Gil Melfe Mateus Santos

Non-cooperative Iris Recognition

University of Beira Interior
Department of Computer Science
August 2009

Gil Melfe Mateus Santos

Non-cooperative Iris Recognition

Thesis submitted to the Department of Computer Science for the fulfillment of the requirements for the degree of Master in Science made under the supervision of Doctor Hugo C. Proença, Assistant Professor at the Department of Computer Science of University of Beira Interior, Covilhã, Portugal

University of Beira Interior
Department of Computer Science
August 2009

> Computer Science is no more about computers than astronomy is about telescopes.
>
> — E. W. Dijkstra

Dedication

To my father, António, and my mother, Manuela, who always believed in me and whose love and support walked me through this stage.

To my sister, Ana, freshwoman next year, who shares the same curiosity for science that somehow inspires me as well.

To my grandfather, Joaquim (1928-2004), who always had a smile on his face and, although not having the opportunity to see me graduate, never doubt that I would succeed.

To all my family, who even if not present were never absent.

To my friends, who I shared with and helped me through this last years, who cheered me up when this thesis seemed interminable and who will never be forgotten.

To God.

Acknowledgements

First and foremost, I would like to thank my supervisor Dr. Hugo Proença, whose expertise, guidance and patience led me to successfully achieving the proposed goals.

I am also thankful to my colleagues and professors at SOCIA Lab, with whom I worked for this last year, and shared not only a laboratory but also an handful of knowledge.

At last, I acknowledge the financial support given by “FCT - Fundação para a Ciência e Tecnologia” and “FEDER” in the scope of the PTDC/EIA/69106/2006 research project “BIOREC: Non-Cooperative Biometric Recognition”.

Abstract

The dramatic growth in practical applications for iris biometrics has been accompanied by relevant developments in the underlying algorithms and techniques. Along with the research focused on near-infrared images captured with subject cooperation, efforts are being made to minimize the trade-off between the quality of the captured data and the recognition accuracy on less constrained environments, where images are obtained at the visible wavelength, at increased distances, over simplified acquisition protocols and adverse lightning conditions. At a first stage, interpolation effects on normalization process are addressed, pointing the outcomes in the overall recognition error rates. Secondly, a couple of post-processing steps to the Daugman's approach are performed, attempting to increase its performance in the particular unconstrained environments this thesis assumes. Analysis on both frequency and spatial domains and finally pattern recognition methods are applied in such efforts. This thesis embodies the study on how subject recognition can be achieved, without his cooperation, making use of iris data captured at-a-distance, on-the-move and at visible wavelength conditions. Widely used methods designed for constrained scenarios are analyzed.

Resumo

O crescimento dramático em aplicações práticas para o reconhecimento da íris está a ser acompanhado por desenvolvimentos notáveis nos algoritmos e técnicas subjacentes. Juntamente com pesquisas focadas em imagens capturadas cooperativamente no *near-infrared*, outras há que são conduzidas no sentido de minimizar a pesada troca entre a qualidade da informação capturada e a precisão do reconhecimento quando em ambientes menos rígidos, onde as imagens são obtidas no comprimento de onda visível, a distâncias relativamente grandes, com condições de iluminação adversas e protocolos de aquisição simplificados. Numa primeira etapa, é estudado o impacto da interpolação no processo de normalização, evidenciando as repercussões na medida final de erro no reconhecimento. Posteriormente, e partindo do método de Daugman, duas vertentes de pós-processamento são testadas tentando aumentar a *performance* do mesmo quando aplicado aos ambientes particularmente adversos em que esta tese se enquadra. São para tal concebidas análises tanto ao domínio espacial como das frequências e, finalmente, métodos de reconhecimento de padrões são aplicados. Esta tese dá assim corpo a um estudo sobre a exequibilidade do reconhecimento de pessoas quando em ausência da sua cooperação, utilizando a informação contida na íris de cada indivíduo que, sendo capturada no comprimento de onda visível, poderá ainda encontrar-se a uma mais alargada distância e em movimento. São analisados métodos utilizados em larga escala para cenários controlados.

Notation

Acronyms

AUC	Area Under Curve
BLPOC	Band-limited Phase-Only Correlation
CA	Classification Accuracy
DCT	Discrete Cosine Transform
FAR	False Accept Rate
FDA	Fisher Discriminant Analysis
FFT	Fast Fourier Transform
FRR	False Reject Rate
HD	Hamming Distance
kNN	k-Nearest Neighbours
LDA	Linear Discriminant Analysis
LR	Logistic Regression
LFDA	Local Fisher Discriminant Analysis
LPP	Locally Preserving Projection
NB	Naive Bayes
NICE.I	Noisy Iris Chalange Evaluation - Part I

NIR	Near-Infrared
PCA	Principal Component Analysis
POS	Product-of-Sum
ROC	Receiver Operating Characteristic
STR	Signal to Noise Ratio
SVM	Support Vector Machine
mRMR	minimum Redundancy Maximum Relevance
VW	Visible Wavelength
XOR	Exclusive OR

Operators

$A \cap B$	And operator between A and B
$A \otimes B$	Binary exclusive or between A and B
$A * B$	Convolution of X with Y
$(X)_{\downarrow 2}$	Down-sampling of X by a factor of two
$(X)_{\uparrow 2}$	Up-sampling of X by a factor of two
$\|\| \bullet \|\|$	Euclidean norm
$\mathrm{sgn}(X)$	Signal operator (1 if positive, 0 otherwise)

List of Figures

List of Tables

Contents

Chapter 1

Introduction

As a part of a growing information society, security became nowadays more than ever an asset of great significance in almost every field. In the process to achieve such safety, the ability of accurately identify subjects based on their biometrical features has been receiving an increased concern and enthusiasm by the scientific community, as more researchers try to develop new methods capable of step up with new needs and challenges. In biometric recognition and from a pattern recognition perspective, subjects physical attributes are captured, processed and eventually classified to output their identities. The use of such recognition systems as a replacement for traditional security systems has become deployed widely by both private and public entities.

From biometrics, which comprehends a vast number of topics, iris usage as a non-intrusive identification method has been privileged, since it causes no constrain to the subject, and it has an information rich structure that stays almost unchanged during lifetime.

This field of iris biometrics is becoming dramatically bigger in both practical applications and the algorithms underneath them. That growth is visible not only in the Near-Infrared (NIR) spectrum where commercial appliances are mostly focused for its robustness in results, but also on the efforts being made to wide the operation field to Visible Wavelength (VW) scenarios and situations where subject cooperation tends to become non-existent.

Being able to identify a subject without the need for his cooperation or, eventually, even having the means to perform recognition without him intuitively understanding to be part on it, is an tempting goal.

Along with that effort, is clear the involved trade-off between the quality of acquired data and the sharpness of results, as noise factors are inevitably introduced during the process.

1.1 Motivation and Objectives

This thesis is then focused on balancing that trade-off, in the search for a performance improvement on such conditions.

Although its great pattern variability among different persons [15], iris has a small size and is problematic to image [18]. According to Daugman [18], a minimum radius of 70 pixels is needed to capture sufficient details of its patterns, and at least 50% of the iris must be visible.

When image acquisition for the iris recognition process falls into the non-cooperative field and is obtained within the VW as well, aggravation occur as artifacts tend to appear. This sort of scenes are prone to various types of noise [53, 54], which eventually result in inferior or defective data degrading the overall process.

The main problem, as in all pattern recognition systems, is to balance the relation between inter and intra-class variability so that the one among different instances of the same class is less than that for different classes [18]. To achieve that, we focus our efforts mainly in the encoding and matching stage.

1.2 Contributions

The diagram present at figure 1.1 gives a general overview over our research work. Areas delimited with dashed lines represent the introduced contributions.

In the first one, Normalization, which is of further discussion at chapter 4, we stress the application of different interpolation methods in the normalization stage of the iris recognition process [57].

In the second one, Feature Extraction, which will be described in chapter 5, we propose several post-processing options for both spatial and frequency domains that, when applied to the used matching result, will conduct to better performance.

The work developed during this dissertation is also to be included in the BioRec - *Non-cooperative Multimodal Biometric Recognition* project [1] (PTDC/EIA/69106/2006),

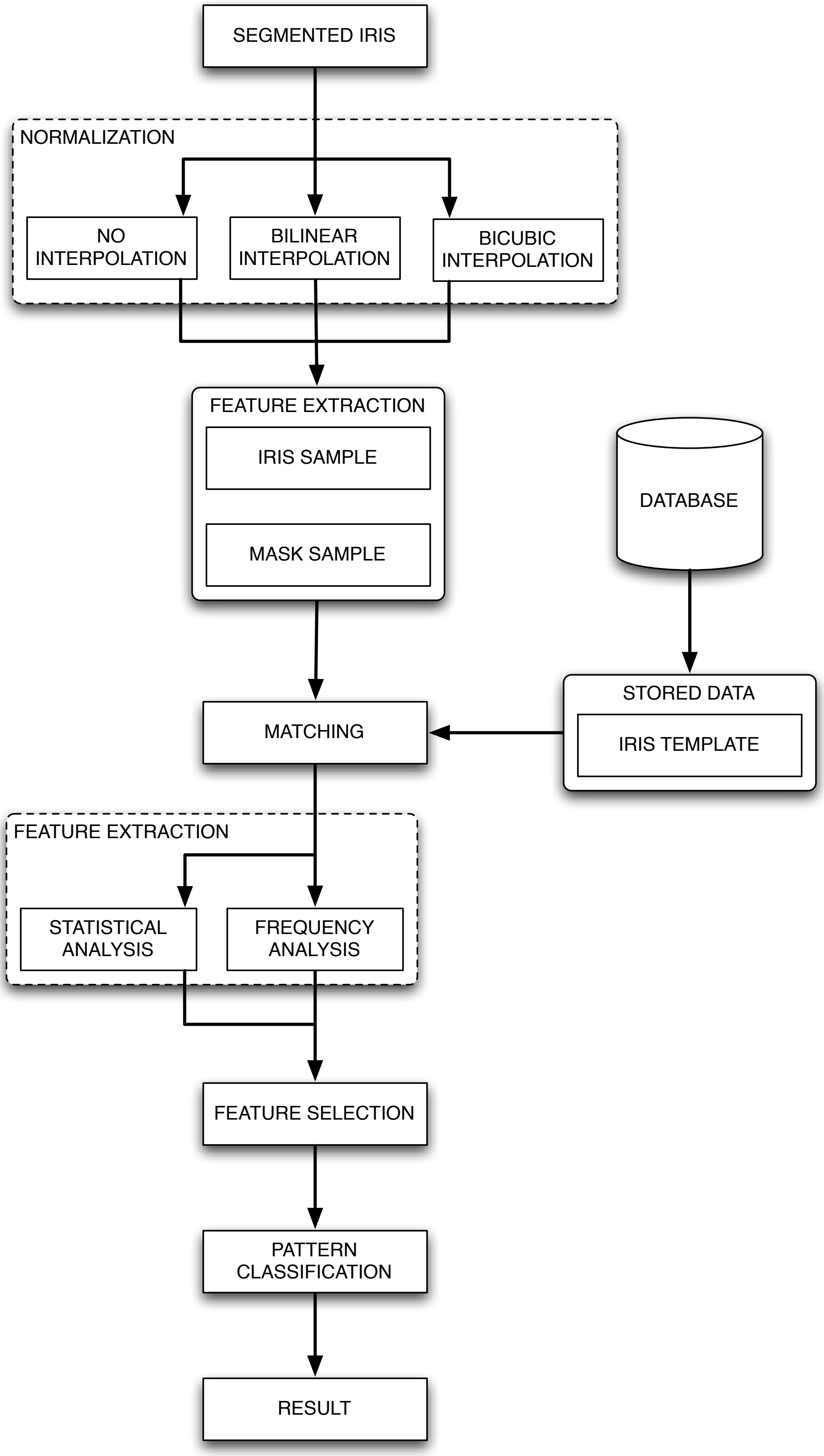

Figure 1.1: Overview of the main steps in our research work.

financed by the FCT and FEDER. BioRec serves the purpose of achieving real-time subject recognition without cooperation through different biometric assessments, being the iris one of them, processed from VW captured images. The work here presented is pointed at that precise module.

1.3 Thesis Outline

The remaining of this thesis is structured as follows: Chapter 2 presents the state-of-the-art, introducing biometrics and existent methodologies on the iris recognition process; Chapter 3 introduces a brief problem description, as well as some experimental considerations; Chapter 4 describes the study for the normalization stage, as well as the performed trials and obtained results; Chapter 5 indicates the proposed encoding and matching stages, feature extraction details and applied pattern recognition processes with respective tests and outcomes; Chapter 6 contains the conclusion.

Chapter 2

State of The Art

2.1 Biometrics

As the science and technology of accessing and analysing biological data, biometrics refers to technologies that measure and analyse human body characteristics for authentication purposes [50]. It comprehends a wide variety of traits, being the most commonly used for biometric purposes the ones we now present.

DNA The deoxyribonucleic acid is representable through a one-dimensional code and is unique for each person. Although the majority of DNA does not differ between individuals, the small portion that does correspond to 3 million base pairs. It is highly prone to contamination and does not allow real-time recognition.

Ear Ears have been used for subject identification, specially at crime scenes where fingerprints are absent. However, its uniqueness is questioned and, since it can be easily covered, user cooperation is required for ear imaging. As advantages we can point the requirement of small dimension images and the less expression variability.

Face The face is the most common biometric characteristic, as humans use it to perform personal recognition. It is non intrusive, and allows convert recognition. Despite commercially deployed recognition systems performances for this treat are reasonable, difficulties arise when facing an uncontrolled ambient.

Facial Thermogram Heat patterns radiated by the human body are considered to be unique for each person. Furthermore, face capturing through infrared cameras produce unique facial signatures, built on heat passing through facial tissue, called “facial thermograms”. This non-invasive treat is highly compromised by nearby hot surfaces.

Finger Geometry Finger geometry is relatively hard to distinguish compared to other treats. It consists on the assessment of finger length, width, thickness and curvature. Despite of having a relatively simple and non-intrusive acquisition technique, it requires the subject to align the fingers against several pegs.

Fingerprint Used for many centuries, either by creating an ink impression of its patterns or using a reader device, the access to the details of fingerprint ridges and furrows, allied to some minutiae points, can determine its uniqueness. Although being a mature and easy-to-use technology, it also requires user cooperation and is vulnerable to noise.

Gait Shape and dynamics of subjects way of walking can be potential information for identification. The analysis of time-series features, stride length, cadence and speed or silhouette can allow subject differentiation. However, these features are vulnerable to changes on walking surface, speed or carrying conditions.

Hand Geometry Used since early 1980’s for low security applications, holds as characteristics hand shape, length and fingers widths. This kind of systems are easy to use and inexpensive, but require a relatively high contact surface which makes it unsuitable for certain purposes.

Hand Vein The pattern in blood veins, being unique for each individual, can be captured with NIR illumination and constitute a relatively secure biometric trait. It is based on the deoxidized hemoglobin property to absorb infrared ray, causing veins to appear black. Although this procedure can hardly be forged, it requires as well a relatively high level of cooperation.

Iris Holding complex patterns, can contain many distinctive features for subject discrimination. It is relatively hard to forge, since artificial irises can be detected, and its optimal imaging occurs in the NIR through expensive frameworks which require considerable user participation.

Keystroke Based on the belief that each person types on a keyboard in a distinguishable way, the analysis of such rhythms can lead to subject identification. Is a biometric trait that allows continuous monitoring, which reduces counterfeit attempts effectiveness, but carries obvious privacy concerns.

Palmprint Alike fingerprints, palms contain unique patterns. Since they are larger than fingers, distinction between subjects is expected to be more accentuated, but also require a larger acquiring surface being therefore more expensive.

Retina Retinal scan captures the vein patterns in the back of the eye. It is stable, unique and very hard to forge and, therefore, considered as one of the most secure traits. However, retina is small, internal and hard to image, requiring very high cooperation from the subject.

Signature The way a person signs his name is a characteristic of that individual for centuries. The classical analysis of this treat is based upon visual appearance of the signature, but the speed, direction, pressure of writing can also be analysed. Despite its well acceptance, is prone to physical and emotional conditions.

Voice This treat uses acoustic information instead of visual one. Consists on the examination of voice characteristics to perform subject recognition, and is used only on low-security applications for its variability and poor accuracy performance.

2.2 Iris Recognition

The iris recognition process comprehends certain steps, which will be under discussion in this chapter. Therefore, the nuclear sequence that provides core structure for iris recognition process (when using a previously acquired image) is:

- Image segmentation: Location and extraction of the iris segment on the image.
- Noise detection: Distinction between the iris pixels *per se* and all the distortions caused by external factors.
- Image Enhancement: Improvement of the iris image quality, as an attempt to compensate noise factors and optimize performance on upcoming operations.
- Normalization: Conversion of the segmented iris to a coordinates system able to deliver invariance to several factors.

- Encoding and Matching: Conversion of the iris data to a structure susceptible of a better corresponding, and the matching itself.

This last item englobes not one but two actions, which by their characteristics are not dissociable from each other, and will be treated as one.

Although some of the cited authors do not use all of the steps above mentioned, these are in fact the necessary ones to the achievement of the goal proposed in this thesis, as I comprehend it.

Noise detection and image enhancement are not implemented, but can be subject of further work as discussed at chapter 6.

2.3 Segmentation

In the segmentation process, some details on the iris part of the image must become known: as its location, shape and size. This involves the determination of its boundaries, with both the pupil and the sclera. To achieve this goals, various actions can be taken, the most relevant being the ones that follow.

2.3.1 Daugman's Integro-differential

John Daugman's pioneer approach [14, 18] is known to be most widely used in processing NIR iris images for recognition purposes.

As before stated, he defends that an iris with a radius larger than 70 pixels must be used in order for its patters to have the necessary information for person identification. He also states that only NIR illumination allows detail extraction in strongly pigmented irises.

The segmentation is made over images beyond a minimum focus level, which assessment is achieved through the analysis of the middle and upper frequency bands of 2D-Fourier spectrum. To look for both the inner and outer contours of the iris, the application of his integro-differential operator defined as follows is required :

$$\max_{r,x_0,y_0} \mid G_\sigma(r) * \frac{\partial}{\partial r} \oint_{r,x_0,y_0} \frac{I(x,y)}{2\pi r} ds \mid \tag{2.1}$$

where $I(x, y)$ is the image containing the iris, and G_θ the Gaussian of scale θ.

A similar operation is used for eyelid boundaries, changing the contour integration form circular to arcuate. In his later work [19], Daugman introduced some new improvements allowing flexible shapes.

Daugman, once again, specifies that images with less than 50% of visible iris are useless.

Tisse *et al.* [61] use a process that combines this integro-differential with the Hough Transform, which will be subject of further discussion in the next sub-section, as they claim that integro-differential is affected by spot reflexions of non-diffused artificial light.

2.3.2 Hough's Transform

Several authors, like Wildes [66], Ma *et al.* [37], Tisse *et al.* [61] and Monro *et al.* [43], apply Hough transform for circle detection in iris boundaries determination.

Wildes [66], prior to Hough transform application, creates a binary edge-map from the acquired image by thresholding the magnitude of the intensity gradient, applying equation (2.2) where $\bigtriangledown \equiv (\partial/\partial x, \partial/\partial y)$ and $G(x, y)$ is the 2D Gaussian centered in (x, y), defined by equation (2.3).

$$\mid \bigtriangledown G(x, y) * I(x, y) \mid \tag{2.2}$$

$$G(x, y) = \frac{1}{2\pi\sigma^2} e^{-\frac{(x-x_0)^2+(y-y_0)^2}{2\sigma^2}} \tag{2.3}$$

Ma *et al.* [37] localize pupil center as the minimal value of the two dimensional projections of the image. They then convert to binary a 120 square region surrounding that center prior to Houghs tranform application.

Tisse *et al.* [61] use a particular combination of a gradient decomposed Hough Transform with the previous mentioned Daugman's integro-differential. It consists in the application, at first, of an edge detection method to determine the approximate position of the eye, followed by the integro-differential which will find the boundaries.

Monro *et al.* [43], before applying Hough transform, reduce the working area by isolating a region containing the iris using an heuristic method. Then, an edge detection is applied and noise removed.

2.3.3 Other approaches

Besides the supra-cited methodologies several authors use different approaches which are less frequent. Broussard *et al.* [8] use a neuronal network to parse features from each pixel and decide whether they are or not iris. Zhu *et al.* [72] use a simple technique based on thresholds to identify iris boundaries.

2.4 Noise Detection

When moving to the VW, specially coming from such a favorable space as the NIR, some associated problems must be dealt with, which are even more aggravated by the unconstrained acquisition protocols. The most concerning is, without doubt, the inclusion of new noise factors that compromise the recognition process.

Despite being considered the most reliable form of biometric assessment for its impressive low False Accept Rate (FAR) when compared to other modalities, False Reject Rate (FRR) is surprisingly high due to poor quality images [12].

For the Noisy Iris Chalange Evaluation - Part I (NICE.I) [53], a challenge focused on the same database our work is mainly centered in, Proença and Alexandre pointed several noise factors (figure 2.1):

Out-of-Focus Subject movement allied to imaging systems limitations (namely in the depth-of-field, poor lightning/exposure ratio) often produce out-of-focus images with repercussions on the steps to come.

Off-Angle Subject head and eye rotation or lack of alignment will produce off-angle iris images.

Rotation Tilt of the head, despite of the subject being or not facing the camera.

Motion blur Blurred iris images deteriorate its location and, since high-frequency information is lost, matching results are also less accurate. Eyelid movement significantly contributes to this type of noise.

Obstructions Various types of blocking objects can be found, being the most commons: eyelids, eyelashes, glasses and contact lenses. Almost all this occlusions are naturally associated with vision itself and can not be prevented without subject cooperation.

(a) Poor focused iris image. (b) Off-angle iris image. (c) Rotated iris image

(d) Motion blurred iris image. (e) Iris with eyelid and eyelash obstructions. (f) Eye with contact lenses.

(g) Iris with large reflection areas. (h) Partial captured iris image. (i) Out-of-iris image.

Figure 2.1: Examples of noisy iris images. These images contain the majority of the described noise factors, that result from less constrained image capturing conditions [53].

Reflections Generally strong reflections caused by light sources or weak ones introduced by surroundings, are most likely to appear on eye surface.

Partial Iris Without user cooperation, images can appear where iris is not completely visible. This clearly causes reduction on the available matching data.

Out-of-iris Images where iris is not present at all, either because fully occlusions or the eye not being present in the frame.

Addressing this issue, Proença and Alexandre presented a method [52] for the identification of noisy regions in normalized iris images. Although their method only gives a binary output for pixels being or not noise, the specification of noise type could be helpful for possible image enhancements through noise compensation. Examples of this kind of improvement are presented in several papers [19, 32, 58, 62, 67, 45, 29], although most of them only deal with NIR captured images.

Chen *et al.* [12] proposed a method that quantifies the quality of the acquired iris images and, when included in the matching process, increases the performance on NIR captured data-sets. It is based mainly on iris texture that, analysed locally through 2D wavelets of concentric bands, delivers a quality index to weight the matching distance. They also assemble several methods allowing to identify noise location, which naturally correspond to a low quality index. The same purpose was also addressed by Belcher and Du [5] who presented a quality measurement method as well, for NIR iris images, based on feature information.

2.5 Normalization

Once completed the segmentation stage, normalization is needed to obtain invariance to several factors (size, rotation, position, iris dilatation, etc.) and make possible the encoding and matching process.

The most widely used method for that purpose is Daugman's rubber-sheet model [17], which converts the iris to a rectangular block over a doubly dimensionless non-concentric polar coordinate system. With the application of equations (2.4) and (2.5), the iris image is transformed as shown on figure 2.2.

$$I(x(r,\theta), y(r,\theta)) \rightarrow I(r,\theta) \tag{2.4}$$

$$\begin{aligned} x(r,\theta) &= (1-r)x_p(\theta) + r x_s(\theta) \\ y(r,\theta) &= (1-r)y_p(\theta) + r y_s(\theta) \end{aligned} \tag{2.5}$$

Where r and θ denote respectively the radius and the angle, $x(r,\theta)$ and $y(r,\theta)$ are defined as linear combinations of both the set of pupillary boundary points $(x_p(\theta), y_p(\theta))$ and the set of limbus boundary points along the outer perimeter of the iris $(x_s(\theta), y_s(\theta))$ bordering the sclera.

Wildes [66], by other side, performs a spacial alignment between the acquired image I_a and the one present in the database I_d using a mapping function $(u(x,y), v(x,y)$ to minimize equation (2.6) so that image intensity at $(x,y) - (u(x,y), v(x,y))$, in I_a, is

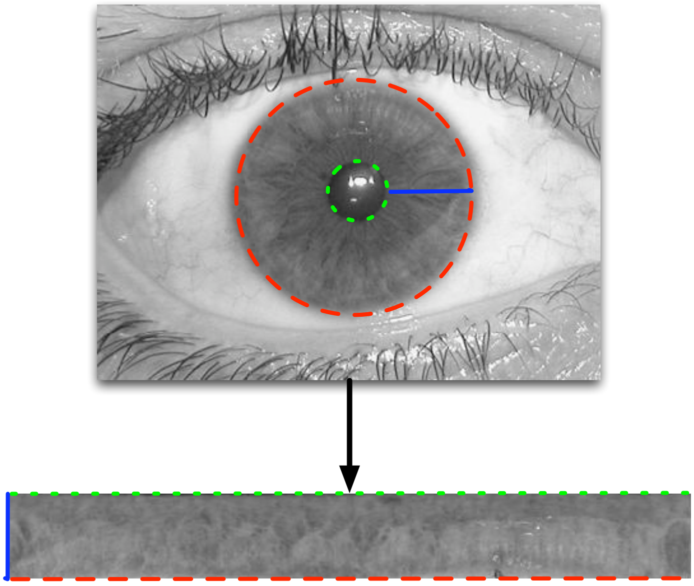

Figure 2.2: Illustration of the normalization of the segmented data into the polar coordinate system, through the “Daugman rubber-sheet” model.

closer to the one at (x, y) in I_d.

$$\int_x \int_y (I_d(x,y) - I_a(x-u, y-v))^2 \, dx \, dy \tag{2.6}$$

This operation is constrained to capture a similarity transformation of image coordinates (x, y) to (x', y') according to the following equation

$$\begin{pmatrix} x' \\ y' \end{pmatrix} = \begin{pmatrix} x \\ y \end{pmatrix} - sR(\phi) \begin{pmatrix} x \\ y \end{pmatrix} \tag{2.7}$$

Where s is a scaling factor and $R(\phi)$ a matrix representing rotations by ϕ.

2.6 Encoding and Matching

Although most of the proposed methods follow the statistical pattern recognition paradigm, encoding iris texture information through phase, zero-crossing or texture analysis based procedures, others are that follow structural (syntactic) approaches.

The principal difference is that, while the first ones represent patterns as sets of features regarded as points in a d-dimensional space being their efficiency determined by class separability, structural methods deal with each pattern as a set of sub-patterns being the most elementary ones called primitives. Relations between primitives allow us to describe patterns, being used for that purpose symbolic structures (strings, trees and graphs) [51].

Several statistical approaches [18, 66, 43, 37, 42] plus a couple of structural ones [70, 51] were studied and briefly explained in the following sub-sections.

2.6.1 Daugman's Iris-code

After the previous steps, John Daugman [14, 18] proceeds with pattern demodulation applying 2D Gabor wavelets (2.8).

$$h_{\{Re,Im\}} = \text{sgn}_{\{Re,Im\}} \int_{\rho} \int_{\phi} I(\rho, \phi) e^{iw(\theta_0 - \phi)} . e^{-(r_0-\rho)^2/\alpha^2} e^{-(\theta_0-\phi)^2/\beta^2} \rho d\rho d\phi \tag{2.8}$$

In this equation (2.8): $h_{\{Re,Im\}}$ are complex-valued bit, which value 0 or 1 (sgn) depends on the sign of the integral; $I(\rho, \phi)$ is the input image in the dimensionless pseudo-polar coordinate system (referred in section 2.5); α and β are the multiscale wavelet parameters; θ is the wavelet frequency; and (r_0, θ_0) represent the polar coordinates.

The produced iriscode, despite its incredible simplicity, have the power to precisely represent the phase information [34].

This implementation [18] also computes the mask to indicate whether or not the iris is affected by noise (eyelid obscuration, eyelash occlusion, specular reflections, contact lens artifacts and poor Signal to Noise Ratio (STR)) and therefore be excluded in the demodulation code.

Another important aspect of this method is that only phase information is used. Amplitude depends on contrast, illumination, camera gain and, as it is not discriminant, will be discarded.

Finally, the dissimilarity between the irises is given by this Hamming Distance (HD) equation (2.9) from where 0 represents a perfect match.

$$HD = \frac{\|(codeA \otimes codeB) \cap maskA \cap maskB\|}{\|maskA \cap maskB\|} \tag{2.9}$$

In this formula $\{codeA, codeB\}$ are irises code-bit vectors and $\{maskA, maskB\}$ the related noise mask codification. The Exclusive OR (XOR) operator finds disagreeing bits, while AND ensures that data is not damaged by noise.

The performance of this method can be accessed by its decidability (2.10), that reflects the distance between the two distributions obtained respectively for the comparisons between signatures extracted from the same (*intra-class*) and different persons (*inter-class*).

$$d' = \frac{|\mu_{inter} - \mu_{intra}|}{\sqrt{\frac{\sigma^2_{inter} + \sigma^2_{intra}}{2}}} \tag{2.10}$$

Where μ_{inter} and μ_{intra} denote means for the inter- and intra-class comparisons, and σ_{inter} and σ_{intra} the respective standard deviations.

Later on, Yao *et al.* proposed a very similar methodology [69, 68] where the complex Gabor filters were replaced by modified Log-Gabor filters. These last ones, having the advantage of being strictly bandpass filters, are therefore more suitable for iris phase features extraction regardless of background brightness. Although the authors even claim to have better performance than the original method from Daugman, we selected the original as it is widely accepted.

2.6.2 Wildes' Pyramid

The matching process presented by Wildes [66] uses no normalization whatsoever, performing instead a spacial alignment with the database record. After this alignment two steps take place: selection of a representation that maximizes distinctive patterns; and determination of the similitude between the two irises.

Regarding the first step, Wildes [66] considers advantageous the use of a multi-scale representation of the iris (figure 2.3), so that a wider range of spacial detail can be captured. For that purpose, an isotropic bandpass decomposition is performed using these filters

$$-\frac{1}{\pi\sigma^4}\left(1 - \frac{\rho^2}{2\sigma^2}\right) e^{\rho^2/2\sigma^2} \tag{2.11}$$

where σ is Gaussian standard deviation and ρ the radial distance to the filters center.

The represented pyramid (figure 2.3) is then a cascade of Gaussian-like filters, where the set of images g_k is obtained applying equation (2.12), starting with an original image ($g_0 = I$). Each level k of the pyramid is given by equation (2.13).

$$g_k = (W * g_{k-1})_{\downarrow 2} \tag{2.12}$$

$$l_k = g_k - 4W * (g_{k+1})_{\uparrow 2} \tag{2.13}$$

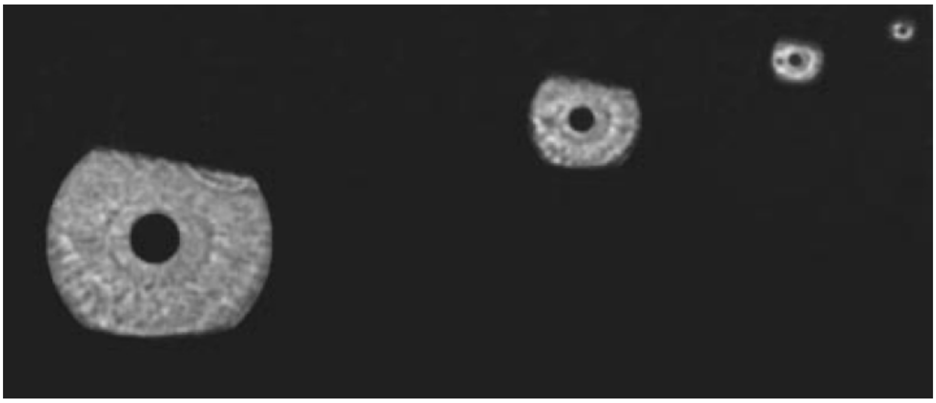

Figure 2.3: Wildes' multi-scale representation for iris pattern matching [66].

In equations (2.12) and (2.13), $W = w^T w$ and $w = [1\ 4\ 6\ 4\ 1]/16$. The upsampling operation in equation (2.13) requires the insertion of rows and columns of zeros, intercalated with original data.

Once these operations have been completed, the similarity between the engaged images must be accessed. For that purpose, Wildes used the normalized correlation (2.14) in 8 × 8 square windows for each of the four bands of the pyramid, which intensifies local variations.

$$\frac{\sum_{i=1}^{n}\sum_{j=1}^{m}(p_1[i,j]-\mu_1)(p_2[i,j]-\mu_2)}{nm\sigma_1\sigma_2} \tag{2.14}$$

In the above equation, μ_1 and σ_1 are the mean (2.15) and standard deviation (2.16) for image intensities array $p_1[i,y]$ of size $m \times\ n$, as follows.

$$\mu_1 = \frac{1}{nm}\sum_{i=1}^{n}\sum_{j=1}^{m} p_1[i,j] \tag{2.15}$$

$$\sigma_1 = \sqrt{\frac{1}{nm}\sum_{i=1}^{n}\sum_{j=1}^{m}(p_1[i,j]-\mu_1)^2} \tag{2.16}$$

Finally, the four *goodness-of-match* measures are combined using Fisher's linear discriminant:

Having n dimensional samples q, n_a from set A (authentic iris comparisons) and n_i from set I (impostor iris comparisons), a weight vector ω is defined to maximize the ratio of between classes variance to within classes variance for the transformed samples $\omega^\top q$. More precisely, having $\mu_a = (\Sigma_{q\in A}\ q)/n_i$ as the *d-dimensional* mean for

$q \in A$ and similiarly for μ_i, the variance within a class of data can be accessed by a scatter matrix (2.17) as follows:

$$S_a = \sum_{q \in A} (q - \mu_a)(q - \mu_a)^\top \tag{2.17}$$

With S_i similarly defined for I, the total within class scatter is then $S_w = S_a + S_i$.

The variance between classes can also be defined as a scatter matrix (2.18):

$$S_b = (\mu_a - \mu_i)(\mu_a - \mu_i)^\top \tag{2.18}$$

Finally, the ratio of between to within class variance of the transformed samples ωq is given by (2.19). This ratio is maximized through equation (2.20).

$$\frac{\omega^\top S_b \omega}{\omega^\top S_\omega \omega} \tag{2.19}$$

$$\omega = S_\omega^{-1}(\mu_a - \mu_i). \tag{2.20}$$

The separation point above which the classes derive from A and bellow from I is given by (2.21):

$$(1/2)\omega^\top(\mu_a - \mu_i) \tag{2.21}$$

2.6.3 Monro *et al.* Discrete Cosine Transform

Monro *et al.* [43] proposed a different and yet simple iris coding method, based on the Discrete Cosine Transform (DCT).

The normalized image is decomposed in 11 horizontal 8×12 bands, with overlapping (4 pixels vertically and 6 pixels horizontally) and a 45° rotation (figure 2.4). Eight pixels from each patch form a 1D vector, which is windowed using a Hanning window prior to application of the DCT. The differences between the DCT coefficients of adjacent patch vectors are then calculated and a binary code generated from their zero crossings.

The distance of two feature vectors is measured using the Product-of-Sum (POS) of individual sub-features HD, which can be defined as follows:

$$HD = \left(\prod_{i=1}^{M} \frac{\sum_{j=1}^{N} (SubFeature\ 1_{ij} \oplus SubFeature\ 2_{ij}))}{N} \right)^{1/M} \tag{2.22}$$

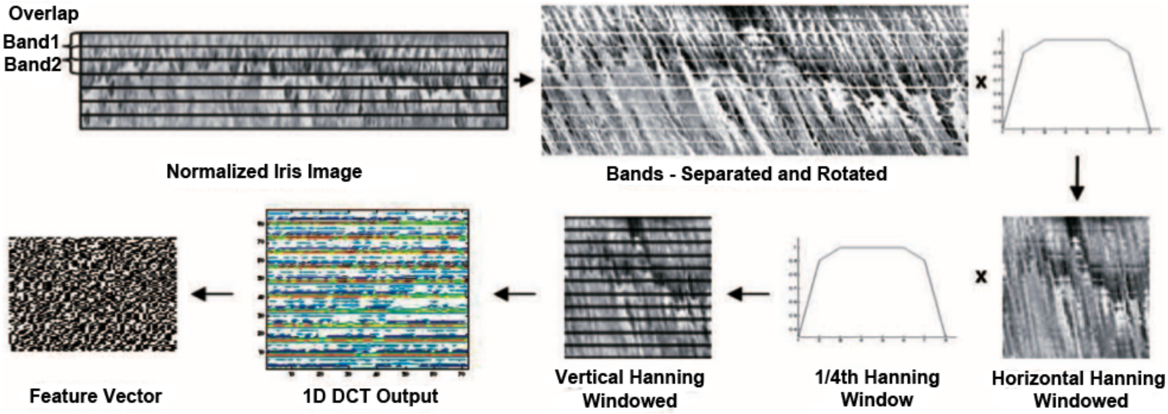

Figure 2.4: Illustrating the various steps in forming feature vectors from normalized iris images. [43]

2.6.4 Ma *et al.* Texture Analysis

Ma *et al.* [37] based their method on feature extraction from Gabor filtered images.

To the normalized image extracted from a optimum spot in the original image, even symmetric Gabor filters (2.23) are applied.

$$\begin{aligned} G(x,y,f) &= \frac{1}{2\pi\delta_x\delta_y}\exp\left[-\frac{1}{2}\left(\frac{x^2}{\delta_x^2}+\frac{y^2}{\delta_y^2}\right)\right]M_i(x,y,f);\ i=1,2. \\ M_1(x,y,f) &= \cos\left[2\pi f\left(\sqrt{x^2+y^2}\right)\right], \\ M_2(x,y,f) &= \cos\left[2\pi f\left(x\cos\theta+y\sin\theta\right)\right], \end{aligned} \tag{2.23}$$

where $M_i(x,y,f)$ denotes the modulation function, M_1 and M_2 are the modulating functions respectively, f is the frequency of the sinusoidal function, δ_x and δ_y are the space constants of the Gaussian envelope along the x and y axis, and θ denotes the orientation of the filter. From this output, and using the regions closer to the pupil, two features are extracted for 8×8 blocks (w) of n pixels: mean m and average standard deviation σ, which are arranged in a 1D vector V.

$$m = \frac{1}{n}\sum_w \left|F_i(x,y)\right|, \quad \sigma = \frac{1}{n}\sum_w \left|\left|F_i(x,y)\right| - m\right| \tag{2.24}$$

$$V = \left[m_1, \sigma_1, m_2, \sigma_2, ..., m_M, \sigma_M\right]^{\mathrm{T}} \tag{2.25}$$

After feature extraction, dimensionality is reduced using Fisher Linear Discriminant

[6] [36], and to the resultant feature vector f the nearest center classifier is applied (2.26) to obtain the dissimilarity measure $d_n(f, f_i)$ for the m^{th} class.

$$\begin{aligned} m &= \arg\min_{1\leq i\leq c} d_n(f, f_i); \quad n = 1, 2, 3. \\ d_1(f, f_i) &= \sum_j \left|f^j - f_i^j\right| \\ d_2(f, f_i) &= \sum_j \left(f^j - f_i^j\right)^2 \\ d_3(f, f_i) &= 1 - \frac{f^{\mathrm{T}} f_i}{||f||\ ||f_i||} \end{aligned} \tag{2.26}$$

where f and f_i are the feature vectors of an unknown sample and the i^{th} class, respectively, f^j and f_i^j are the j^{th} component of the feature vector for the unknown sample and the one for the i^{th} class respectively, and c is the total number of classes.

2.6.5 Yu and Zhang Key-points

Yu and Zhang [70] preset in their paper an interesting work based on key-point extraction and relative distance computing.

Starting from a normalized image, 2D Gabor filters (2.27) are used for key-point extraction. Variations are made in the width α and height β (standard deviation) parameters, as well as on the wavelength T and the angle θ between the (x, y) and (x', y') coordinates systems.

$$G(x, y, f, \theta) = e^{-(x'^2/2\alpha^2)-(y'^2/2\beta^2)} e^{-(2\pi_i/T)x'} \tag{2.27}$$

with x' and y' given by

$$\begin{bmatrix} x' \\ y' \end{bmatrix} = \begin{bmatrix} cos\theta & sin\theta \\ -sin\theta & cos\theta \end{bmatrix} \begin{bmatrix} x \\ y \end{bmatrix} \tag{2.28}$$

Such variations produce a total of 32 filters and, consecutively, the same number of resultant images (figure 2.5), where blocks similar to the filters will get larger coefficients. Those points with the largest absolute value in the channels filtered image are then regarded as feature points and, given a certain number of points with the biggest coefficient, their barycenter is taken as the key-point.

Let $F(x, y)$ be the absolute value of a filtered image,

$$LFP = [(x_1, y_1), (x_2, y_2), ..., (x_m, y_m)] \tag{2.29}$$

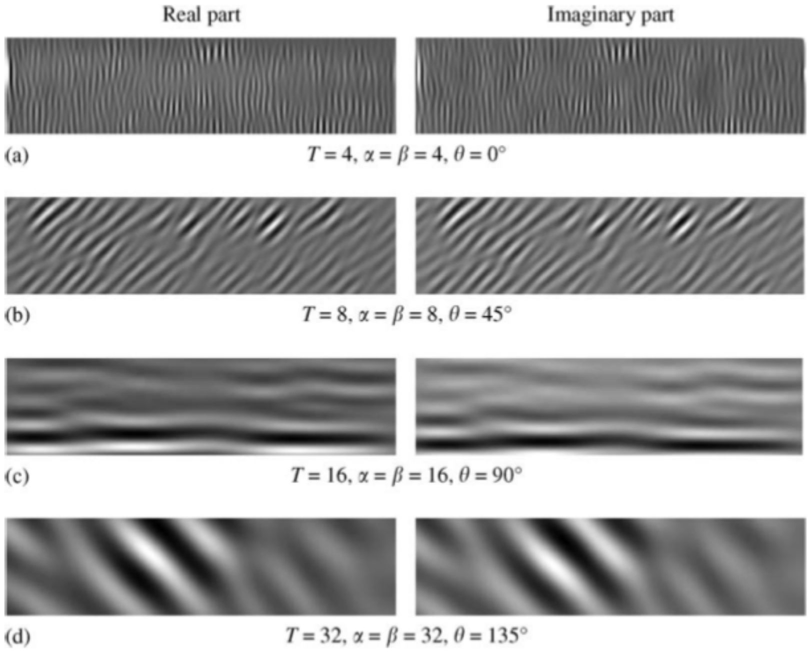

Figure 2.5: The filtered images in some channels [70].

the location of feature points, and m a parameter, then the location of key-point (x_{KP}, y_{KP}) is given by

$$\begin{array}{ll} x_{KP} = \frac{\Sigma_{i=1}^{m} x_i F(x_i,y_i)}{\Sigma_{i=1}^{m} F(x_i,y_i)}, & \\ & (x_i, y_i) \in LFP \\ y_{KP} = \frac{\Sigma_{i=1}^{m} y_i F(x_i,y_i)}{\Sigma_{i=1}^{m} F(x_i,y_i)}, & \end{array} \tag{2.30}$$

The key-point extraction procedure is applied in blocks, so that each image is subdivided into 16 (2.31), producing a total of 512 key-points for the whole iris image.

$$LKP(k) = \{(x_{KP1}, y_{KP1})_j, (x_{KP2}, y_{KP2})_j, ..., (x_{KP32}, y_{KP32})_j)\},\ j = 1, 2, ..., 16. \tag{2.31}$$

For the j^{th} sub-image, the center of the key-points is given by

$$\begin{array}{ll} O_j(x) = \frac{\Sigma_{n=1}^{32} (x_{KPn}) j}{32}, & \\ & (x_{KPn}, y_{KPn})_j \in LKP(j), j = 1, 2, ..., 16. \\ O_j(y) = \frac{\Sigma_{n=1}^{32} (y_{KPn}) j}{32}, & \end{array} \tag{2.32}$$

Then the distance between the center $O_j(x, y)$ and every key-point is defined as the relative distance (2.33), as better depicted through figure 2.6.

$$D_j(n) = \sqrt{((x_{KPn})_j - O_j(x))^2 + ((y_{KPn})_j - O_j(y))^2},\ n = 1, 2, ..., 32. \tag{2.33}$$

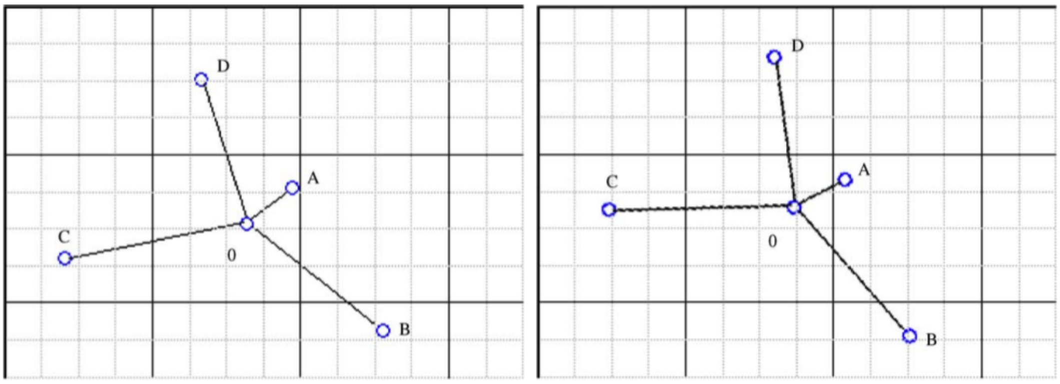

Figure 2.6: An illustration of the relative distance [70].

The total number of relative distances is then 512, and the final similarity value given by (2.34).

$$r = \sqrt{\frac{\Sigma_{i=1}^{512}(D1_l - D2_l)^2}{512}}. \tag{2.34}$$

2.6.6 Miyazawa *et al.* Phase-Based Matching

Miyazawa *et al.* [42] proposed in they recent work a phase-based aproach for iris image matching. After iris location, normalization and optional enhancement, the matching stage comprehends several steps from hence in discussion: effective region extraction, displacement alignment and matching score calculation.

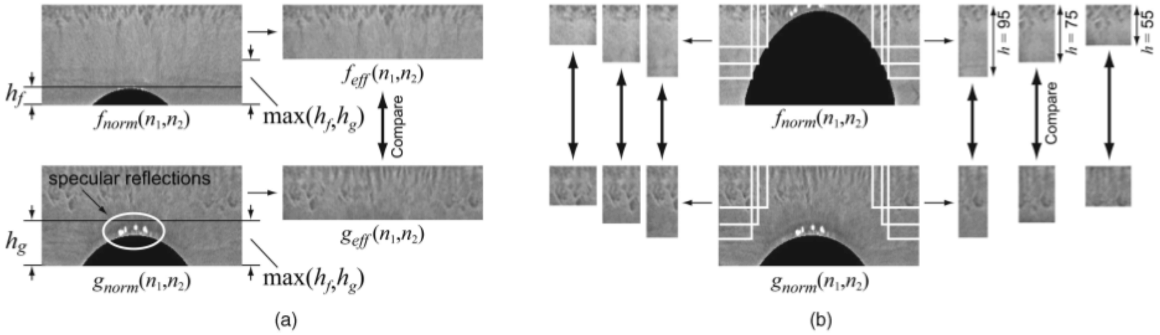

Figure 2.7: Effective region extraction. (a) Normal case. (b) The case when multiple sub-regions should be extracted [42].

Regarding region extraction, divisions are made in $N_1 \times N_2$ sized areas, so that they do not contain data from irrelevant regions. More precisely, being h_f and h_g the heights of irrelevant regions (eyelid occlusions in normalized images), the rule

$N_1 \times N_2\{N_2 - max(h_f, h_g)\}$ is obied (figure 2.7a). In case $\max(h_f, h_g) \simeq N_2$, multiple regions are extracted (figure 2.7b) to compensate and avoid lack of information when performing image matching.

After that, alignment between regions $f_{eff}(n_1, n_2)$ and $f_{eff}(n_1, n_2)$ is accomplished using Band-limited Phase-Only Correlation (BLPOC) (2.35) functions peak. Assuming that the ranges of the inherent frequency band of iris texture are given by $k_1 = -K_1, ..., K_1$ and $k_2 = -K_2, ..., K_2$, where $0 \leq K_1 \leq M_1$, and $0 \leq K_2 \leq M_2$

$$r^{K_1K_2}_{f_{eff}g_{eff}}(n_1, n_2) = \frac{1}{L_1L_2}\sum_{k_1=-K_1}^{K_1}\sum_{k_2=-K_2}^{K_2} R_{FG}(k_1, k_2) \times W_{L_1}^{-k_1n_1} W_{L_2}^{-k_2n_2} \tag{2.35}$$

where frequency spectrum effective size is given by $L_1 = 2K_1 + 1$ and $L_2 = 2K_2 + 1$, $n_1 = -K_1, ..., K_1$ and $n_2 = -K_2, ..., K_2$. This relations can be more clearly seen on figure 2.8.

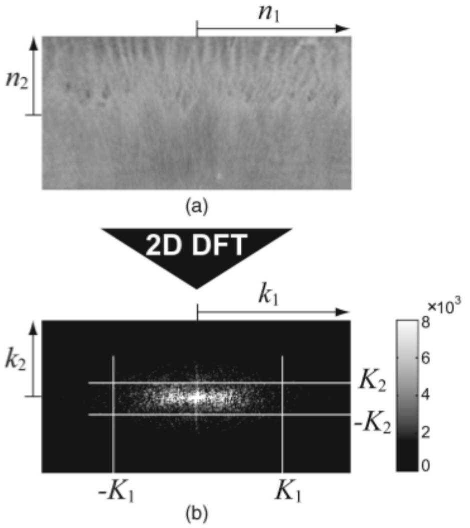

Figure 2.8: Normalized iris image in (a) the spatial domain and (b) the frequency domain (amplitude spectrum) [42].

Finally, matching score calculation is performed applying BLPOC once again, this time aimed at the aligned images. From that operation, the function peak should be centered for genuine matching, and the score measure is simply the maximum value on a centered window O (2.36).

$$Matching\ Score = \max_{(n_1,n_2)\in O}\{r^{K_1K_2}_{fg}(n_1, n_2)\} \tag{2.36}$$

To attenuate possible errors introduced during iris location process, which are translated into erroneous horizontal scaling, ±3%, ±5% and ±7% corrections are made over that axle. When facing a genuine match the peak is accentuated, contrasting to impostor matching where the peak suffers no significant change.

In these authors work [42] a modified algorithm for degraded images is proposed as well, being the main alterations regarding image sectioning. Images are divided into $B_1 \times B_2$ blocks, overlapping adjacent ones by $B/2$ pixels. BLPOC functions are then applied to each block and a weighted average computed, being the weights w given by expression (2.37) according to the noise level (E) they contain.

$$w_i = \begin{cases} 1 - \frac{E_i}{B_1 \times B_2} & \text{if } \frac{E_i}{B_1 \times B_2} < 0.5 \\ 0 & \text{otherwise} \end{cases} \tag{2.37}$$

For performance, the average is computed in the frequency domain. The matching score is calculated as before mentioned (2.36).

2.6.7 Proença's Structural Pattern Analysis

The method proposed by Proença [51] also follows the structural pattern recognition paradigm (Figure 2.9). This method takes as primitives the centers of most homogeneous regions, *i.e.* with lower average differences of intensities between neighbour pixels, as they are intuitively visually more relevant.

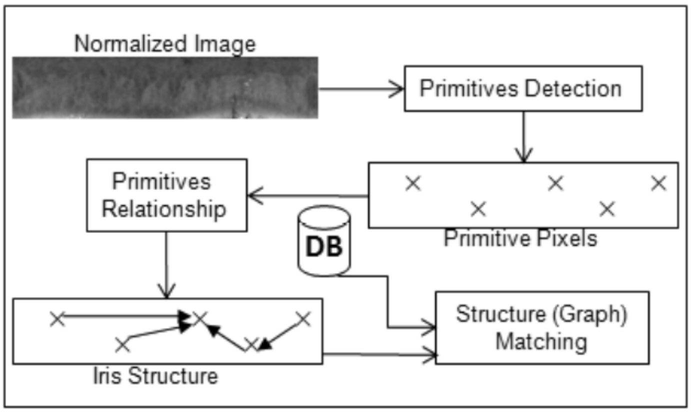

Figure 2.9: Stages of the pattern recognition method proposed by Proença, according to the structural pattern recognition paradigm [51].

From the normalized iris image, the distinctiveness between a pixel $p = (x, y)$ and its $L/2$ radius neighbourhood is accessed by the function $e(x, y) : \mathbb{N}^2 \rightarrow \mathbb{R}$ (equation (2.38)) where $G(x, y)$ is a Gaussian kernel with dimensions $L \times L$ and $I(x, y)$ the intensity at (x, y).

$$e(x,y) = \sum_{i=-\frac{L}{2}}^{\frac{L}{2}} \sum_{j=-\frac{L}{2}}^{\frac{L}{2}} \left[||I(x+i, y+j) - I(x,y)|| \times G\left(i + \frac{L}{2}, j + \frac{L}{2}\right)\right] \tag{2.38}$$

The pixel with minimal $e()$ in its neighbourhood is then considered as primitive (equation (2.39)).

$$pr(x,y) = \begin{cases} 1 & (x,y) = \min_{\frac{L}{2}} e(x_i, y_j) \\ 0 & otherwise \end{cases} \tag{2.39}$$

To establish the relation between the primitives, a graph is built through vertex connection with higher difference between their $e()$. Being $P = \{p_1, ..., p_n\}$, $p_i = (x_i, y_i)$ a set of primitives and $d()$ the euclidean distance, edges are created if

$$e(p_j) < e(p_j) \wedge \frac{e(p_i) - e(p_j)}{d(p_i, p_j)} > \frac{h\left(p_i, \frac{L}{2}\right) + h\left(p_j, \frac{L}{2}\right)}{2} \tag{2.40}$$

where $h(p, r)$ is image entropy in a p centred window with radius r. Examples of this kind of graphs are given by figure 2.10.

The matching between graph $G_1(P_1, E_1)$ and a second one $G_2(P_2, E_2)$ with P_i vertexes and E_i edges is accessed by the dissimilarity $g()$ given by equation (2.41), where each term is weighted through α $(0 \leq \alpha \leq 1)$.

$$g(G_1, G_2) = \alpha\ v(G_1, G_2) + (1 - \alpha) e(G_1, G_2) \tag{2.41}$$

A minimal distance $v()$ between primitives relative position in the graph is given by (2.42).

$$v(G_1, G_2) = \sum_{p_i} \min \frac{d(p_i, p_j)}{|P_1|} + \sum_{p_j} \min \frac{d(p_i, p_j)}{|P_2|} \tag{2.42}$$

where $|P|$ is P set cardinality, with $p_i \in P_1$ and $p_j \in P_2$.

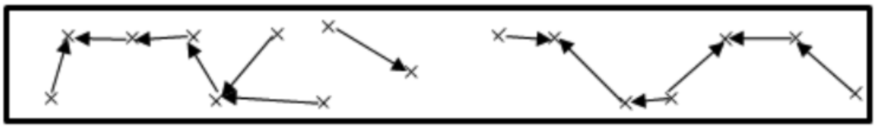

(a) Graph representing the structure the iris image ”1” of subject ”1”.

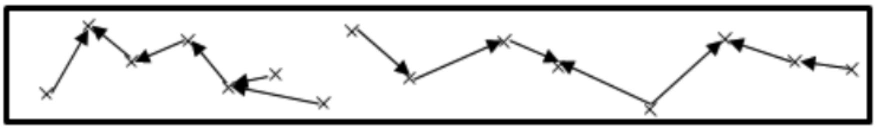

(b) Graph representing the structure of the iris image ”2” of subject ”1”.

(c) Graph representing the structure of an iris image of subject ”2”.

Figure 2.10: Graphs representing the structures of the irises images. The upper two figures illustrate the structure of different images of the same iris and the bottom one from a different person [51].

To the resulting similarity matrix M, with dimensions $|P_1| \times |P_2|$, containing vertex dissimilarities, the minimal distance is given by $e()$ (2.43).

$$e(G_1, G_2) = e(M) = \sum_{i=1}^{|P_1|} \min M(i,j) + \sum_{j=1}^{|P_2|} \min M(i,j) \tag{2.43}$$

Chapter 3

Noisy Iris Recognition

3.1 Iris anatomy

Iris can be schematically described as a multi-layered tissue stretching around the pupil in the frontal side of the eye as depicted in figure 3.1 [4].

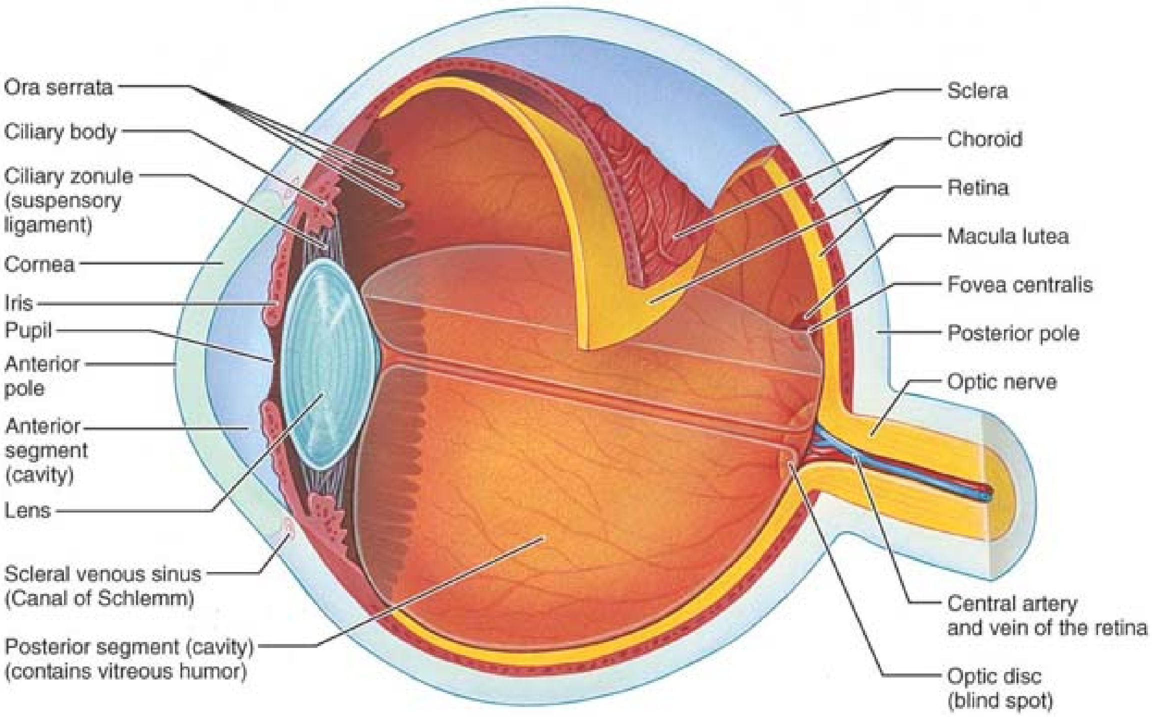

Figure 3.1: Diagrammatic view of the internal structure of the eye [38].

Formed during the gestation stage and completely defined at the eighth month, is during the early post-maternal life that its coloration changes [48]. Iris color is mainly determined by melanin concentration and distribution in its interior [23, 28]. Iris main function is to control the light level that enters the eye, through contracting itself, witch has repercussions on pupil size (figure 3.2).

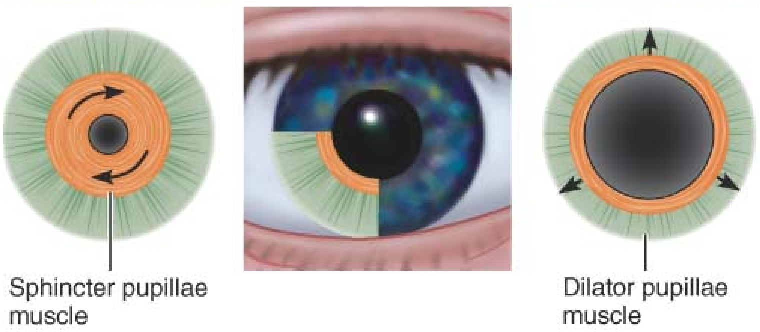

Figure 3.2: Pupil dilation and contraction, anterior view [38].

Iris patterns are formed based upon internal textures and its formations caused by both genetic and external influences, being therefore safely considered unique for each individual, despite the existence of a genetic relation of relatively importance (heritability) affecting their structure [35]. Although these patterns being relatively stable during lifetime, certain ocular and systemic diseases as well as drug use can cause on them considerable variations [48].

3.2 Wavelength and Color

Electromagnetic radiation includes all wavelengths, from long radio waves which length is measured in meters to the very short gamma waves with less than a nm ($1nm = 10^{-9}m$) [38]. Our eyes however, respond only to wavelengths between the $400 - 700nm$ located in the spectrum region named visible light or VW. Images captured at different wavelengths contain different amounts of useful information as they reflection properties vary accordingly to the illumination source.

Despite of iris radiance for light blue eyes being on VW relatively high, for darker pigmentation this value is extremely low within VW. The closer we get to the NIR wavelength, the more radiance values for dark brown and green eyes tend to increase.

On Vilaseca *et al.* work [63], they show that iris reflectance when illuminated with an halogen type lamp, also increases the closer we get to the NIR (figure 3.4). This

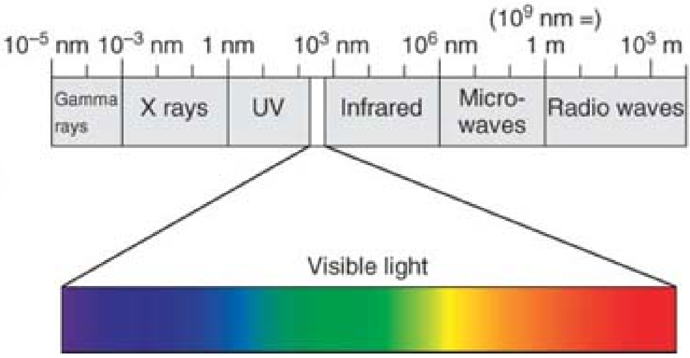

Figure 3.3: The electromagnetic spectrum, extending from the very short gamma waves to the long radio waves. Wavelengths are indicated in nanometers [38].

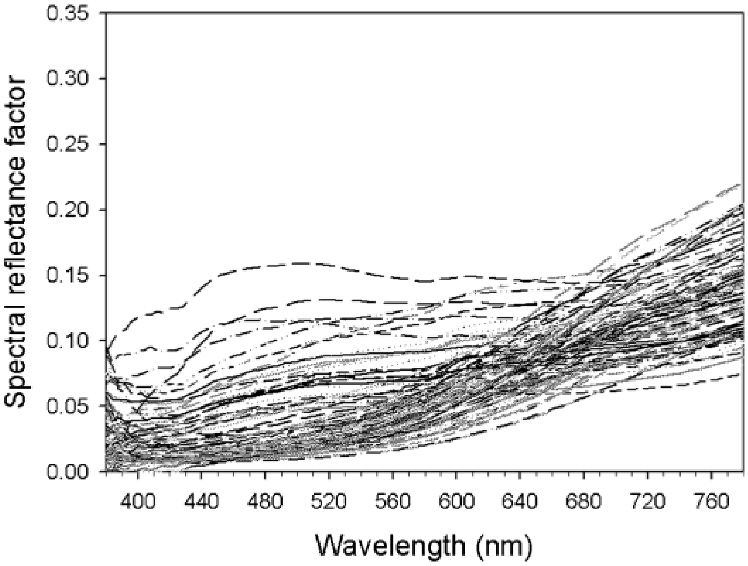

Figure 3.4: Spectral reflectance factors of 52 human irises [63].

increments, which allow a favorable definition of iris patterns on wavelengths closer to the NIR, are strongly related to the illumination type.

3.3 Less Constrained Image Capturing

Along with the methodologies presented on the State of The Art chapter (2), several authors produced efforts regarding less constrained image capturing. The "Iris-on-the-move" project [40] is the most relevant engineering of a less intrusive acquisition system, where acquisition is made under NIR as the subject walks through an access control point. Later on, *Honeywell Technologies* filed a patent [30] for a similar system providing at-a-distance iris recognition. Fancourt *et al.* [24] concluded on the feasibility of sufficiently high-quality image acquisition up to ten meters. Narayanswamy and Silveira [44] deliberately bluring images without change over a large depth-of-field, and then proceeding with digital processing, established a linear trade-off between STR and depth-of-field. Smith *et al.* [59] comparatively examined information captured in the NIR and VW spectra, addressing the use of multi-spectral data to improve recognition performance. Park and Kim [46] acquired at-a-distance images quickly, and Boddeti and Kumar [7] used correlation filters as a way to expand the depth-of-field. He *et al.* [26] studied the impact of different NIR wavelengths on final error rates. Yoom *et al.* presented a framework able to perform NIR acquisition up to three meters. Boyce *et al.* [9] identified the important role of iris pigmentation, studying acquisition wavelengths of revealed iris components.

The greatest drawback when intending to perform iris recognition in non-controlled conditions is clearly the associated noise. Figure 3.5 containing images from UBIRIS.v2, a non-cooperative iris database captured on VW (further details on section 3.4), makes that perceptible. On irises a and b, reflexes compromise a significant part of the image; c and d are mainly occluded by eyelids; and the last images (e and f) are too dark, either by the strong pigmentation of the iris or the lack of visible illumination. All those adversities lead to a reduction of class separability (Figure 3.6), and despite UBIRIS presents a more favorable behaviour than UBIRIS.v2, it is still far from the optimal scores given by NIR data-sets.

The good performance on iris recognition methods applied over NIR images comes essentially from the high level on texture detail that can be achieved (figure 3.7). Also, this kind of acquisition is, for its specifications, not so prone to strong reflexes.

Another restraining factor is the lack of subject cooperation, producing images where irises cannot be processed without proper corrections.

At the attempt to achieve iris recognition in VW without subject collaboration, the chosen methodology was to perform modifications over Daugman's approach [18], allowing it to achieve better performance in such adverse conditions. Although this method has been designed to operate over iris images acquired at NIR wavelengths, it has proofed itself to perform well in different types of images, specially with the iris accurately segmented and occlusions on the textures detected and localized in the

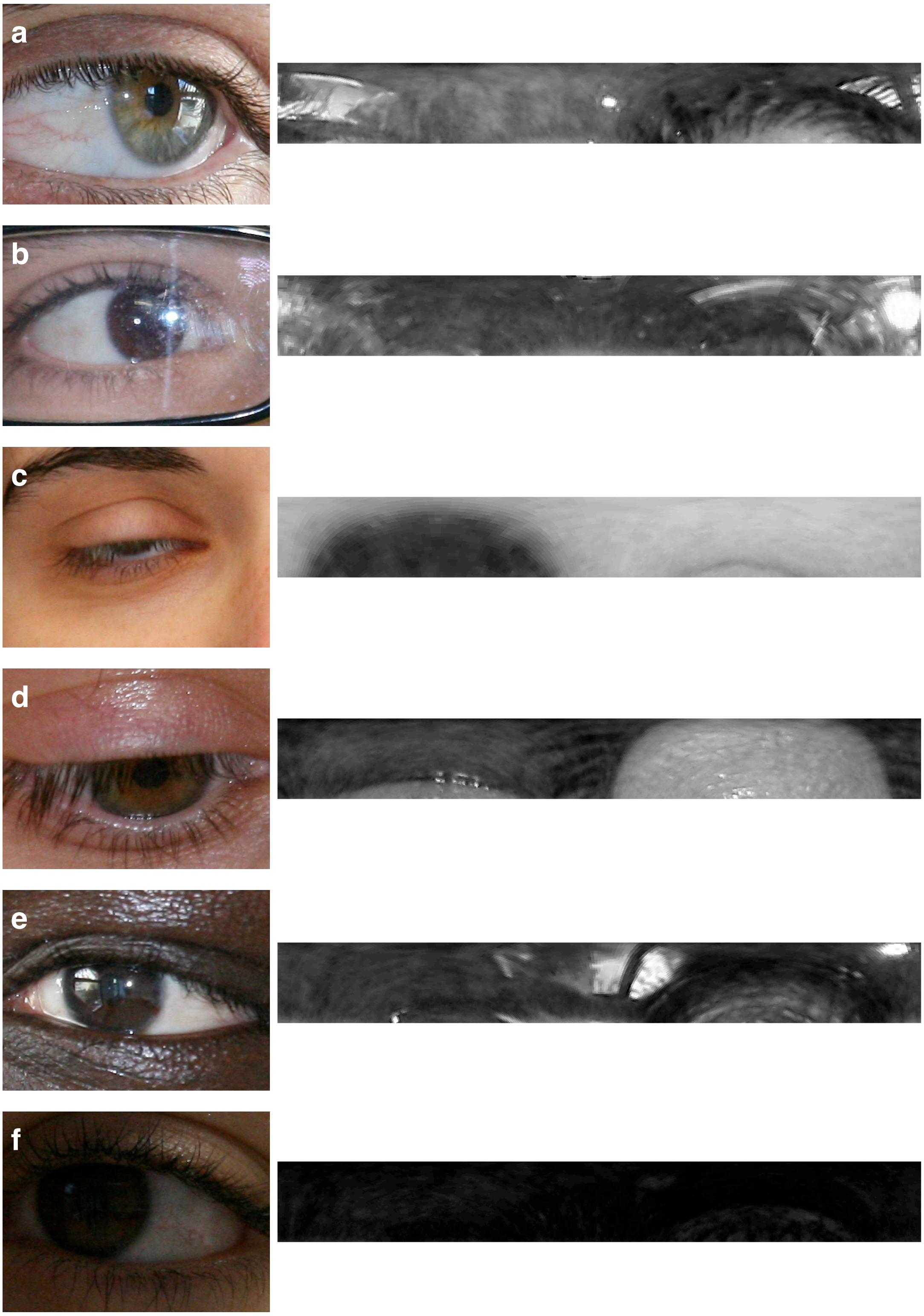

Figure 3.5: Illustration of strong noise presence in unconstrained captured and normalized images from UBIRIS.v2.

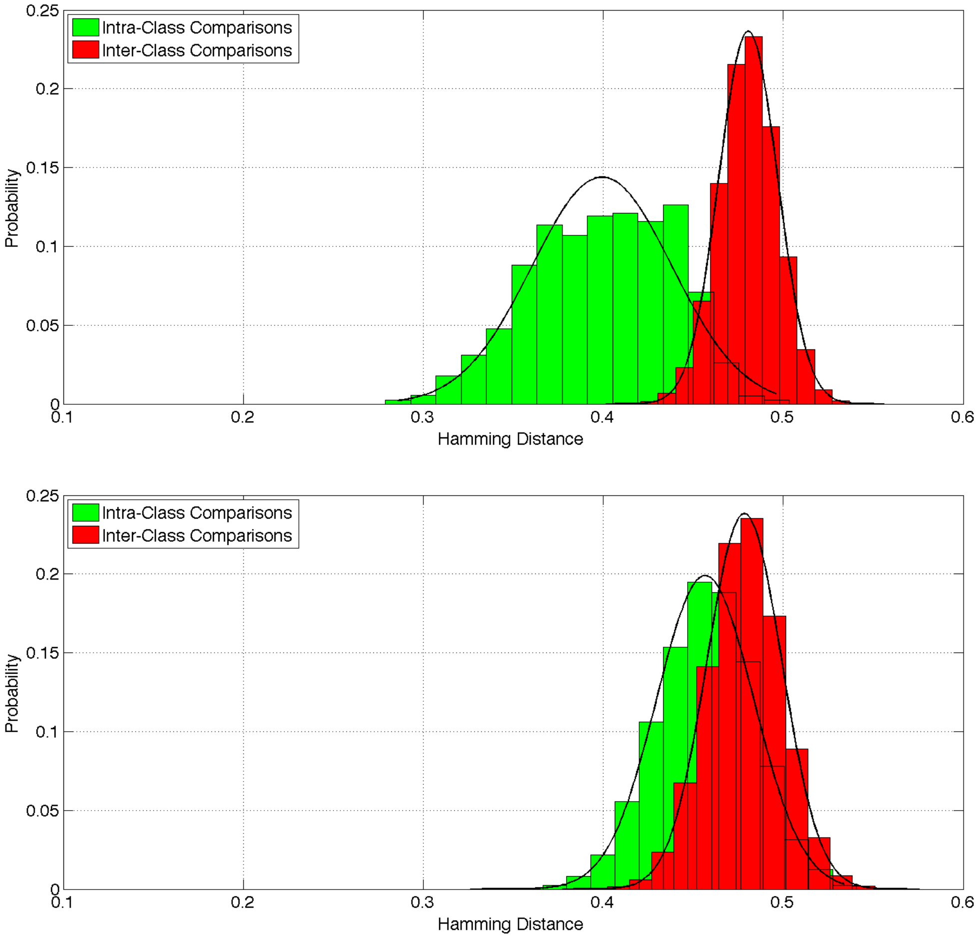

Figure 3.6: Hamming Distance distributions for 500 images of UBIRIS and UBIRIS.v2 data-sets respectively.

original and normalized data.

The first action aiming to attenuate the overall recognition error was centered in the normalization process, where a couple of interpolation algorithms impacts were quantified (section 4.1). At a further step the iriscode matching results were analyzed in both spatial and frequency domains (sub-sections 5.1.1 and 5.1.2). Finally, pattern classification procedures were put on operation to analyse earlier results which, duly formatted, produced satisfying results (section 5.3).

3.4 Datasets

There are several databases storing irises captured on several conditions and different acquisition protocols, being most of them built on images obtained on NIR (figure 3.7).

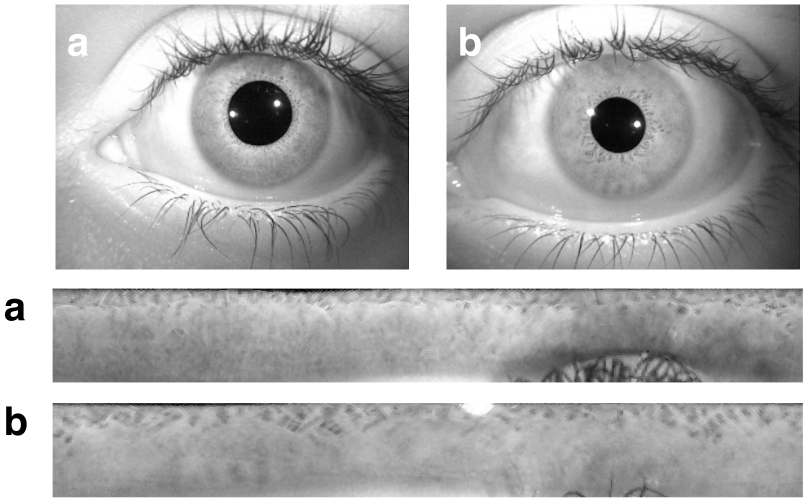

Figure 3.7: Sample images from the WVU data-set.

In our experiments, two different datasets were used: UBIRIS and UBIRIS.v2 (figure 3.8). The main justification is that our research concerns are focused in the feasibility of the recognition using VW iris images captured at-a-distance and on-the-move.

The UBIRIS database [55] was created at the Soft Computing and Image Analysis Lab (*SOCIA Lab*) of the University of Beira Interior. It consists on a set of VW noisy iris images, captured at close-up distance with user cooperation under VW. This dataset is intended for the development of robust iris recognition algorithms for biometric purposes and aims to *simulate* non-cooperative image acquisition, adding noise to the resultant images.

The UBIRIS.v2[54] was also created at *SOCIA Lab* and contains images *actually* captured at-a-distance with subjects facing different directions. The specific framework and setup used during UBIRIS.v2 database capturing, which are very similar to the ones present at BioRec [1], consisted as depicted in figure 3.9 on the necessary equipment installed on a lounge under both natural and artificial light sources. Subjects were moving towards the camera, while images were acquired

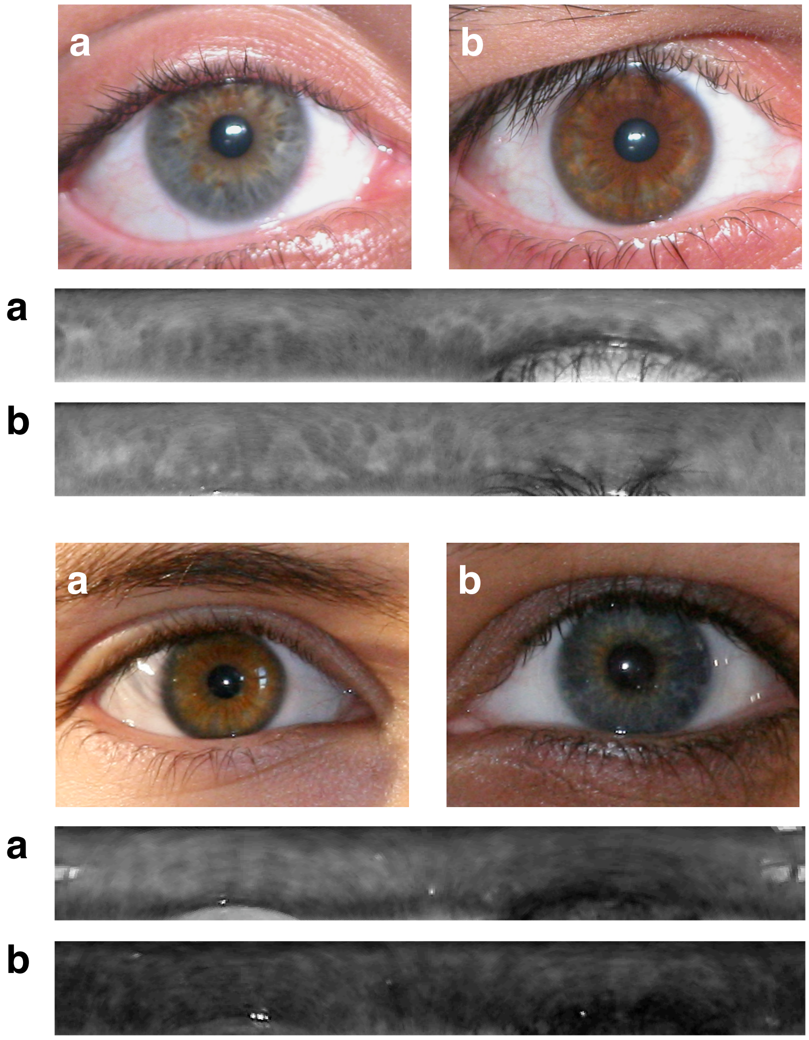

Figure 3.8: Sample images from the UBIRIS and UBIRIS.v2 data-sets respectively.

between four and eight meters. Those images contain several regions of the iris rings occluded by reflections, as well as significant iris obstructions due to eyelids and eyelashes. Location and orientation of the acquisition device and artificial light sources changed between the two distinct sessions that took place, in order to increase heterogeneity. Subjects were required to walk slightly slower than normal speed and look at several lateral markers, which forced head and eye rotation. The resulting images contain 90% Caucasian, 8% Black and 2% Asian people.

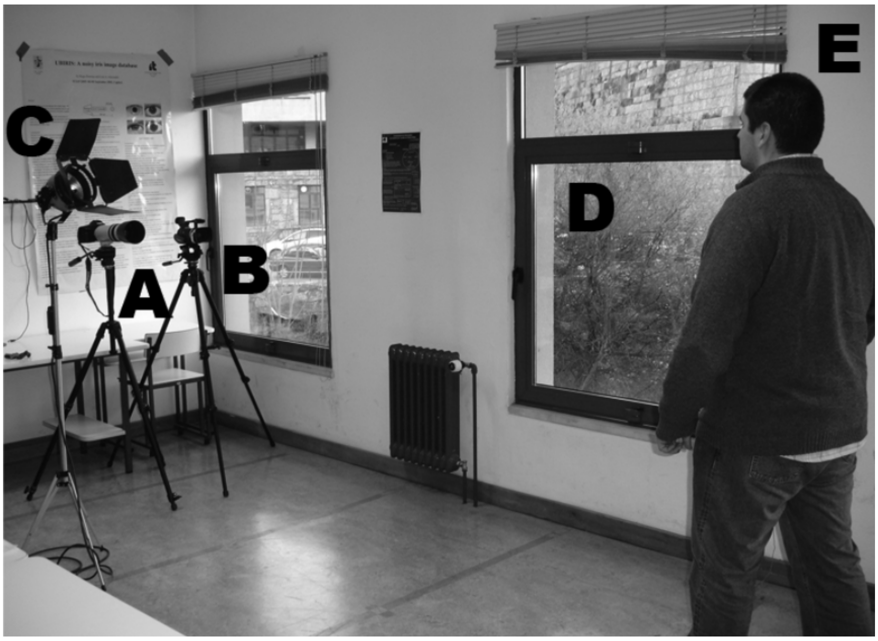

Figure 3.9: Overview of the used image acquisition framework (A,B) light sources (C,D) and subjects location (E) [54].

3.5 Experimental considerations

A few considerations must be exposed for better understanding of the experiments presented in the next chapters. For the interpolation trials (section 4.1) over 500 pictures (400 × 300 pixels) were used from each data-set.

On chapter 5, Featuring Encoding and Matching, three configurations were used. The first one consists, resembling the setup of Normalization procedures, of 500 images from UBIRIS.v2 without any kind of particular selection. A second arrangement consists of 175 images, also from UBIRIS.v2, captured with the subject looking at camera direction, which produced over 15000 comparisons. The third and last setup is composed by 100 images from the same database, with the subject also looking at the camera direction, but at relatively closer distances (4 to 6 meters). In every case, we selected a group of images that we believe to represent each data-set.

Prior to normalization, images were carefully segmented and iris and pupil centers and radius manually determined. In normalization related experiments (chapter 4), image noise was accounted for. At feature encoding and matching stage, and despite the previously obtained results, a central and contiguous region was extracted form the normalized image as illustrated in figure 3.10. This region, avoiding eventual pupil and eyelids occlusions, was conveniently considered noise-free and used for iriscode extraction. This particular option was taken to empower the spatial and frequency domains analysis.

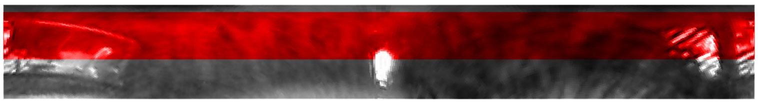

Figure 3.10: Illustration of the region for iriscode generation from the normalized image. The mentioned region is the one marked in red.

For iriscode extraction, only one optimized Gabor kernel configuration was used, as depicted in figure 3.11. Frequency, orientation and amplitude parameters were obtained through a thorough search, seeking decidability (2.10) maximization. In all trials, the available images were tested again each-others, producing intra- and inter-class comparisons.

We can further assume the compressed format all images were stored in upon capturing did not impact recognition performance, accordingly to the established by Ives *et al.* [31] and later on by Rackshit and Monro [56] and also Daugman and Downing [16] where they state that the trialled image compression methods do not significantly impact the recognition process.

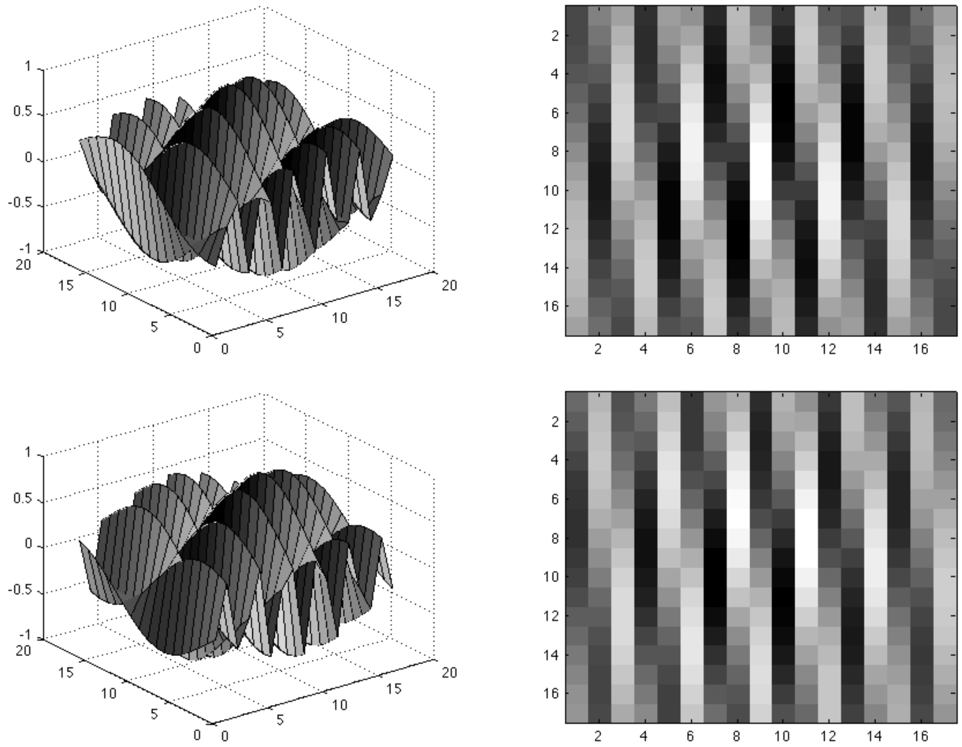

Figure 3.11: Illustration of the optimized Gabor kernel, used during iriscode extraction. Images on the left are perspective representations, and the ones on the right are over-top views. From top to bottom, Real and Imaginary parts are depicted respectively.

Chapter 4

Normalization

As mentioned, normalization process aims at achieving invariance to size, position and pupil dilatation in the segmented iris region.

In this work, we will focus on Daugman's rubber-sheet model [17], as explained in section 2.5. Regarding the location and segmentation of the iris, all used images were manually and accurately segmented, being known the center and radius of the pupils and irises. and detected all the regions that occlude portions of the iris.

The material included in this chapter was submitted for the 2009 International Conference on Computational Intelligence and Security (CIS'09) [2], and accepted for oral presentation and for publication in the main conference proceedings, published by the IEEE (appendix B).

4.1 Interpolation Repercussion

When performing rubber-sheet model normalization parametrized accordingly with authors' suggestion, it came to our attention that some of the iris pixels from the original image in Cartesian coordinates were not used in the construction of the normalized image. Also, the distribution of pixel usage despite the usual difference inherent from distancing to the center, was not regular (figure 4.1).

Therefore interpolation methods were tested to find out if its application could lead to better recognition rates, as stated in our recent paper [57].

On the translation between the cartesian and the pseudo-polar coordinate system we used three interpolation variants: the first - hereinafter called *no interpolation* -

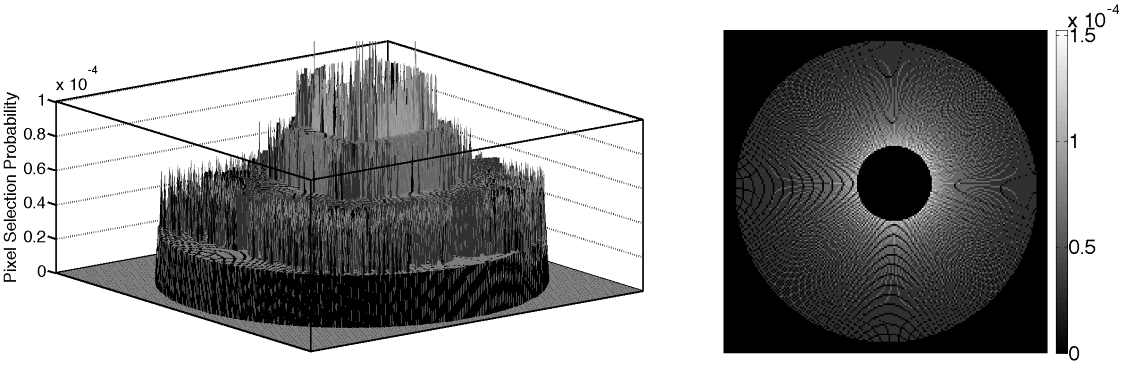

Figure 4.1: Perspective and over-top representation of the pixel selection probability over an UBIRIS image with no interpolation.

simply picks from the cartesian data the nearest neighbor pixel of $(x(r,\ \theta), y(r,\ \theta))$ (using L_2 norm). Also, we implemented two of the most well known interpolation variants: the bilinear and bicubic, as described in [49]. In these situations, instead of picking a single pixel $(x(r,\ \theta), y(r,\ \theta))$ in each step of the normalization process, we obtained the corresponding value according to its neighborhood, as below described.

Other types of interpolation (as the bicubic splines) were not the focus of our analyzis, essentially because we believe that the obtained results will be close to those obtained with the bicubic implemented variant.

4.1.1 Bilinear Interpolation

This is the simplest method to perform the two-dimensional approximation of missing values. It is given by:

$$y(x_1, x_2) = (1-t)(1-u)y_0 + t(1-u)y_1 + tuy_2 + (1-t)uy_3 \tag{4.1}$$

To determine the value $y_{ij} = y(x_{i1}, x_{2j})$ at some point, (4.1) is used, considering four surrounding points $y_o, ..., y_3$, defined counterclockwise starting from the lower left that obey the relations stated in (4.2) with i and j according to (4.3) and t, u as described in (4.4).

$$\begin{aligned} y_0 &\equiv y_{ij} \\ y_1 &\equiv y_{(i+1)j} \\ y_2 &\equiv y_{(i+1)(j+1)} \\ y_3 &\equiv y_{i(j+1)} \end{aligned} \tag{4.2}$$

$$\begin{aligned} x_{1i} \leq x_1 \leq x_{1(i+1)} \\ x_{2j} \leq x_2 \leq x_{2(j+1)} \end{aligned} \tag{4.3}$$

$$\begin{aligned} t &\equiv (x_1 - x_{1i})/(x_{1(i+1)} - x_{1i}) \\ u &\equiv (x_2 - x_{2j})/(x_{2(j+1)} - x_{2j}) \end{aligned} \tag{4.4}$$

4.1.2 Bicubic Interpolation

This interpolation method gives an higher order of smoothness, at a cost of use a higher number of pixels in each operation. That being said, bicubic interpolation for the function y given the four derivatives y_1, y_2, y_{12}, and is executed in two steps: determination of quantities $c_{ij}, i, j = 0, ..., 3$, combining a region of the image with the appropriate matrix and then use the following equations (4.5) with t, u given by (4.4).

$$\begin{aligned} y(x_1, x_2) &= \sum_{i=0}^{3} \sum_{j=0}^{3} c_{ij} t^i u^j \\ y_1(x_1, x_2) &= \sum_{i=0}^{3} \sum_{j=0}^{3} i c_{ij} t^{i-1} u^j (dt/dx_1) \\ y_2(x_1, x_2) &= \sum_{i=0}^{3} \sum_{j=0}^{3} j c_{ij} t^i u^{j-1} (du/dx_2) \\ y_{12}(x_1, x_2) &= \sum_{i=0}^{3} \sum_{j=0} i j^3 c_{ij} t^{i-1} u^{j-1} \end{aligned} \tag{4.5}$$

4.2 Results and Discussion

4.2.1 Cartesian Data Usage

Our first observation is that the interpolating methods used in the normalization process do impact over the usage of the iris pixels of the cartesian coordinate system in such translation into pseudo-polar coordinate system. To illustrate this, figure 4.2 shows the number of times each pixel located within the ring of a segmented iris region is used in the translation into the normalized data. Here, brighter pixels denote those more frequently accessed and the darker ones denote pixels with fewer accesses. The higher smoothness of the image corresponding to the bicubic interpolation is evident, as well evident discontinuities in the pixels' usage can be observed in the left image, obtained when used the no interpolation variant.

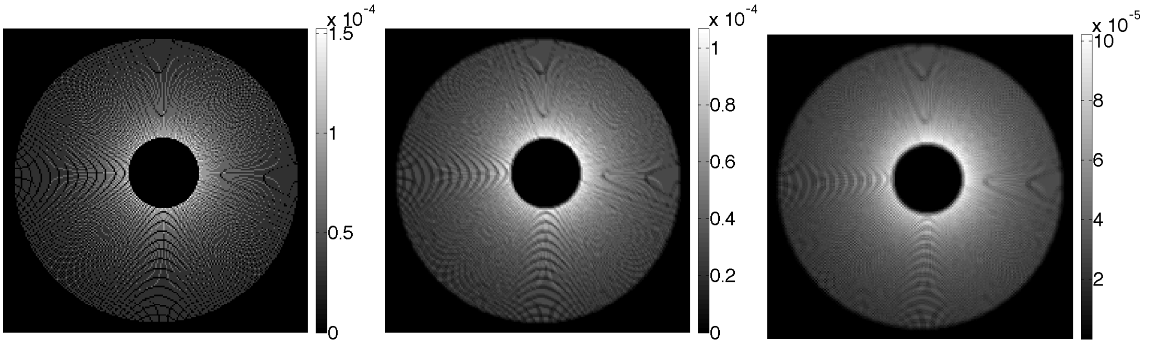

Figure 4.2: Representation of the number of times that each pixel of the segmented iris data is accessed during a normalization process, when using no interpolation (left), the bilinear (middle) and the bicubic (right) interpolation.

Not surprisingly, we observed that the average probability of a pixel to be used in the normalization process remains stable (due to the fixed size of the normalized block). However, the standard deviation obtained for the corresponding distribution becomes significantly lower when interpolation methods are used. In other words, pixel selection during a normalization process became more balanced, directly corresponding to the complexity of the interpolation process, i.e., to the number of pixels involved in a single interpolating operation.

The above described observations are better visible in figure 4.3, which gives a tridimensional representation for the probability that each pixel located within a segmented iris region is used in the interpolating operations of the iris normalization method. Again, the higher smoothness of the resultant graph for the bilinear and (more evidently) for the bicubic interpolating variant is evident.

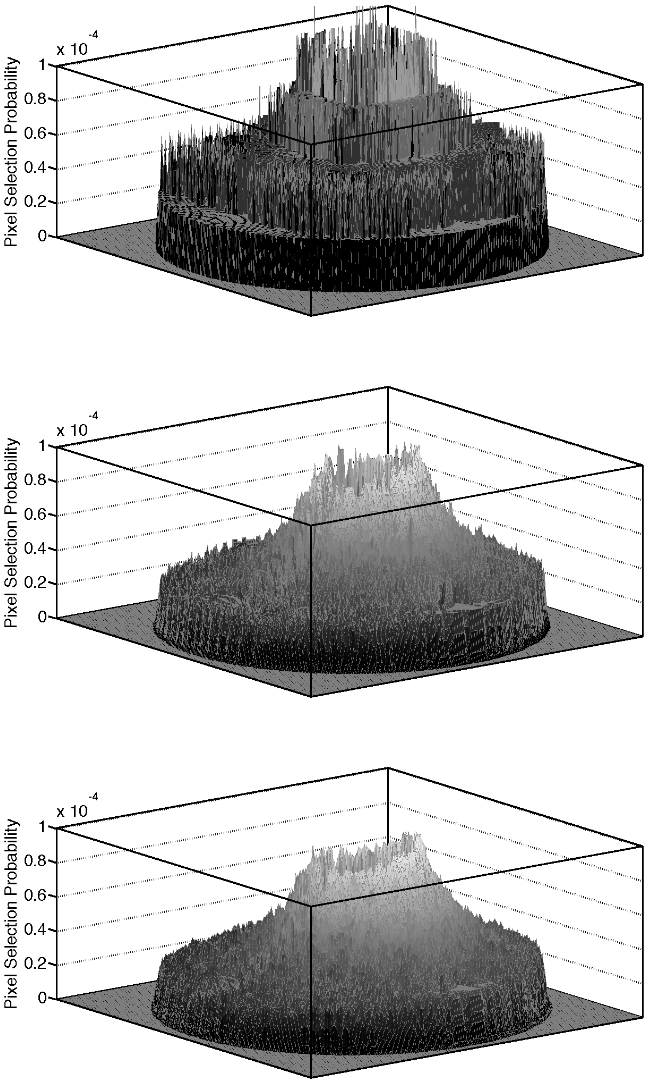

Figure 4.3: Perspective representation of the pixel selection probability over an UBIRIS image respectively with no interpolation (top), bilinear (middle) and bicubic interpolation (bottom).

Figures 4.4 and 4.5 give histograms about the probability for the pixels usage in the normalization stages, respectively in the UBIRIS and UBIRIS.v2 data sets. The horizontal axis gives the probability beans and the vertical gives the number of pixels that fall in the corresponding bean.

Regarding the UBIRIS dataset (highly normalized), it can be observed a considerable reduction in the amount of pixels that were never accessed during the normalization procedure (#pixels within the 0 probability bean), as well as an accentuation of the slope of the #Pixels value regarding the augment of the probability values.

The spread of the bar beans also suffers an decrement, from the no-interpolation to the bilinear and from this one to the bicubic variant. Using the bilinear interpolation, the probability for the pixel selection converged to a more evenly distributed iris data usage, where pixels are more likely to became part of the data used to extract the iriscode. Finally, when analyzing the bicubic interpolation, these changes are even more visible. The amplitude of the overall distribution was smaller and more homogeneous, as well as the resemblance between the probability for the pixel selection and a normal distribution.

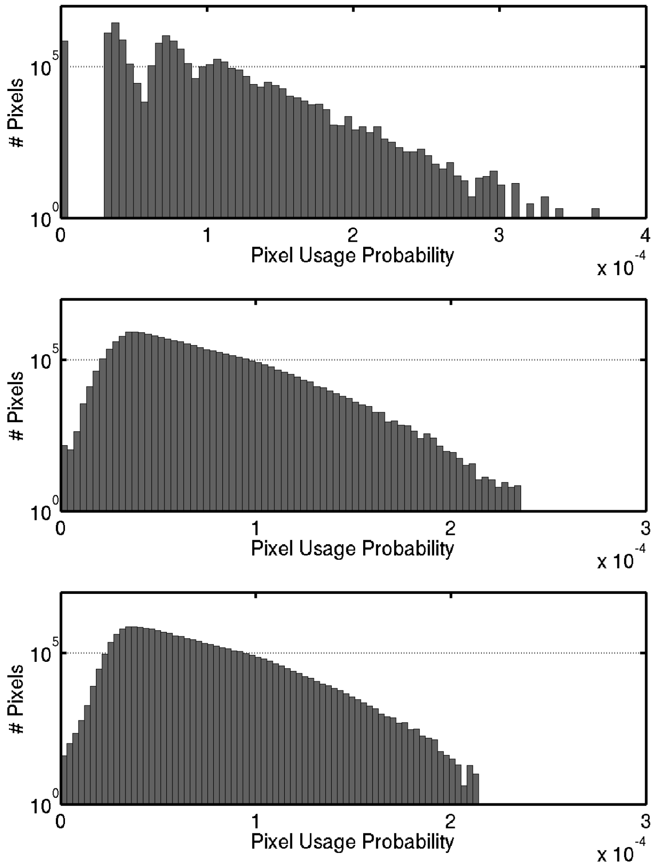

Figure 4.4: Overall probability for the iris pixel usage respectively with no interpolation (top), bilinear (middle) and bicubic interpolation (bottom) in the UBIRIS dataset.

Interestingly, the values obtained for the UBIRIS.v2 database were more close to

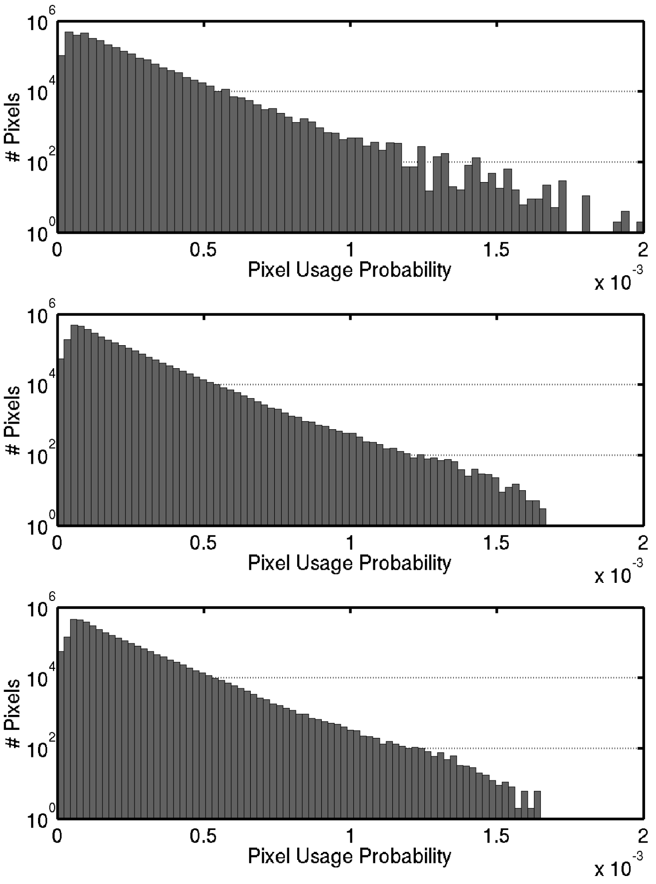

Figure 4.5: Overall probability for the iris pixel usage respectively with no interpolation (top), bilinear (middle) and bicubic interpolation (bottom) in the UBIRIS.v2 dataset.

each other, which we explain by the higher irregularity of this data set. However, the above stated observations for the first version of the database fit to the results obtained for this second version, as can be seen essentially by the higher spread of the histograms beans when no interpolation method was used.

4.2.2 Recognition Error Rates

Here, we give results about the variations of the recognition error rates, as function of the type of interpolating method used in the normalization process. We plot the Receiver Operating Characteristic (ROC) curves obtained when using each of the three interpolating variants on the two experimented datasets.

The first interesting observation is that the lowest error rates in the UBIRIS data-

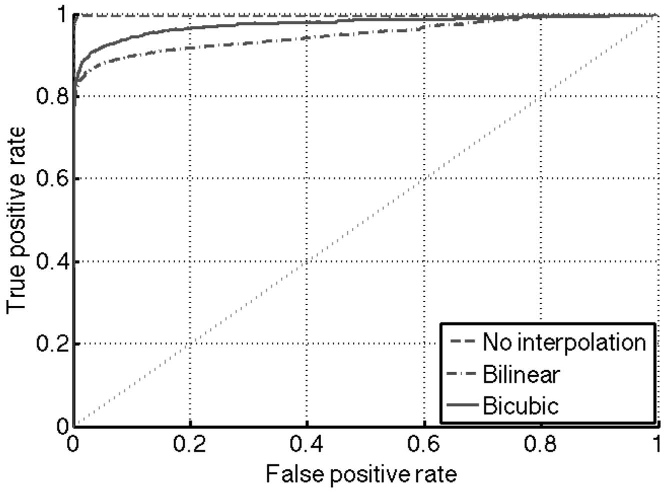

Figure 4.6: Receiver operating characteristic curve for different interpolation methods on UBIRIS dataset.

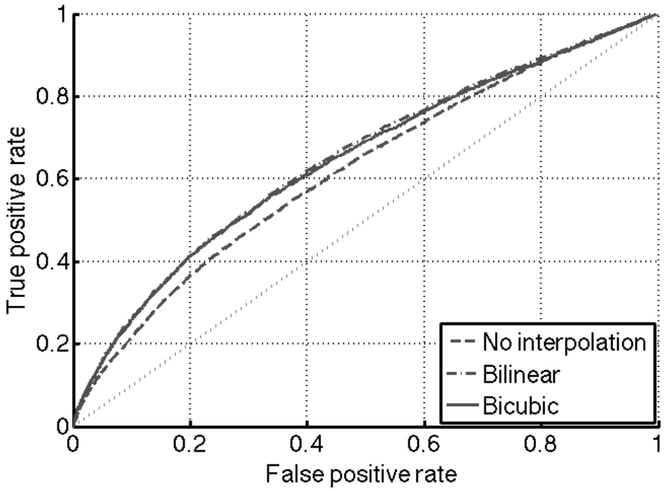

Figure 4.7: Receiver operating characteristic curve for different interpolation methods on UBIRIS.v2 dataset.

set were - clearly - obtained when no interpolation method was used (figure 4.6). Our interpretation is that less cartesian iris pixels are used in the normalized data, which minimizes the aliasing effects induced by the normalization process. Thus, in environments that propitiate the acquisition of less noisy images, the use of interpolating methods represents no-advantage, as showed by the difference between the results obtained when using no-interpolation and the interpolating methods.

Oppositely, for the UBIRIS.v2 images the better results were obtained when using the two types of interpolating techniques (figure 4.7). As this dataset contains higher levels of noise, the normalization process tend to be best succeed if more iris pixels are used in each normalization step, smoothing the corruption that non-detected noisy data carries to the normalized image.

Table 4.1: Iris pixel usage and decidability on different interpolation methods for UBIRIS and UBIRIS.v2 dataset.

	Interpolation	Iris Usage	Decidability
UBIRIS	None	$0.926 \pm 1.663 \times 10^{-4}$	4.390
	Bilinear	$0.999 \pm 2.294 \times 10^{-6}$	2.724
	Bicubic	$0.999 \pm 6.362 \times 10^{-7}$	2.779
UBIRIS.v2	None	$0.967 \pm 1.957 \times 10^{-4}$	0.410
	Bilinear	$0.986 \pm 1.286 \times 10^{-4}$	0.519
	Bicubic	$0.988 \pm 1.209 \times 10^{-4}$	0.496

Finally, the previously described usage of the iris pixels of the cartesian coordinate system as function of the interpolation method is resumed in Table 4.1, with corresponding confidence intervals of 95%. Also, it is given the decidability (2.10) of the corresponding pattern recognition systems. That - again - confirms the previously stated conclusions: the use of image interpolation techniques on less noisy images seems not to represent any surplus in the final error rates. However, if images are highly noisy, interpolation techniques can slightly increase the recognition accuracy.

Chapter 5

Feature Encoding and Matching

As shown before, Daugman's method performance substantially degrades when applied to non-ideal iris images, despite of interpolation application at the normalization stage. Figure 3.6 clearly depicts how intra- and inter-class distributions come together under such conditions, and the work on this chapter is then aimed to increase their separability modifying the feature encoding and matching stage.

At the matching stage, Daugman applies a quantifying measure that relates the overall ratio of concordant iriscode data over the hole iris. Having two matrices with the same size of iriscode, where the punctual result of the comparison between two irises is represented, it is clear that no matter how these results are distributed, the HD (2.9) gives the same weight to both of them as long as they have an equal amount of concordant spots.

In our work we propose a different yet complementing approach: performing analysis in both spatial (sub-section 5.1.1) and frequency (sub-section 5.1.2) domains, we extract features which, upon selection, will feed a pattern classification method to reach a final result.

5.1 Feature Extraction

At figure 5.1 four images are depicted, two for each subject. The intra-class comparisons between the legitimate irises produced however high HD values, which consecutively led to erroneous classifications as impostors. We can clearly observe, here again, the presence of eyelid and reflection occlusions and yet the existence of “clean” regions that weren’t affected and are therefore clearly visible. This kind of observations had an important role on choosing the approaches we describe along the remaining of this chapter.

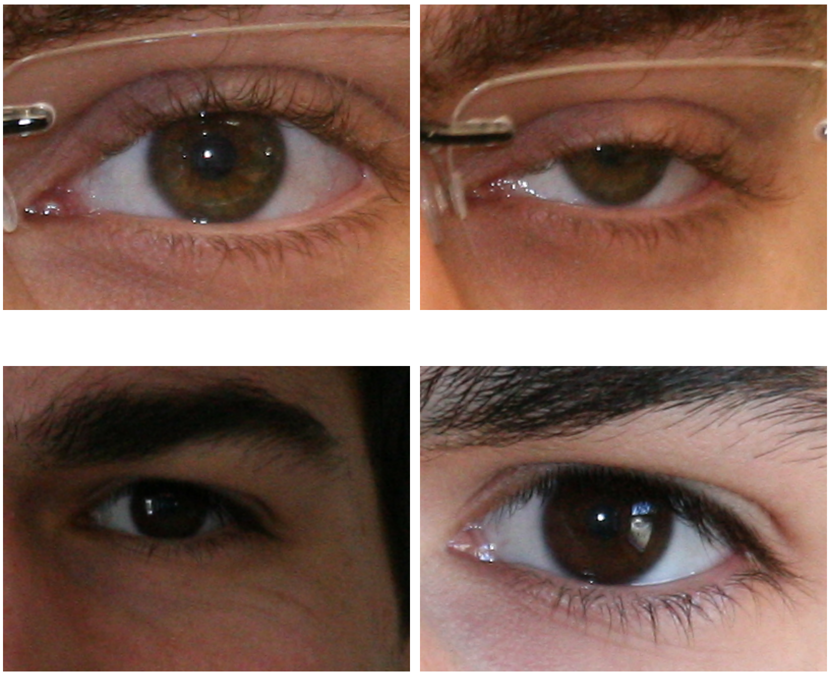

Figure 5.1: False reject illustration on UBIRIS.v2 database. The first couple images had an HD of 0.517, and second ones about 0.494

5.1.1 Spatial Domain Analysis

Our first proposition at this stage was aimed at finding contiguous regions with an high matching rate, since theoretically those regions would have more interest that the same quantity of concordant bites dispersed by the whole area.

Figure 5.2: Iriscode matching result illustration. The delimited region correspond to an high concordance area.

Figure 5.2 illustrates two matching results between four iriscodes. As they both contain a similar rate of concordant points (represented in black), their HD will be the same. Despite that, on the right half of the bottom image there is clearly a contiguous region of matching points. Would that region suffice to conclude that we are in the presence of a positive match, even if Daugman's method tell us otherwise?

To test that theory, we first proceeded with the convolution between the matching result and a bank of Haar filters of different sizes. That allowed us to obtain matrices of values representing the level of similarity in a window the same size of the used filter, and stress which would be the best window size to decide, with legit confidence, whether in presence of a positive match or not. For this first trial stage only the global maximum were accounted for. However, such simple and clear analysis did not produce the expected result, as the maximum itself did not allow a clear separation between the inter and intra-classes.

A second step was to analyse not only the maximum value, but rather to use a single Haar filter to build a 25 bin histogram, populated with result values from the convolution. As then came to our understanding when averaging the histogram population for both inter and intra-classes, there was a noticeable separation (figure 5.3). Intra-class comparisons tend to originate more windows with an high level of matching, as the inter-class generates less concordant bits in the same windows.

Regardless, due to the great value deviation, this distinction was not able to produce

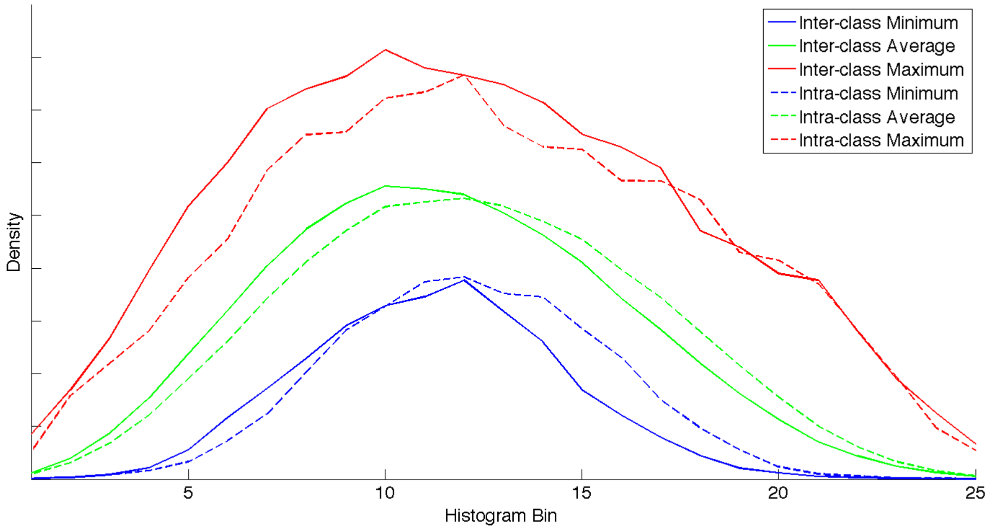

Figure 5.3: Histogram bin statistics for frontal captured UBIRIS.v2 images Haar filter convolution.

a remarkable classifier *per se*, but instead became features with further use in section 5.3. Let us have in mind that the increment in dimensionality would help to better describe a separation hyper-plan from the different classes.

5.1.2 Frequency Domain Analysis

Another analysis was focused on the frequency of the signal that describes the matching occurrence. We were based on the hypotheses that the matching result between the iriscodes tends to have a random distribution of concordant and non-concordant bites when facing an impostor comparison. When a legitimate match is in analysis by other side, the distribution would hopefully behave differently, presenting a lower frequency pattern in signal propagation.

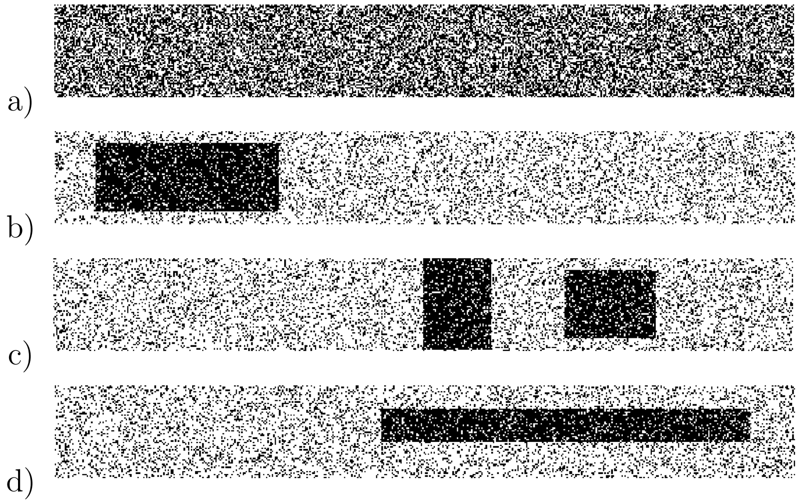

Figure 5.4: Iriscode matching result illustration for different strongly concordant areas. Black dots represent a positive match bit. The first image (a) contains randomly distributed concordant bits, and the following ones contain the same overall proportion of concordance ($HD = 0.5$), but with regions clearly more identical.

Figure 5.4 represents, for illustration purposes and in exaggerated proportions, several match results between irises. In the first image (a) of this picture, we have a randomly distributed 50% concordance level, which produces a 0.5 HD and therefore result in an impostor classification. The remaining images contain the same overall proportion of concordant bits, distributed with larger concentration in several relatively small contiguous regions. Assuming that these regions are caused by the fact we are facing legitimate comparisons (between different images of the same iris)

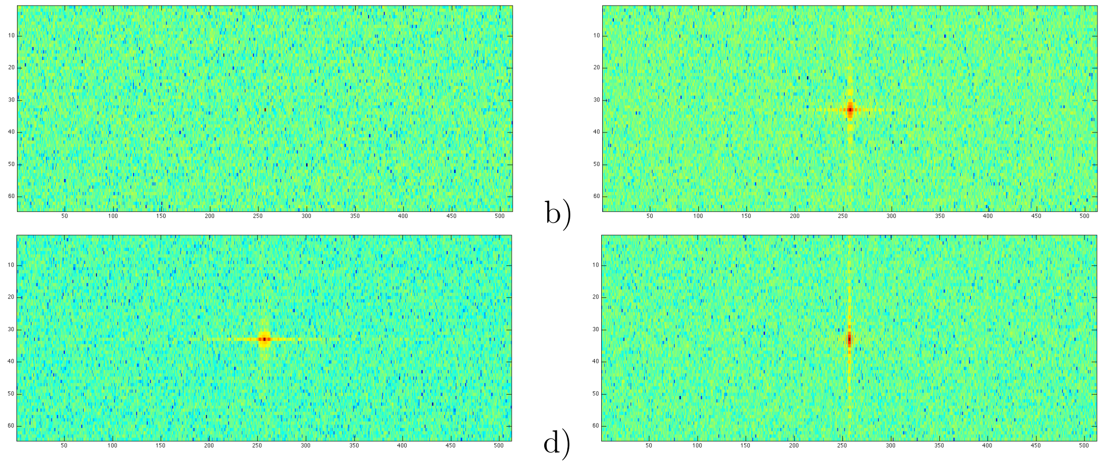

a) b) c) d)

Figure 5.5: Frequency analysis for different strongly concordant areas - over-top representation. This illustrative results are for the respective images at figure 5.4

which are somehow occluded on most of their area, classifying those comparisons are impostors based upon the HD would result in false negatives.

When analysing the Fast Fourier Transform (FFT) for these comparisons (figures 5.5 and 5.6), and as expected, there are clear stronger peaks in the region representing lower frequencies for (b), (c) and (d), which are not present in (a) and are caused by the mentioned high concordance areas. Those peaks are present, although with different shapes, independently of region size, orientation and location. This was the principle that motivated our analysis in the frequency domain.

A modification to the Daugman's approach was introduced at this stage: the subtraction of the signal-wise binary conversion step, and the replacement of the XOR operation with the difference between the coefficients.

The FFT was then applied both for the *traditional* binary match result and the differential one. The most remarkable results were obtained for the second one, producing the results depicted in figures 5.7 and 5.8, where we can see a predominance of null frequencies, at the center of the matrix, followed by two distinct peaks at both left and right sides. These features are however present in both inter-class and intra-class, so no clear distinction can be established from them. In the intra-class Fourier analysis, there is a strongly marked occurrence at the zero-frequency that goes along all the y axle. Once again, the high variation of values does not allow a linear rule to be deduced.

The resulting matrices (figures 5.7 and 5.8) were decomposed in sixteen sub-regions

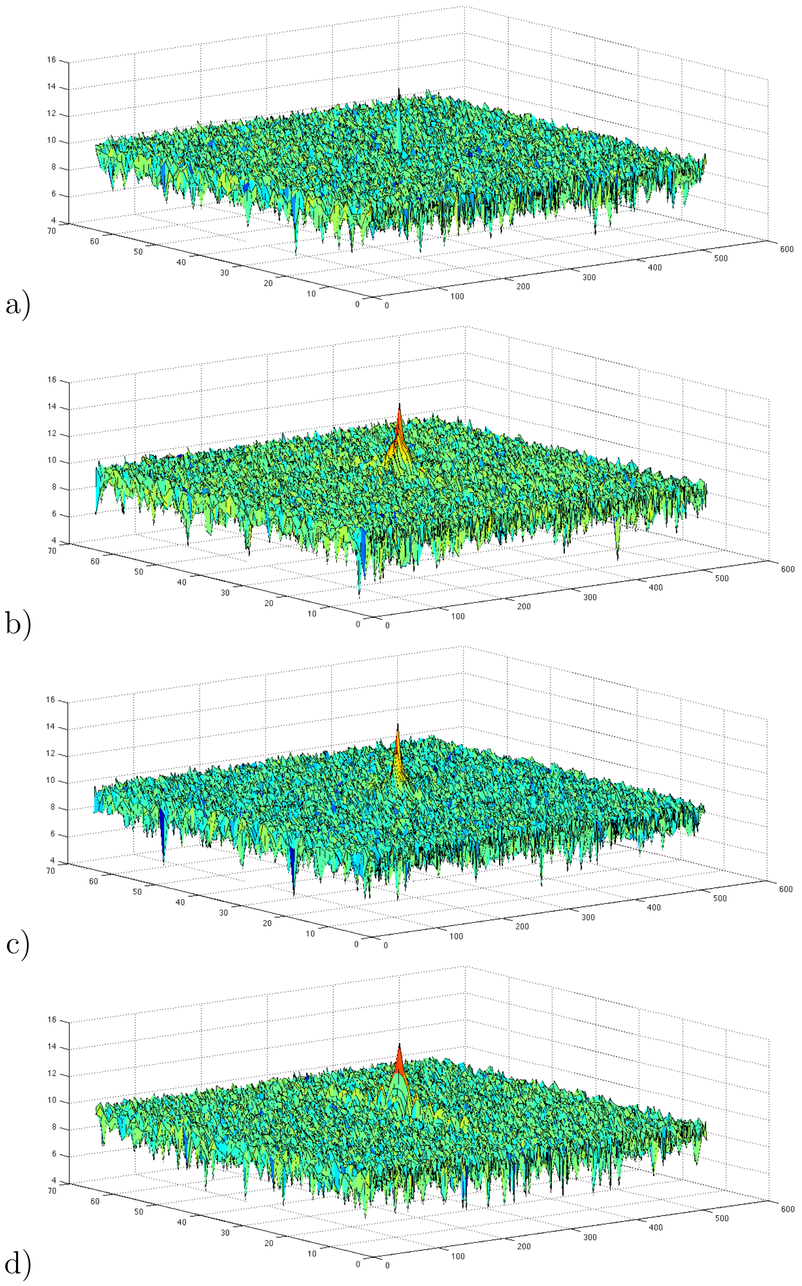

Figure 5.6: Frequency analysis for different strongly concordant areas - over-top representation. This illustrative results are for the respective images at figure 5.4

each, regularly distributed in a 8×4 grid. From every single region, a set of attributes were ascertained: minimum and maximum values, average and standard deviation and, finally, entropy.

Since the central values contain, presumably, important information that the anterior windowing was unable to properly process, another method was used to extract

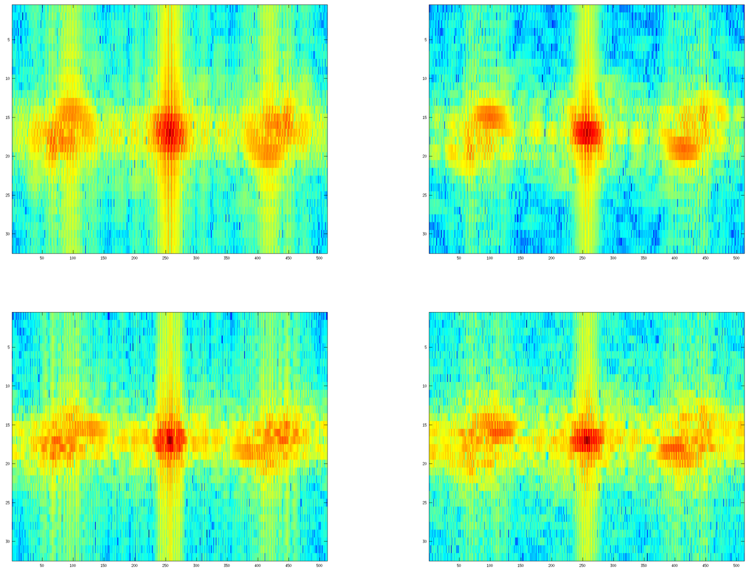

Figure 5.7: Sample frequency analysis depict for intra-class iriscode subtraction. Images on the left represent imaginary part, and on the right the corresponding real part.

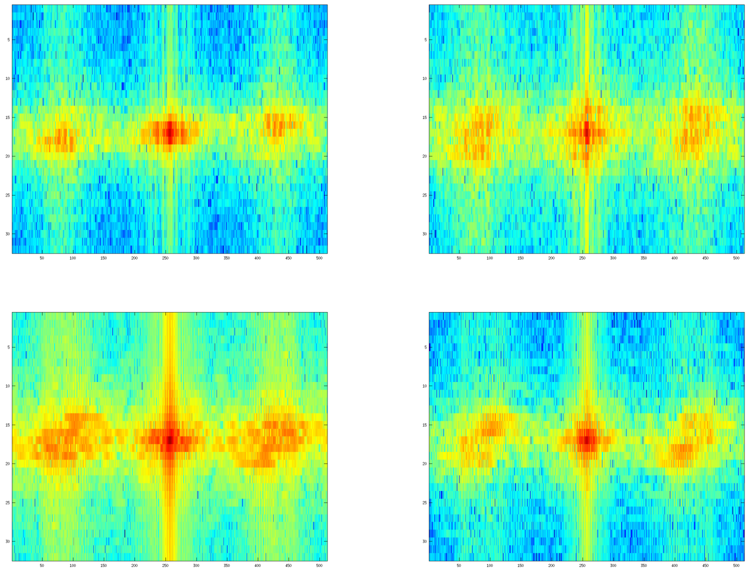

Figure 5.8: Sample frequency analysis depict for inter-class iriscode subtraction. Images on the left represent imaginary part, and on the right the corresponding real part.

features from this area. Let us have a $P \times N$ window A centered in the $P \times M$ matrix which contains the noticeable central shape with $P = 2M/8$. Ten features F_i are then extracted as explained in (5.1b), being them the density of values higher than ten different thresholds T_i, evenly spaced within the limits.

$$T_i = \min(A) + i\frac{\Delta A}{10} \tag{5.1a}$$

$$F_i = \sum_{m=1}^{P}\sum_{n=1}^{N} \operatorname{sgn}\left(x_{(m,n)} - T_i\right) \tag{5.1b}$$

With $\Delta A = \max(A) - \min(A)$, the values $x_{(m,p)} \in A$ are present at coordinates (m, p) and $i = 1, 2, ..., 10$.

5.2 Feature Selection

The purpose of dimensionality reduction is to hold most of the “intrinsic information” from data samples in a low-dimensional space. Upon accomplishing this goal, the newly obtained data representation can be used for the succeeding tasks [60]. Also, reducing the dimensionality of the problem causes a decrease of computational cost and data noise [21].

From the set of features we possess, four of them were immediately eliminated since they contained no information at all. The ones in question were the convolution maximums from 4×4 and 6×6 Haar filters, and the densities of values at the central shapes, when using the two highest thresholds.

The remaining features were then submitted to some well known dimensionality reduction methods, and their results compared.

5.2.1 mRMR - minimum-Redundancy, Maximum Relevance

The identification of features best describing the target classes is essential for classification error minimization [47].

Peng *et al.* [47, 21, 20] propose a feature sorting method based on their relevance, assuring that they contain a minimum of redundancy when compared to each other. Feature relevance is obtained seeking attributes that satisfy equation (5.2), where

$I(x_i, c)$ is the mutual information between feature x_i and the class c.

$$\max D(S, c),\ D = \frac{1}{|S|} \sum_{x_i \in S} I(x_i, c) \tag{5.2}$$

Mutual information is based on probability density functions $p(x_i)$, $p(c)$ and $p(x_i, c)$ accordingly to equation (5.3), being S the feature set we are looking for, containing $\{x_i\}$ features.

$$I(x_i, c) = \iint p(x_i, c) \log \frac{p(x_i, c)}{p(x_i)p(c)} dx_i dc \tag{5.3}$$

It becomes clear that feature selection based on this criteria alone produces a set where they tend to be redundant (*i.e.* with a large dependency among theirselves). This situation is solved introducing a second metric with the power to quantify that redundancy, based on the fact that when facing two redundant features, by removing one of them we produce a low variation on the set discriminant power. The rule to select mutually exclusive features is then stated in equation (5.4).

$$\min R(S),\ R = \frac{1}{|S|^2} \sum_{x_i, x_j \in S} I(x_i, x_j) \tag{5.4}$$

The criteria that combines this two constraints is called minimum Redundancy Maximum Relevance (mRMR), optimized simply by Φ when equation (5.5) is satisfied.

$$\max \Phi(D, R),\ \Phi = D - R \tag{5.5}$$

The application of mRMR to our previously obtained features led to the results at table 5.1, where features are represented as follows:

- Hamming Distance: Self-explanatory (equation 2.9);
- Haar Max ($i \times i$): Global maximum for matching result convolution with a $i \times i$ Haar filter;
- Haar Hist (bin i): Value at the i^{th} bin of Haar convolution histogram;
- FFT {Ent|Mean|Min|Max|Std} (x,y): FFT entropy (Ent), mean (Mean), minimum (Min), maximum (Max) or standard deviation (Std) for the window starting at coordinates (x, y);

- Ratio {Real|Imag} ($i = k$): Central shape density, for the FFT real or imaginary part, with a threshold T_k (equation 5.1b).

Table 5.1: Feature sorting accordingly to the mRMR criteria. Full results exhibited at appendix A.

Order	Feature	Score	Order	Feature	Score
1	Hamming Distance	0.351	26	FFT Std $(641, 1)$	-0.833
2	Haar Max (8×8)	-0.015	27	Haar Hist (bin 22)	-0.861
3	Ratio Imag $(i = 9)$	-0.065	28	FFT Min $(513, 17)$	-0.874
4	Haar Max (10×10)	-0.057	29	FFT Std $(1, 9)$	-0.894
5	Haar Max (12×12)	-0.157	30	FFT Min $(769, 1)$	-0.909
6	Ratio Real $(i = 9)$	-0.160	31	Haar Hist (bin 5)	-0.932
7	Haar Hist (bin 1)	-0.217	32	FFT Ent $(769, 9)$	-0.947
8	Haar Hist (bin 25)	-0.294	33	FFT Std $(129, 17)$	-0.966
9	Ratio Imag $(i = 8)$	-0.336	34	FFT Min $(769, 25)$	-0.977
10	Haar Max (14×14)	-0.347	35	FFT Ent $(257, 17)$	-0.985
11	Ratio Real $(i = 1)$	-0.403	36	FFT Std $(513, 25)$	-0.995
12	Ratio Real $(i = 8)$	-0.441	37	FFT Min $(385, 1)$	-1.008
13	Ratio Imag $(i = 1)$	-0.479	38	FFT Std $(129, 1)$	-1.016
14	Haar Max (16×16)	-0.522	39	Haar Hist (bin 21)	-1.024
15	FFT Std $(769, 9)$	-0.570	40	FFT Std $(513, 9)$	-1.036
16	Ratio Real $(i = 6)$	-0.601	41	Ratio Real $(i = 5)$	-1.045
17	Haar Hist (bin 23)	-0.632	42	FFT Std $(385, 25)$	-1.054
18	Haar Hist (bin 2)	-0.659	43	FFT Ent $(1, 9)$	-1.063
19	FFT Std $(769, 25)$	-0.688	44	FFT Min $(769, 9)$	-1.071
20	FFT Std $(385, 1)$	-0.714	45	FFT Min $(257, 25)$	-1.077
21	FFT Min $(129, 1)$	-0.740	46	FFT Std $(897, 9)$	-1.087
22	Haar Hist (bin 24)	-0.752	47	Ratio Real $(i = 7)$	-1.093
23	Haar Max (18×18)	-0.766	48	Ratio Imag $(i = 6)$	-1.100
24	FFT Min $(129, 17)$	-0.796	49	FFT Min $(257, 1)$	-1.109
25	Ratio Imag $(i = 7)$	-0.813	50	Haar Hist (bin 8)	-1.115

As we can see, the HD obtained from Daugman's method is the most relevant attribute. The features obtained by the convolution between the matching result and the Haar filters also play an important role, being generally best classified than the ones from the frequency domain analysis. In this last one, the ratio mentioned in equation (5.1b) (*i.e.* frequencies closer to null) stands out. As for window statistics ascertained from FFT, the most important are clearly the standard deviation and minimums outlying the value peaks.

From the over 200 features which are now ordered, instead of choosing a fixed small size subset, we selected various sets which were fed to the dimensionality reduction methods we now present.

5.2.2 PCA - Principal Component Analysis

Component analysis is an unsupervised method for data dimensionality reduction [22]. The most famous example of dimensionality reduction is Principal Component Analysis (PCA) [65].

In PCA, also known as *Karhunen-Loéve transform*, we attempt to represent a d-dimensional space through a lower dimension one with fewer degrees of freedom, reducing as before stated both space and time complexities, and removing some "noisy" directions. To do so, we start by determining the d-dimensional mean vector μ and the $d \times d$ covariance matrix Σ. Then, the e_i eigenvectors and δ_i eigenvalues are computed and sorted by decreasing eigenvalues. Finally, we chose the k larger eigenvectors to produce a $k \times k$ matrix A which will allow a data conversion by equation (5.6).

$$x' = A^t(x - \mu) \tag{5.6}$$

PCA is an unsupervised technique and, therefore, does not account for class information during the dimensionality reduction process.

5.2.3 LDA - Linear Discriminant Analysis

Linear Discriminant Analysis (LDA) (alias Fisher Discriminant Analysis (FDA)) uses class information to find a sub-space that best discriminates them [11].

Given independent features, LDA makes a linear combination of those who yield the largest mean difference between the desired classes [39]. In a general way, having samples for all classes, two measures are defined: *within-class* scatter matrix (5.7) and *between-class* scatter matrix (5.8).

$$S_w = \sum_{j=1}^{c} \sum_{i=1}^{N_j} (x_i^j - \mu_j)(x_i^j - \mu_j)^T \tag{5.7}$$

$$S_b = \sum_{j=1}^{c} (\mu_j - \mu)(\mu_j - \mu)^T \tag{5.8}$$

where x_i^j is the i-sample of class j, μ_i is that class mean, c is the number of classes, N_j is the number of samples from class j and μ is the mean of all classes.

The objective is then to maximize the *between-class* measure, while minimizing the *within-class* one. That can be achieved through $\frac{\det|S_b|}{\det|S_w|}$ ratio maximization.

Opposing PCA, LDA produces the results depicted in figure 5.9.

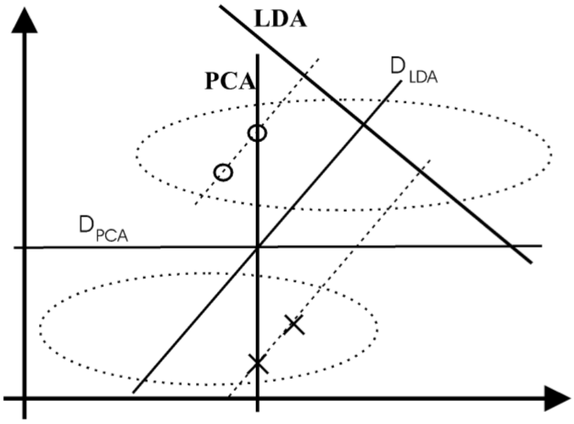

Figure 5.9: Conceptual depiction of PCA classification versus LDA. D_{PCA} and D_{LDA} represent decision thresholds [39].

5.2.4 LFDA - Local Fisher Discriminant Analysis

The previously mentioned LDA tends to provide undesired results when samples from the same class are distributed among several distinct clusters, *i.e.*, multimodal [60]. To solve this problem, Sugiyama proposed in his paper [60] a new dimensionality reduction method: Local Fisher Discriminant Analysis (LFDA).

This new approach also considers data arrangement, so that even multimodal sample distributions can be correctly structured, combining a supervised reduction algorithm (FDA) with the Locally Preserving Projection (LPP).

The LPP, proposed by He and Niyogi [25], is a dimensionality reduction method that preserves neighbourhood structure on sample data. It is unsupervised and presented as an alternative to PCA.

In figure 5.10 we can see a comparative reduction example between FDA, LPP and LFDA. As mentioned before, it is clear that FDA is unable to adapt on multimodal situations.

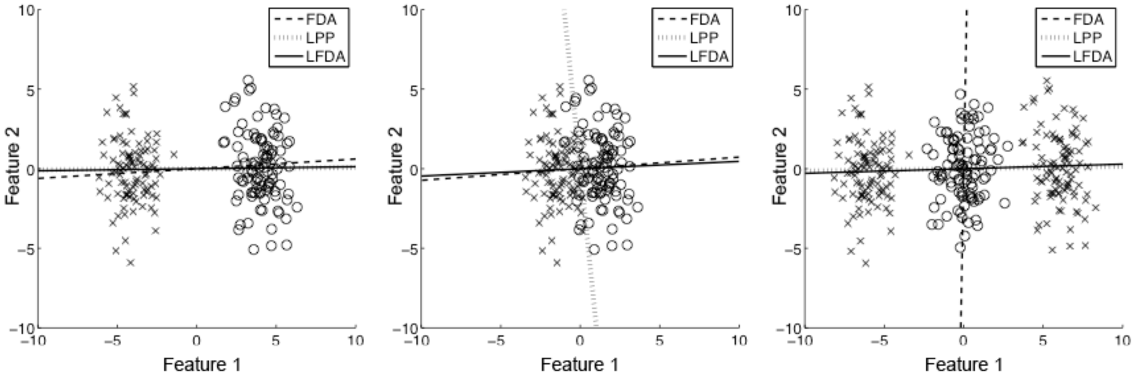

Figure 5.10: Examples of dimensionality reduction by FDA, LPP and LFDA [60].

LFDA evaluates the *within-class* scatter (5.7) and the *between-class* scatter (5.8) in a local way, through which the class separability and local structure preservation are simultaneously maximized.

In our experiments, we were able to conclude LFDA application to mRMR best features to be the most overcoming, when compared to both PCA and LDA.

5.3 Pattern Classification

At the pattern classification stage, the recently acquired and selected features were submitted to specific algorithms, aiming knowledge extraction from those attributes. Different approaches results were examined from the different methods we now describe and, as we will discuss furthermore at the end of this chapter, the used pattern classification processes converge to the conclusion that iris recognition under the VW slice of the electromagnetic spectrum is feasible without user cooperation.

5.3.1 Naive Bayes

The Naive Bayes (NB) is one of the most efficient algorithms in knowledge extraction from data [71]. While being an highly practical Bayesian learning method, its performance in some domains can even compare to a neural network or decision tree learning [41]. In this subsection, we introduce the basis of NB.

Having an example E represented by a tuple of features $(x_1, x_2, ..., x_n)$, where x_i is the value for attribute X_i, and one binary class C which assumes the value c, the probability (5.9) can be established.

$$p(c|E) = \frac{p(E|c) \cdot p(c)}{p(E)} \tag{5.9}$$

We can then recognize E belonging to $C = 1$ if and only if we verify (5.10), with $f_b(E)$ being the Bayesian classifier.

$$f_b(E) = \frac{p(C = 1|E)}{p(C = 0|E)} \geq 1 \tag{5.10}$$

Assuming that we are facing independent features given the class value, that is,

$$p(E|c) = p(x_1, x_2, ...x_n|c) = \prod_{i=1}^{n} p(x_i|c), \tag{5.11}$$

the resulting classifier, given by (5.12), is called NB.

$$f_{nb} = \frac{p(C = 1)}{p(C = 0)} \prod_{i=1}^{n} \frac{p(x_i|C = 1)}{p(x_i|C = 0)} \tag{5.12}$$

In the NB learner there is no explicit search through the space of possible hypothesis. Instead, hypothesis are formulated counting the frequency of various training data combinations [41].

5.3.2 Logistic Regression

Regression models are an important component in any data analysis concerned in describing the relationship between a response and one or more explanatory variables, being linear regression the most common one [27]. Logistic Regression (LR), that unlike linear regression assumes a binary result, has been increasingly used in a wide variety of applications [3, 10].

The way LR works is equivalent to a single-output neural network with a logistic activation function trained under log loss. Using the previously introduced notation (subsection 5.3.1), and if we abbreviate $p(C = 1|E$ by p, we can describe the logistic regression model through equation 5.13.

$$\log\left(\frac{p}{1-p}\right) = \beta_0 + \beta_1 x_1 + \beta_2 x_2 + ... + \beta_n x_n \tag{5.13}$$

Where the fraction $p/(1-p)$ is called *the odds* that $C = 1$. The odds are, then, the ratio between the probability that $C = 1$ and the complementary $C = 0$. The β_i value is the weight that relates an independent variable x_i with the odds and, consecutively, with the probability that $C = 1$.

5.3.3 k-Nearest Neighbours

The k-Nearest Neighbours (kNN) is the simplest instance-based method, as it assumes all instances to be points in a n-dimensional space [41].

The *nearest neighbours* of an instance are defined based on euclidean distance (5.14) that relies on the n features $(x_1, x_2, ..., x_n)$ of each example E.

$$d(E_i, E_j) \equiv \sqrt{\sum_{r=1}^{n} (x_r(E_i) - x_r(E_j))^2} \tag{5.14}$$

After that, we account the classes from the k neighbours coming nearest to the actual example to decide how to classify it.

5.3.4 Support Vector Machines

The Support Vector Machine (SVM) is a promising method on learning separating functions for pattern recognition problems [33].

It uses a linear hyperplane for class separation, casting the problem as a "constrained nonlinear optimization problem". When linear separation is not possible in the original space SVM increases the space dimensionality by nonlinear mappings, after which finding the best separating hyperplane (the maximal margin hyperplane) (figure 5.11) is relatively trivial [33, 64].

Let us consider the binary classification problem with a training set $x_i,\ i = 1, ..., n$, assigned to one of two classes ω_1 and ω_2 with corresponding labels $y_i = \pm 1$, and denote the linear discriminant function (5.15) with decision rule (5.16).

$$g(x) = w^T x + w_0 \tag{5.15}$$

$$w^T x + w_0 \begin{cases} > & 0 \\ < & 0 \end{cases} \Rightarrow x \in \begin{cases} \omega_1 & \text{with corresponding number value } y_i = +1 \\ \omega_2 & \text{with corresponding number value } y_i = -1 \end{cases} \tag{5.16}$$

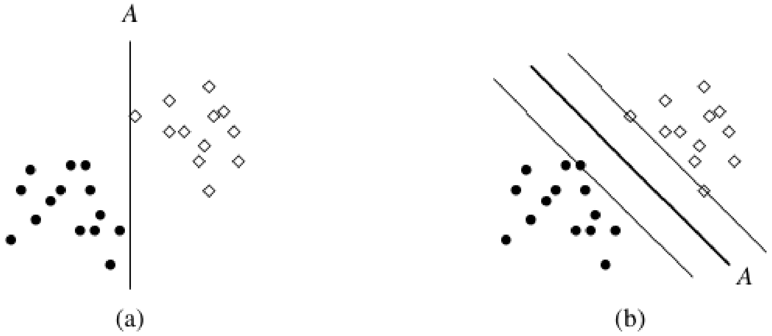

Figure 5.11: Two linear separable sets of data with separating hyperplane. The one on the right (thick line) leaves the closest points a maximum distance. The thin lines are the margin [64].

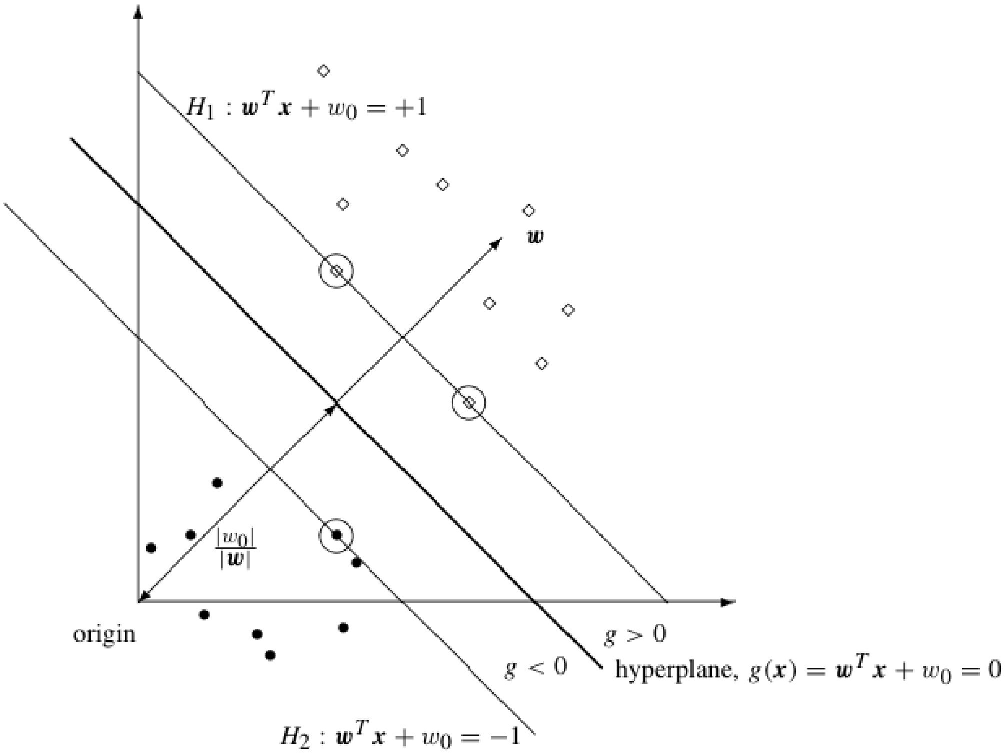

Figure 5.12: H_1 and H_2 are the canonical hyperplanes. The margin is the perpendicular distance between the separating hyperplane ($g(x) = 0$) and a hyperplane through the closest points (marked by a ring around the data points. [64].

Thus, all points are correctly classified if

$$y_i(w^T x_i + w_0) > 0 \text{ for all } i \tag{5.17}$$

Figure 5.11 shows two sets of points separated by hyperplane A. Being clear the existence of more than one possible hyperplane, the one that maximizes the separating margin is then given by the *maximal margin classifier*. Adding this margin, we have (5.18).

$$y_i(w^T x_i + w_0) \geq b \tag{5.18}$$

Assuming $b = 1$ to define the *canonical hyperplanes*, $H_1 : w^T x_i + w_0 \geq +1$ for $y_i = +1$ and $H_2 : w^T x_i + w_0 \leq -1$ for $y_i = -1$, we have the result depicted in figure 5.12. The points lying on canonical hyperplanes are called *Support Vectors* (circled on figure 5.12).

5.3.5 CN2

CN2 is a rule induction algorithm, designed for both efficiency and simplicity, with the ability to classify new examples accurately even in the presence of noise [13].

The CN2 generated rules are arranged as a set of *if-then* instructions known as decision list. The search for this list is terminated by an heuristic function based on a data noise estimation. This decision tree containing one rule per node is built through the proceeding depicted in algorithm 1. The auxiliary algorithm for finding the best complex is illustrated in algorithm 2. As for the used terminology is as explained through algorithm 3.

Algorithm 1 Procedure returning the rule list for the CN2 algorithm. [13].

```
let RULE_LIST be the empty list;
repeat
    let BEST_CPX be Find.Best.Complex(E);
    if BEST_CPX is not nill then
        Let E' be the examples covered by BEST.CPX;
        Remove from E the examples E' covered by BEST_CPX;
        Let C be the most common class of examples in E';
        Add the rule 'if BEST_CPX then class=C' to the end of RULE_LIST,
until BEST_CPX is nil or E is empty.
return RULE_LIST.
```

Algorithm 2 Procedure to find the best complex on the CN2 algorithm. [13].

```
let the set STAR contain only the empty complex;
let BEST_CPX be nil;
let SELECTORS be the set of all possible selectors;
while STAR is not empty,
    specialize all complexes in STAR as follows:
    let NEWSTAR be the set $\{x \wedge y \in$ STAR, $y \in$ SELECTORS $\}$;
    Remove all complexes in NEWSTAR that are either in STAR (i.e., the
        unspecified ones) or are null (e.g. big = y $\wedge$ big = n)
    for every complex $C_i$ in NEWSTAR:
        if $C_i$is statistically significant when tested on E and better than
            BEST_CPX according to user-defined criteria when tested on E,
        then replace the current value of BEST_CPX by $C_i$;
    repeat remove worst complexes from NEWSTAR
        until size of NEWSTAR is $\leq$ user-defined maximum;
    let STAR be NEWSTAR;
return BEST_CPX.
```

Algorithm 3 Rule terminology illustration for CN2 algorithm. The area surrounded by square brackets represents a *Complex*, and the italic text is a *Selector*. The entire set of rules is called *Cover* and the set of alternative complexes is referred as *Star*.

```
if [ HD $> 0.35 \wedge$ $ratioImag > 0.7$]
then Impostor
else Genuine
```

5.4 Results and Discussion

Our first tests were conducted in an UBIRIS.v2 database sub-set, containing images captured with the subject looking at camera direction. That allowed us, at an initial state, to avoid eventual problems associated with more complex noise factors (like gazed look), which would inevitably require implicit corrections.

In this kind of data, the used pattern recognition methods produced the results presented at tables 5.2 and 5.3, for the Classification Accuracy (CA) and ROC's Area Under Curve (AUC) respectively. Besides the classification algorithm, we made variations on the number of features supplied to the LFDA, *i.e.* the dimensionality the algorithm would operate on.

Table 5.2: Classification Accuracy variation for UBIRIS.v2 frontal images accordingly to classification method and number of features.

♯ Feat	NB	LR	kNN	SVM	CN2
1	0.9579	0.9582	0.9530	0.9577	0.9566
5	0.6781	0.9581	0.9519	0.9579	0.9516
10	0.9052	0.9579	0.9411	0.9568	0.9507
15	0.8435	0.9582	0.9475	0.9571	0.9530
25	0.8912	0.9587	0.9504	0.9564	0.9529
50	0.9539	0.9585	0.9464	0.9575	0.9575
75	0.9534	0.9589	0.9475	0.9573	0.9531
100	0.9536	0.9587	0.9504	0.9570	0.9525
125	0.9527	0.9590	0.9484	0.9586	0.9532

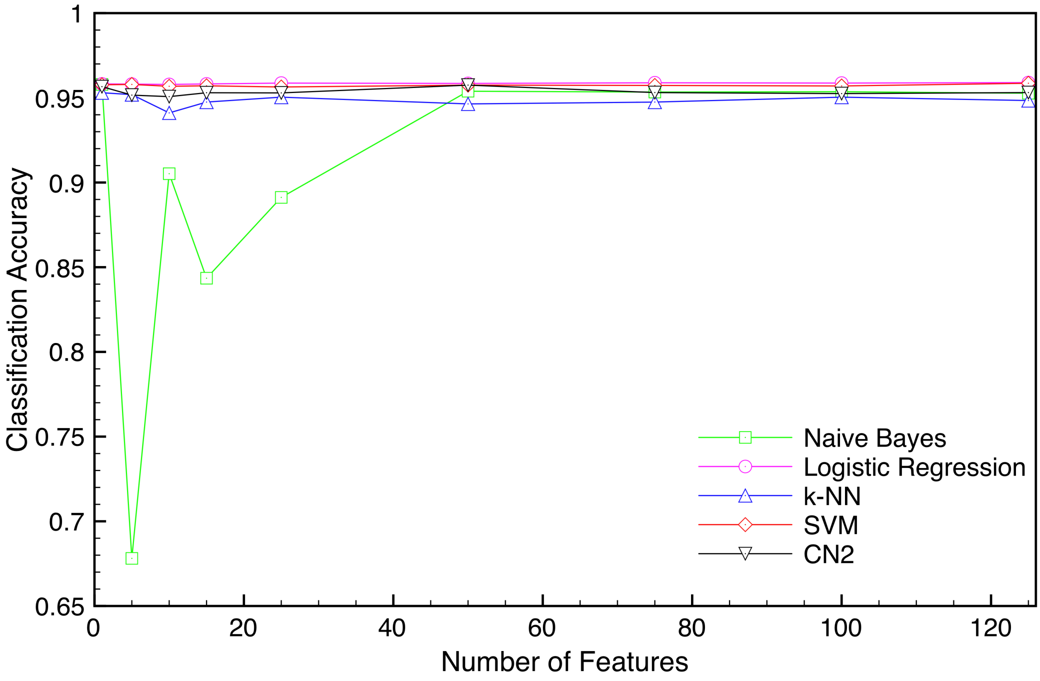

Figure 5.13: Classification Accuracy variation for UBIRIS.v2 frontal images accordingly to classification method and number of features.

For the CA, which is the proportion of correctly classified examples, and apart from the Naive Bayes algorithm, values are relatively stable at about 0.95. This happens because of classes' strong unbalancing: for the over 15000 produced comparisons (which are our samples), over 14000 belong to inter-class and less than one thousand to the intra-class distribution. This could led, for example, to high CA values in a classification method which associates all entries to "impostor" comparisons, although it as no ability at all to establish a distinction between them and intra-class ones. Figure 5.13 illustrates more clearly the CA results from table 5.2.

Following that line of reasoning, ROCs' AUC allow us to better analyse the true ability to perform correct classification of both categories. The ROC reflects the variability of both the FAR and true accept rate according to each other. That way, and facing figure 5.14 where AUC variations are depicted for the used pattern recognition algorithms as a function of the number of used features, we can draw some interesting conclusions.

Table 5.3: Area under ROC curve variation for UBIRIS.v2 frontal images accordingly to classification method and number of features.

♯ Feat	NB	LR	kNN	SVM	CN2
1	0.8499	0.8499	0.7529	0.6095	0.8224
5	0.7674	0.8503	0.7417	0.7307	0.7671
10	0.6943	0.8514	0.7291	0.7446	0.6544
15	0.6382	0.8507	0.7153	0.7326	0.6650
25	0.7089	0.8528	0.6991	0.7263	0.6286
50	0.8127	0.8564	0.6359	0.7304	0.6627
75	0.8113	0.8548	0.6494	0.7652	0.6410
100	0.8312	0.8553	0.6313	0.8025	0.6500
125	0.8345	0.8562	0.6239	0.8193	0.6485

To start, being the Hamming Distance used by Daugman the first and best feature, it is clear its ability to produce alone on the majority of methods quite good results. Only the SVM is unable of satisfiable operation on this attribute alone, and the kNN also presents some minor difficulties. On most of the remaining methods, when more features are added, we can see a decrease on class separability. The NB and SVM classifiers can recover from such decay when at least 50 features are considered and, although SVM can with the best 125 features overcome all CA results for one feature alone, the outcome difference is minimal.

In this not so optimistic scenario, there is a method that stands out - Logistic

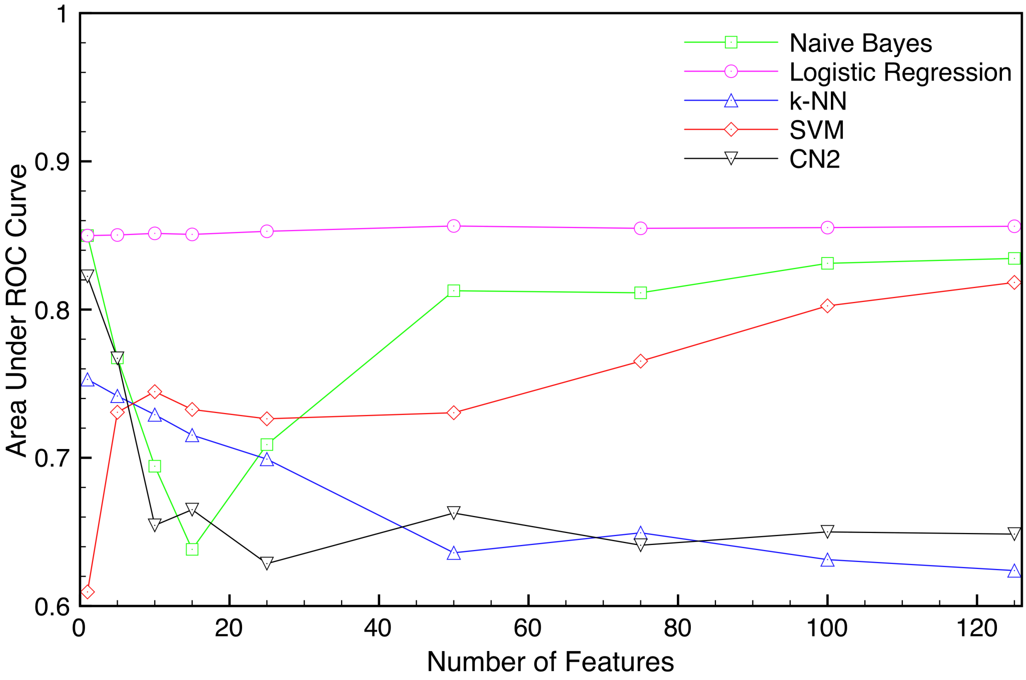

Figure 5.14: Area under ROC curve variation for UBIRIS.v2 frontal images accordingly to classification method and number of features.

Regression. This algorithm is able to present the best results when using the HD alone, and they became even better along with the addition of more features. Facing this, was more or less natural when the best results were obtained with LR for the best 125 features (accordingly to mRMR), restructured to 15 dimensions using the LFDA.

Despite the tendency to obtain better results along with the inclusion of more and more features, the heavy implementation and computational requirements of LFDA algorithm make impracticable carrying on tests with larger feature sets without reducing the number of samples. We then choose to experiment with a maximum of 125 features, and keep an higher representativeness of the working data. Also, using such high number of features would defeat the purpose of the selection arranged by mRMR application.

When LR stability was settled, comparative trials were carried out in three different setups. Using the same iris database, the method was applied to both frontally and close captured images (clearly a simpler subset) and another set containing iris imaged in all conditions with no particular restriction. Our approach was also tested once again against the first version of UBIRIS. Results of such tests are presented at tables 5.4 and 5.5.

Table 5.4: Logistic Regression results for different data-set configurations.

	HD		125 Feat	
	AUC	CA	AUC	CA
UBIRIS.v2	0.7315	0.9574	0.7598	0.9589
UBIRIS.v2 Frontal	0.8499	0.9582	0.8562	0.9590
UBIRIS.v2 Frontal Close	0.8740	0.9632	0.8897	0.9643
UBIRIS	0.9865	0.9868	0.9932	0.9897

Attending once again to the information given by AUC assessment when using the HD information alone, and as expected, this measurement had an inverse variation with data-base “difficulty”. The worst result was obtained for UBIRIS.v2, increased for frontal images only, and eventually even more for irises captured between 4 and 6 meters. For the UBIRIS this value was even closer to optimal performances.

When adding the information held on the best 125 extracted features, we observed improved results for all the setups, occurring the most significant ones when using images from all UBIRIS.v2. Once again, CA values are relatively high. Although this measurement also increases with our approach, the addition is residual because of the before stated reasons.

Table 5.5 allows perhaps a better understanding of the improvements introduced with our method.

In these matrices, representing proportions of true for different data-set setups, we can observe that decreases on the FRR are achieved without compromising, at least significantly, the FAR. This outcome varies from some shy 1.7 percentile points for frontal UBIRIS.v2 images to the 6.8% on the first version of UBIRIS. The FAR and FRR represent the relations between the well succeeded recognitions and the total of “impostor” and “authentic” ones respectively.

Is also interesting to observe that for the UBIRIS.v2 data-set, containing 500 images from which only one third are frontal captured ones, there was an increment of 4.9% on the true positive rate. We must remember that the trials from which initial considerations were extrapolated, leading us to carry on with Logistic Regression and 125 features, only contained frontally captured irises, and we are dealing with images captured within the VW.

Table 5.5: Confusion matrices representing proportions of true for different data-set configurations. Percentile values.

		Predicted			
		HD		125 Feat	
	Real	0	1	0	1
UBIRIS.v2	0	100.0	0.0	100.0	0.0
	1	99.1	0.9	95.0	5.0
UBIRIS.v2 Frontal	0	99.7	0.3	99.7	0.3
	1	85.8	14.2	84.1	15.9
UBIRIS.v2 Frontal Close	0	99.7	0.3	99.6	0.4
	1	79.7	20.3	74.4	25.6
UBIRIS	0	99.8	0.2	99.8	0.2
	1	26.2	73.8	19.4	80.6

All the presented values were cross-validated with ten folds.

Chapter 6

Conclusion

This thesis main objective was to minimize the trade-off between the quality of acquired images and the final error rates on the iris recognition process, when carried out without subject cooperation and within the VW.

Along this last year several contributions presented by many authors were studied, related not only to the recognition process itself but also other aspects that could help to the achievement of better results. Knowledge was also acquired within the pattern recognition area and associated paradigms, when applying this kind of methodology to analyse and classify the features obtained during the process.

For the interpolation, although not usually mentioned, when used in the translation of the segmented iris data in the Cartesian coordinate system into the pseudo-polar normalized coordinate system, can impact the final performance of the recognition process. Using Daugman's recognition method and two data-sets with different levels of noise to evaluate the variations in the recognition error rates as function of three image interpolation variants (no-interpolation, bilinear and bicubic), we concluded that the use of these techniques does not constitute any significant advantage in iris images with low levels of noise and tends to contribute to a slightly decrease in the recognition error rates of highly noisy iris images.

As for the non-cooperative iris recognition environments, where the ability to deal with highly noisy and heterogeneous data is required, we can affirm the application of data-mining and pattern recognition methods to this problem (which is traditionally analysed in a more rigid manner) to be, starting from the new features extracted through spatial and frequency domains analysis to the matching results between two subjects, advantageous. This approach, analysing not only the individual features of each subject, but the result of a modified implementation of the matching proposed by Daugman instead, produced outcomes in all the stressed databases. Having in mind that those modifications contemplate the usage of a reduced iris portion considered noise-free, and knowing that for UBIRIS.v2 that is an unrealistic thinking, its relatively solid to take as a fact that as further work the modification of this approach to include noise information can lead to even better results. The same inference can be extended to the execution of noise attenuating methods, specially in off-angle and rotated image correction, which was not carried.

We must also consider that images were matched against each other. On a fully deployed system, captured images are compared against a database record which contains almost none or no noise at all.

6.1 Further Work

Although satisfactory, this work is not a breakthrough in this area. It started with the adaptation of a NIR method to the VW spectrum, disregarding eventual useful information this new scenario could bring. Thus, further work is needed and some way-points can already be defined seeking for performance improvement.

When working in the VW spectrum, along with the well known disadvantages, comes new information which is currently not being used: iris colorimetric data. Carrying color information to advanced stages of the recognition process, instead of converting the image to gray-scale, can intuitively help telling subjects apart. At an initial stage, we can simply apply a gray-scale conversion procedure with better color separability. This kind of conversion is already deployed in another vision related areas.

Another improvement, as already mentioned, was to perform corrections or enhancements lowering noise impact. Ideally, we should know not only which areas were occluded by noise, but also be able to tell apart different noise types so that different procedures could be carried to attenuate each one of them. Possessing all this rich information, we could then use not only the comfortable “noise-free” area but the hole iris data in much a better way.

Combining these improvements with the presented work, we are confident that non-cooperative noisy iris recognition can become less of an utopia and more of a fully capable, covertly deploy-able system.

Appendix A

Full mRMR Results

Order	Feature	Score	Order	Feature	Score
1	Hamming Distance	0.351	26	FFT Std $(641, 1)$	-0.833
2	Haar Max (8×8)	-0.015	27	Haar Hist (bin 22)	-0.861
3	Ratio Imag $(i = 9)$	-0.065	28	FFT Min $(513, 17)$	-0.874
4	Haar Max (10×10)	-0.057	29	FFT Std $(1, 9)$	-0.894
5	Haar Max (12×12)	-0.157	30	FFT Min $(769, 1)$	-0.909
6	Ratio Real $(i = 9)$	-0.160	31	Haar Hist (bin 5)	-0.932
7	Haar Hist (bin 1)	-0.217	32	FFT Ent $(769, 9)$	-0.947
8	Haar Hist (bin 25)	-0.294	33	FFT Std $(129, 17)$	-0.966
9	Ratio Imag $(i = 8)$	-0.336	34	FFT Min $(769, 25)$	-0.977
10	Haar Max (14×14)	-0.347	35	FFT Ent $(257, 17)$	-0.985
11	Ratio Real $(i = 1)$	-0.403	36	FFT Std $(513, 25)$	-0.995
12	Ratio Real $(i = 8)$	-0.441	37	FFT Min $(385, 1)$	-1.008
13	Ratio Imag $(i = 1)$	-0.479	38	FFT Std $(129, 1)$	-1.016
14	Haar Max (16×16)	-0.522	39	Haar Hist (bin 21)	-1.024
15	FFT Std $(769, 9)$	-0.570	40	FFT Std $(513, 9)$	-1.036
16	Ratio Real $(i = 6)$	-0.601	41	Ratio Real $(i = 5)$	-1.045
17	Haar Hist (bin 23)	-0.632	42	FFT Std $(385, 25)$	-1.054
18	Haar Hist (bin 2)	-0.659	43	FFT Ent $(1, 9)$	-1.063
19	FFT Std $(769, 25)$	-0.688	44	FFT Min $(769, 9)$	-1.071
20	FFT Std $(385, 1)$	-0.714	45	FFT Min $(257, 25)$	-1.077
21	FFT Min $(129, 1)$	-0.740	46	FFT Std $(897, 9)$	-1.087
22	Haar Hist (bin 24)	-0.752	47	Ratio Real $(i = 7)$	-1.093
23	Haar Max (18×18)	-0.766	48	Ratio Imag $(i = 6)$	-1.100
24	FFT Min $(129, 17)$	-0.796	49	FFT Min $(257, 1)$	-1.109
25	Ratio Imag $(i = 7)$	-0.813	50	Haar Hist (bin 8)	-1.115

Order	Feature	Score	Order	Feature	Score
51	FFT Std $(513, 1)$	-1.123	91	Haar Hist (bin 17)	-1.343
52	FFT Ent $(513, 17)$	-1.128	92	FFT Min $(385, 17)$	-1.355
53	FFT Std $(385, 9)$	-1.134	93	FFT Ent $(129, 1)$	-1.362
54	Haar Max (20×20)	-1.140	94	FFT Min $(129, 9)$	-1.364
55	FFT Ent $(129, 17)$	-1.145	95	FFT Std $(385, 17)$	-1.367
56	Ratio Real $(i = 2)$	-1.148	96	FFT Ent $(897, 25)$	-1.372
57	FFT Min $(897, 25)$	-1.159	97	Haar Max (30×30)	-1.375
58	FFT Min $(385, 9)$	-1.163	98	FFT Min $(641, 9)$	-1.380
59	FFT Std $(257, 25)$	-1.168	99	Haar Hist (bin 12)	-1.386
60	Haar Hist (bin 6)	-1.171	100	FFT Ent $(513, 9)$	-1.391
61	FFT Min $(513, 9)$	-1.179	101	FFT Std $(257, 1)$	-1.397
62	Ratio Imag $(i = 5)$	-1.188	102	FFT Ent $(1, 1)$	-1.400
63	FFT Std $(897, 17)$	-1.194	103	FFT Std $(897, 1)$	-1.403
64	FFT Std $(257, 17)$	-1.207	104	Haar Hist (bin 3)	-1.406
65	Haar Hist (bin 7)	-1.211	105	FFT Min $(129, 25)$	-1.414
66	FFT Min $(385, 25)$	-1.218	106	Haar Hist (bin 15)	-1.416
67	FFT Min $(513, 25)$	-1.225	107	FFT Ent $(257, 1)$	-1.424
68	Haar Max (32×32)	-1.230	108	FFT Std $(641, 17)$	-1.429
69	FFT Min $(1, 25)$	-1.237	109	FFT Min $(897, 17)$	-1.431
70	FFT Min $(641, 25)$	-1.246	110	FFT Ent $(1, 17)$	-1.435
71	FFT Min $(641, 1)$	-1.252	111	FFT Min $(641, 17)$	-1.439
72	FFT Ent $(769, 25)$	-1.255	112	FFT Min $(897, 9)$	-1.442
73	Haar Hist (bin 4)	-1.261	113	FFT Min $(897, 1)$	-1.444
74	Haar Hist (bin 9)	-1.267	114	Haar Hist (bin 10)	-1.451
75	FFT Std $(257, 9)$	-1.273	115	FFT Std $(641, 9)$	-1.454
76	FFT Min $(1, 9)$	-1.277	116	FFT Ent $(257, 25)$	-1.462
77	FFT Min $(1, 1)$	-1.281	117	FFT Std $(1, 17)$	-1.465
78	Ratio Imag $(i = 2)$	-1.283	118	FFT Ent $(1, 25)$	-1.471
79	FFT Min $(1, 17)$	-1.287	119	FFT Ent $(641, 25)$	-1.473
80	Haar Hist (bin 20)	-1.290	120	FFT Ent $(513, 25)$	-1.476
81	FFT Max $(1, 17)$	-1.298	121	Haar Hist (bin 19)	-1.479
82	FFT Ent $(385, 1)$	-1.303	122	FFT Ent $(129, 9)$	-1.484
83	FFT Min $(513, 1)$	-1.307	123	Haar Hist $(bin14)$	-1.492
84	Haar Hist (bin 7)	-1.311	124	FFT Ent $(385, 25)$	-1.494
85	FFT Min $(257, 17)$	-1.316	125	FFT Std $(769, 17)$	-1.497
86	FFT Std $(641, 25)$	-1.319	126	FFT Min $(769, 17)$	-1.504
87	FFT Ent $(769, 1)$	-1.325	127	FFT Max $(513, 9)$	-1.510
88	FFT Ent $(641, 9)$	-1.330	128	FFT Max $(897, 17)$	-1.514
89	FFT Std $(513, 17)$	-1.334	129	FFT Std $(129, 9)$	-1.516
90	FFT Ent $(385, 9)$	-1.339	130	FFT Ent $(769, 17)$	-1.520

Order	Feature	Score	Order	Feature	Score
131	FFT Max $(385, 17)$	-1.530	171	Ratio Imag $(i = 4)$	-1.715
132	FFT Std $(129, 25)$	-1.533	172	FFT Mean $(513, 25)$	-1.723
133	FFT Ent $(897, 1)$	-1.535	173	FFT Max $(769, 17)$	-1.726
134	Haar Max (28×28)	-1.538	174	FFT Mean $(879, 9)$	-1.729
135	FFT Std $(897, 25)$	-1.541	175	FFT Max $(641, 9)$	-1.735
136	Haar Hist (bin 16)	-1.546	176	FFT Mean $(385, 9)$	-1.738
137	FFT Ent $(513, 1)$	-1.549	177	FFT Max $(769, 25)$	-1.743
138	Haar Max (26×26)	-1.554	178	FFT Mean $(257, 25)$	-1.752
139	FFT Ent $(897, 17)$	-1.564	179	FFT Max $(129, 1)$	-1.757
140	Haar Hist (bin 13)	-1.567	180	FFT Max $(897, 1)$	-1.761
141	FFT Ent $(257, 9)$	-1.569	181	FFT Max $(385, 25)$	-1.764
142	FFT Ent $(641, 1)$	-1.574	182	FFT Mean $(641, 9)$	-1.767
143	Haar Hist (bin 11)	-1.575	183	FFT Mean $(385, 25)$	-1.771
144	FFT Std $(1, 1)$	-1.584	184	Ratio Imag $(i = 3)$	-1.774
145	FFT Max $(385, 9)$	-1.587	185	FFT Mean $(257, 1)$	-1.779
146	FFT Max $(1, 9)$	-1.601	186	Ratio Real $(i = 3)$	-1.783
147	FFT Ent $(129, 25)$	-1.603	187	FFT Mean $(257, 17)$	-1.785
148	FFT Min $(257, 9)$	-1.607	188	FFT Max $(641, 1)$	-1.788
149	FFT Mean $(385, 17)$	-1.614	189	FFT Mean $(1, 17)$	-1.793
150	FFT Ent $(897, 9)$	-1.616	190	FFT Max $(129, 9)$	-1.798
151	FFT Max $(275, 1)$	-1.621	191	FFT Mean $(897, 1)$	-1.800
152	FFT Std $(769, 1)$	-1.623	192	FFT Max $(897, 25)$	-1.803
153	FFT Ent $(641, 17)$	-1.629	193	FFT Mean $(513, 17)$	-1.808
154	Haat Max (22×22)	-1.631	194	FFT Max $(1, 25)$	-1.818
155	FFT Mean $(897, 17)$	-1.636	195	FFT Max $(257, 9)$	-1.821
156	FFT Max $(897, 9)$	-1.640	196	FFT Max $(513, 17)$	-1.828
157	FFT Max $(1, 1)$	-1.645	197	FFT Max $(129, 17)$	-1.834
158	Haar Max (24×24)	-1.648	198	FFT Mean $(641, 25)$	-1.837
159	FFT Mean $(1, 9)$	-1.655	199	FFT Max $(513, 25)$	-1.846
160	FFT Mean $(513, 1)$	-1.660	200	FFT Max $(385, 1)$	-1.850
161	FFT Std $(1, 25)$	-1.669	201	FFT Max $(129, 25)$	-1.852
162	FFT Mean $(1, 25)$	-1.675	202	FFT Max $(257, 17)$	-1.859
163	FFT Max $(641, 25)$	-1.679	203	FFT Mean $(769, 25)$	-1.864
164	FFT Max $(257, 25)$	-1.682	204	FFT Max $(769, 1)$	-1.871
165	FFT Mean $(385, 1)$	-1.686	205	FFT Mean $(1, 1)$	-1.880
166	FFT Mean $(513, 9)$	-1.692	206	FFT Mean $(129, 1)$	-1.885
167	FFT Ent $(385, 17)$	-1.695	207	FFT Mean $(257, 9)$	-1.888
168	FFT Mean $(641, 1)$	-1.699	208	FFT Mean $(769, 17)$	-1.898
169	Ratio Real $(i = 4)$	-1.701	209	FFT Mean $(897, 25)$	-1.903
170	FFT Max $(641, 17)$	-1.708	210	FFT Max $(513, 1)$	-1.906

Order	Feature	Score	Order	Feature	Score
211	FFT Mean $(129, 9)$	-1.914	215	FFT Mean $(129, 25)$	-1.946
212	FFT Mean $(641, 17)$	-1.922	216	FFT Mean $(129, 17)$	-1.979
213	FFT Max $(769, 9)$	-1.925	217	FFT Mean $(769, 9)$	-2.007
214	FFT Mean $(769, 1)$	-1.934			

Feature description:

- Hamming Distance: Self-explanatory (equation 2.9);
- Haar Max $(i \times i)$: Global maximum for matching result convolution with a $i \times i$ Haar filter;
- Haar Hist (bin i): Value at the i^{th} bin of Haar convolution histogram;
- FFT {Ent|Mean|Min|Max|Std} (x,y): FFT entropy (Ent), mean (Mean), minimum (Min), maximum (Max) or standard deviation (Std) for the window starting at coordinates (x, y);
- Ratio {Real|Imag} $(i = k)$: Central shape density, for the FFT real or imaginary part, with a threshold T_k (equation 5.1b).

Appendix B

On the Role of Interpolation in the Normalization of Non-Ideal Visible Wavelength Iris Images

On the Role of Interpolation in the Normalization of Non-Ideal Visible Wavelength Iris Images

Gil Santos and Hugo Proença
Dept. of Computer Science - IT - Networks and Multimedia Group
Universidade da Beira Interior, Covilhã, Portugal
Email: m1214@ubi.pt, hugomcp@di.ubi.pt

Abstract—**The growth in practical applications for iris biometrics has been accompanied by relevant developments in the underlying algorithms and techniques. Along with the research focused on near-infrared (NIR) cooperatively captured images, efforts are being made to minimize the trade-off between the quality of the captured data and the recognition accuracy on less constrained environments, where images are obtained at the visible wavelength, at increased distances, over simplified protocols and adverse lightning. This paper addresses the effect of the interpolation method, used in the iris normalization stage, in the overall recognition error rates. This effect is stressed for systems operating under less constrained image acquisition setups and protocols, due to higher variations in the amounts of captured data. Our experiments led us to conclude that the utility of the image interpolating methods is directly corresponding to the levels of noise that images contain.**

I. INTRODUCTION

One of the most active research areas in biometry seeks to minimize the constraints associated to the recognition process. The use of the iris as main biometric trait is emerging as one of the most recommended, due to the possibility of contactless data acquisition and to its circular and planar shape that makes easy the detection, segmentation and compensation for off-angle capturing. This area - often called *non-cooperative iris recognition* - receives growing attention from the research community (e.g., [1]–[6], [21]).

Independently of the type of used images (NIR or visible wavelength) and of the constraints associated to the acquisition setup, the large majority of the iris recognition methods perform the normalization of the segmented data into a dimensionless pseudo-polar coordinate system through a process known as the "Daugman rubber sheet" (e.g., [7]–[9]). This transforms the segmented iris data into a rectangular block of fixed size and compensates for varying image capturing distances and pupils' sizes. Due to the different amount of data in the segmented ring and in the normalized block, the use of some interpolation method is unavoidable and constitutes the scope of the work described in this paper. However, the role of the normalization stage is stressed for non-cooperative iris recognition purposes, due to significantly higher variations in the amounts of captured data dictated by the higher range of image capturing distances, different perspectives and heterogeneous lighting conditions that determine the size of the pupil.

In this paper we show how the interpolation method used in the normalization process affects the overall performance of the recognition system. We used our implementation of the Daugman's recognition method [7] and varied the type of interpolation method used in the normalization process, having observed the variations in the recognition error rates over two well known visible wavelength iris image datasets [10], [11].

The remaining of this paper has the following structure: Section II overviews the iris recognition process, namely the less constrained iris acquisition setup and the Daugman's approach. Section III briefly overviews the used variants of image interpolation methods, describes the used datasets and discusses the obtained results. Finally, Section IV states the conclusions.

II. IRIS RECOGNITION

The large majority of the published iris recognition methods follow the statistical pattern recognition paradigm, and share the structure given in figure 1 The process starts with the segmentation of the iris ring in the close-up eye image. Further, data is transformed into a double dimensionless polar coordinate system, through the above referred *Daugman's Rubber Sheet* process. Regarding the feature extraction stage, existing approaches can be roughly divided into three variants: phase-based [12], zero-crossing [13] and texture-analysis methods [14]. Dauman [12] used multi-scale quadrature wavelets to extract texture phase-based information and obtain an iris signature with 2048 binary components. Boles and Boashash [13] computed the zero-crossing representation of a 1D wavelet at different resolutions of concentric circles. Wildes [14] proposed the characterization of the iris texture through a Laplacian pyramid with four different levels. Finally, in the feature comparison stage, a numeric dissimilarity value is produced, which determines the subjects' identity. Here, it is usual to apply different distance metrics (Hamming [12],

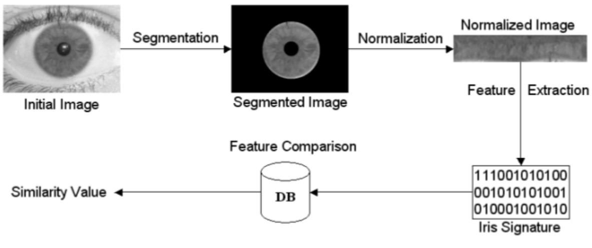

Fig. 1. Typical block diagram of the published iris recognition methods.

Euclidian [15] or weighted Euclidian [16]), or methods based on signal correlation [14].

The accuracy of the deployed iris recognition systems is remarkable, as reported by the study conduced by Daugman [17] and three other independent evaluations [18]–[20]. However, we stress that those error rates are conditioned to the acquisition of good quality images, captured in stop-and-stare interfaces, at close imaging distances. Also, failures on this acquisition setup cause significant increment of the recognition error rates.

A. *Less Constrained Image Acquisition*

In less constrained conditions, where a trade-off between data acquisition constrains and recognition accuracy is inevitable, the challenge is to maximally increase flexibility in three axes: subjects position and movements, imaging distances and lightning conditions. As before stated, this area receives growing interests from the research community and constituted the scope of several publications. The "Iris-on-the-move" project [2] is a major example of the engineering image acquisition required to make the recognition process less intrusive to subjects. *Honeywell Technologies* registered a patent [3] of a similar system capable of performing at-a-distance iris recognition. Previously, Fancourt et al. [4] showed that it is possible to acquire images at-a-distance of up to 10 meters with sufficient quality to support iris recognition and Narayanswamy and Silveira [5] increased the iris image depth-of-field through a simple framework composed by a camera with fixed focus, without a zoom lenses. Park and Kim [21] proposed an approach to fast at-a-distance acquisition of iris images and He *et al.* [6] studied the acquisition of in-focus images, as well analyzed the impact of different wavelengths in the recognition error rates. Although concluding that illumination inside the 700-900 nm optimally reveals the richness of the iris structure, they observed that irises with moderate levels of pigmentation could be imaged in the visible light with good quality.

B. *Daugman's Approach*

The Daugman's approach [7] to perform the iris biometric recognition is known to be the most widely acknowledged, with great acceptance over the scientific community. Apart from being the uniquely implemented in commercially deployed systems, it is the one that usually acts as comparison term for alternative proposals.

The structure of this method is as follows: it starts by the detection and segmentation of the iris, through the determination of its circular contours. Later, the normalization of the segmented region is made as described in subsection II-C. The next stage is iris feature extraction through the convolution of the normalized data with a bank of 2D Gabor Wavelets (1), followed by the quantization that gives a binary *iriscode*. This code is used in the matching stage, using the *Hamming Distance* (2) as comparison measure.

$$\begin{aligned} h_{\{Re,Im\}} = sgn_{\{Re,Im\}} \int_\rho \int_\phi I(\rho,\phi) e^{iw(\theta_0-\phi)}. \\ .e^{-(r_0-\rho)^2/\alpha^2} e^{-(\theta_0-\phi)^2/\beta^2} \rho d\rho d\phi \end{aligned} \tag{1}$$

$$HD = \frac{\|(codeA \otimes codeB) \cap maskA \cap maskB\|}{\|maskA \cap maskB\|} \tag{2}$$

The performance can be accessed by its decidability (3), that reflects the distance between the two distributions obtained for the comparisons between signatures extracted from the same (*intra-class*) and different persons (*inter-class*).

$$d' = \frac{|\mu_{inter} - \mu_{intra}|}{\sqrt{\frac{\sigma_{inter}^2 + \sigma_{intra}^2}{2}}} \tag{3}$$

Where μ_{inter} and μ_{intra} denote the means of the inter- and intra-class comparisons and σ_{inter} and σ_{intra} the respective standard deviations.

C. *Image Normalization*

As mentioned before, the normalization process aims to obtain invariance to size, position and pupil dilatation in the segmented iris region. This is accomplished by assigning each pixel to a pair of real coordinates (r,θ) over the polar coordinates system, which will be used in the later stages.

For this purpose, we will proceed with Daugman's rubber-sheet model [22], as originally proposed. (4) and (5) give a transformation similar to the depicted in figure 1.

$$I(x(r,\theta), y(r,\theta)) \rightarrow I(r,\theta) \tag{4}$$

$$\begin{aligned} x(r,\theta) &= (1-r)x_p(\theta) + rx_s(\theta) \\ y(r,\theta) &= (1-r)y_p(\theta) + ry_s(\theta) \end{aligned} \tag{5}$$

Where r and θ denote respectively the radius and the angle, $x(r,\theta)$ and $y(r,\theta)$ are defined as linear combinations of both the set of pupillary boundary points $(x_p(\theta), y_p(\theta))$ and the set of limbus boundary points along the outer perimeter of the iris $(x_s(\theta), y_s(\theta))$ bordering the sclera.

III. EXPERIMENTS

The use of the Daugman's recognition method should be justified. Although this method has been thought to operate over iris images acquired at NIR wavelengths, it has proven to perform well in different types of images, specially if the iris was accurately segmented and occlusions of the iris textures are detected and localized in the original and normalized data. The necessary parameters for the Gabor wavelets (1) were tuned for best performance on all different trials, being chosen those with maximal decidability (3). Regarding iris' location and segmentation, all images were manually and accurately segmented, being known the center and radius of the pupils and of the iris and detected the regions that occlude portions of the iris. Thus, we assume that segmentation inaccuracies and noisy regions do not corrupt the obtained results.

A. Image Interpolation Methods

On the translation between the cartesian and the pseudo-polar coordinate system we used three interpolation variants. The first - hereinafter called *no interpolation* - simply picks from the cartesian data the nearest neighbor pixel of $(x(r,\ \theta), y(r,\ \theta))$ (using L_2 norm). Also, we implemented two of the most well known interpolation variants: the bilinear and bicubic [23], which obtain the corresponding value according to its neighborhood, as below described. Other types of interpolation (as the bicubic splines) were not the focus of our analyzis, essentially because we believe that the obtained results will be close to those obtained.

1) Bilinear Interpolation: This is the simplest method to perform the two-dimensional approximation of missing values.

$$y(x_1, x_2) = (1-t)(1-u)y_0 + t(1-u)y_1 + tuy_2 + (1-t)uy_3 \tag{6}$$

To determine the value $y_{ij} = y(x_{1i}, x_{2j})$ at some point, (6) is used, considering four surrounding points $y_o, ..., y_3$, defined counterclockwise starting from the lower left that obey the relations stated in (7) with i and j according to (8) and t, u as described in (9).

$$\begin{aligned} y_0 &\equiv y_{ij} & y_1 &\equiv y_{(i+1)j} \\ y_2 &\equiv y_{(i+1)(j+1)} & y_3 &\equiv y_{i(j+1)} \end{aligned} \tag{7}$$

$$x_{1i} \le x_1 \le x_{1(i+1)} \qquad x_{2j} \le x_2 \le x_{2(j+1)} \tag{8}$$

$$\begin{aligned} t &\equiv (x_1 - x_{1i})/(x_{1(i+1)} - x_{1i}) \\ u &\equiv (x_2 - x_{2j})/(x_{2(j+1)} - x_{2j}) \end{aligned} \tag{9}$$

2) Bicubic Interpolation: This interpolation method gives an higher order of smoothness, at a cost of use a higher number of pixels in each operation. Interpolation for the function y, given the four derivatives y_1, y_2, y_{12}, is executed in two steps: determination of quantities $c_{ij}, i, j = 0, ..., 3$ combining a region of the image with the appropriate matrix, and then the following equations (10) with t, u given by (9).

$$\begin{aligned} y(x_1, x_2) &= \sum_{i=0}^{3}\sum_{j=0}^{3} c_{ij}t^i u^j \\ y_1(x_1, x_2) &= \sum_{i=0}^{3}\sum_{j=0}^{3} ic_{ij}t^{i-1}u^j(dt/dx_1) \\ y_2(x_1, x_2) &= \sum_{i=0}^{3}\sum_{j=0}^{3} jc_{ij}t^i u^{j-1}(du/dx_2) \\ y_{12}(x_1, x_2) &= \sum_{i=0}^{3}\sum_{j=0} ij^3 c_{ij}t^{i-1}u^{j-1} \end{aligned} \tag{10}$$

B. Datasets

In the experiments, two different datasets were used: Ubiris and Ubiris.v2. The higher range of image acquisition distances enables the capturing of irises with higher varying sizes and will make the results more visible. Also, our research concerns the feasibility of recognition in visible wavelength iris images, captured at-a-distance and on-the-move.

The Ubiris database [10] was created at the Soft Computing and Image Analysis Lab (*SOCIA Lab*) of the University of Beira Interior. It consists on a set of visible wavelength noisy iris images, captured at close-up distance with user cooperation. This dataset is intended for the development of robust iris recognition algorithms for biometric purposes and aims to *simulate* non-cooperative image acquisition, adding noise to the resultant images.

The Ubiris.v2 [11], also created at *SOCIA Lab*, contains images *actually* captured at-a-distance (between 4 and 8 meters) from moving subjects. Those images contain several regions of the iris rings occluded by reflections, as well significant iris obstructions due to eyelids and eyelashes.

Over 500 pictures (400×300 pixels) were used from each dataset on our experiments. In both cases, we selected a group of images that we believe to represent each dataset.

C. Results and Discussion

1) Cartesian Data Usage: Our first observation is that the interpolating methods used in the normalization process do impact over iris pixels usage. To illustrate this, figure 2 shows the number of times each pixel located within the ring of a segmented iris region is used in the translation into the normalized data. Here, brighter pixels denote those more frequently accessed. The higher smoothness of the image corresponding to the bicubic interpolation is evident, as well evident discontinuities in the pixels' usage can be observed in the left image, obtained when used the no interpolation variant.

Not surprisingly, we observed that the average probability of a pixel to be used in the normalization process remains stable (due to the fixed size of the normalized block). However, the standard deviation obtained for the corresponding distribution becomes significantly lower when interpolation methods are used. In other words, pixel selection during a normalization process became more balanced, directly corresponding to the complexity of the interpolation process, i.e., to the number of pixels involved in a single interpolating operation.

Figures 3 and 4 give histograms about the probability for the pixels usage in the normalization stages, respectively in the Ubiris and Ubiris.v2 data sets. The horizontal axis gives the probability beans and the vertical gives the number of pixels that fall in the corresponding bean.

Regarding the Ubiris dataset (highly normalized), it can be observed a considerable reduction in the amount of pixels that were never accessed during the normalization procedure (#pix-

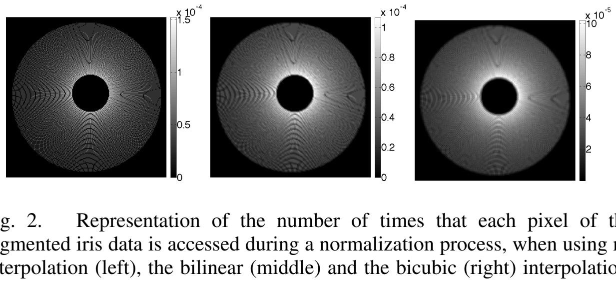

Fig. 2. Representation of the number of times that each pixel of the segmented iris data is accessed during a normalization process, when using no interpolation (left), the bilinear (middle) and the bicubic (right) interpolation.

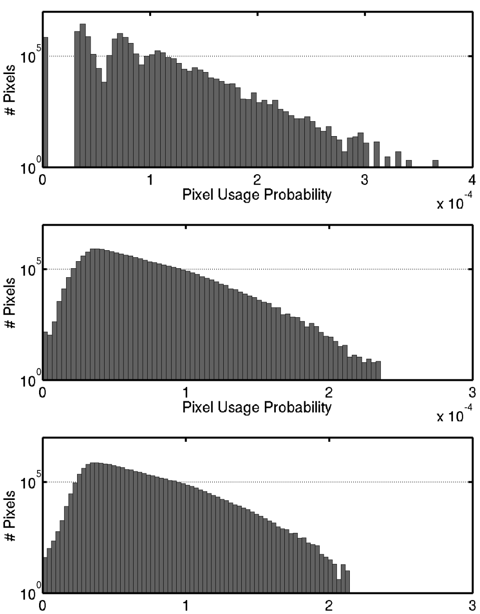

Fig. 3. Overall probability for the iris pixel usage respectively with no interpolation (top), bilinear (middle) and bicubic interpolation (bottom) in the Ubiris dataset.

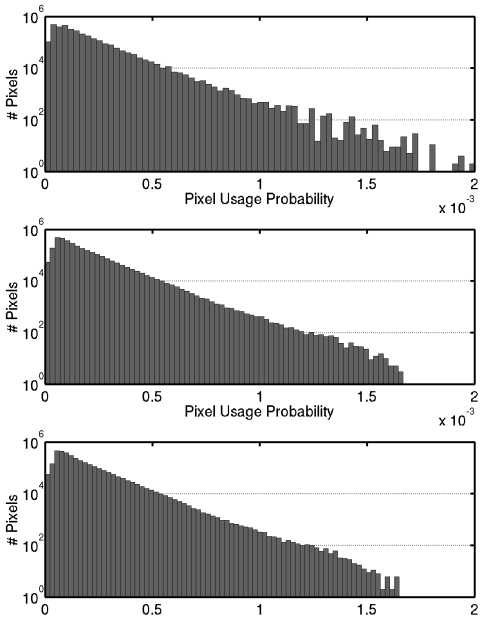

Fig. 4. Overall probability for the iris pixel usage respectively with no interpolation (top), bilinear (middle) and bicubic interpolation (bottom) in the Ubiris.v2 dataset.

els within the 0 probability bean), as well as an accentuation of the slope of the #Pixels value regarding the augment of the probability values.

The spread of the bar beans also suffers an decrement, from the no-interpolation to the bilinear and from this one to the bicubic variant. Using the bilinear interpolation, the probability for the pixel selection converged to a more evenly distributed iris data usage, where pixels are more likely to became part of the data used to extract the iriscode. Finally, when analyzing the bicubic interpolation, these changes are even more visible. The amplitude of the overall distribution was smaller and more homogeneous, as well as the resemblance between the probability for the pixel selection and a normal distribution.

Interestingly, the values obtained for the Ubiris.v2 database were more close to each other, which we explain by the higher irregularity of this data set. However, the above stated observations for the first version of the database fit to the results obtained for this second version, as can be seen essentially by the higher spread of the histogram's beans when no interpolation method was used.

2) Recognition Error Rates: Here, we give results about the variations of the recognition error rates, as function of the type of interpolating method used in the normalization process. We plot the receiver operating curves (ROC) obtained when using each of the three interpolating variants on the two experimented datasets. The first interesting observation is that the lowest error rates in the Ubiris data set were - clearly - obtained when no interpolation method was used (figure 5). Our interpretation is that less cartesian iris pixels are used in the normalized data, which minimizes the aliasing effects induced by the normalization process. Thus, in environments that propitiate the acquisition of less noisy images, the use of interpolating methods represents no-advantage, as showed by the difference between the results obtained when using no-interpolation and the interpolating methods.

Oppositely, for the Ubiris.v2 images the better results were obtained when using the two types of interpolating techniques (figure 6). As this dataset contains higher levels of noise, the normalization process tend to be best succeed if more iris pixels are used in each normalization step, smoothing the corruption that non-detected noisy data carries to the normalized image.

Finally, the previously described usage of the iris pixels of the cartesian coordinate system as function of the interpolation method is resumed in Table I, with corresponding confidence

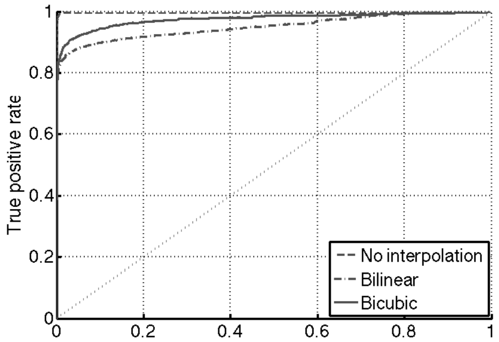

Fig. 5. ROC curve for different interpolation methods on Ubiris dataset.

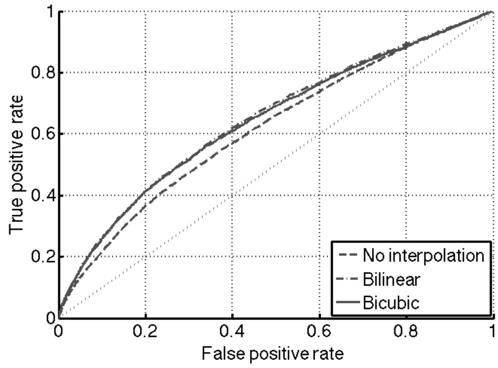

Fig. 6. ROC curve for different interpolation methods on Ubiris.v2 dataset.

intervals of 95%. Also, it is given the decidability (3) of the corresponding pattern recognition systems. That - again - confirms the previously stated conclusions: the use of image interpolation techniques on less noisy images seems not to represent any surplus in the final error rates. However, if images are highly noisy, interpolation techniques can slightly increase the recognition accuracy.

	Interpolation	Iris Usage	Decidability
Ubiris	None	$0.926 \pm 1.663 \times 10^{-4}$	4.390
	Bilinear	$0.999 \pm 2.294 \times 10^{-6}$	2.724
	Bicubic	$0.999 \pm 6.362 \times 10^{-7}$	2.779
Ubiris.v2	None	$0.967 \pm 1.957 \times 10^{-4}$	0.410
	Bilinear	$0.986 \pm 1.286 \times 10^{-4}$	0.519
	Bicubic	$0.988 \pm 1.209 \times 10^{-4}$	0.496

TABLE I
IRIS PIXEL USAGE AND DECIDABILITY ON DIFFERENT INTERPOLATION METHODS FOR UBIRIS AND UBIRIS.V2 DATASET.

IV. CONCLUSIONS

Although usually not mentioned, the interpolation technique used in the translation of the segmented iris data between coordinate systems can impact the final error rates of the recognition system. In this paper we used the Daugman's recognition method and two data sets with different levels of noise to evaluate the variations in the recognition error rates, as function of three image interpolating variants: nearest neighbor (no-interpolation), bilinear and bicubic.

We concluded that the use of interpolation techniques does not constitute any significant advantage in iris images with low levels of noise and tend to contribute to a slightly decrease in the recognition error rates of highly noisy iris images. Thus, further research is required to access the utility of these interpolating techniques in the increase of the recognition robustness, on non-cooperative iris recognition environments, where the ability to deal with highly noisy and heterogeneous iris data is required.

ACKNOWLEDGMENT

We acknowledge the financial support given by "FCT-Fundação para a Ciência e Tecnologia" and "FEDER" in the scope of the PTDC/EIA/69106/2006 research project "BIOREC: Non-Cooperative Biometric Recognition".

REFERENCES

[1] H. Proença, "On the feasibility on the visible wavelength, at-a-distance and on-the-move iris recognition," *IEEE IEEE Symposium Series on Computational Intelligence in Biometrics: Theory, Algorithms, and Applications*, 2009.

[2] J. R. Matley, D. Ackerman, J. Bergen, and M. Tinker, "Iris recognition in less constrained environments," *Springer Advances in Biometrics: Sensors, Algorithms and Systems*, pp. 107–131, October 2007.

[3] "A distance iris recognition," Honeywell International Inc., Tech. Rep., 2007, united States Patent 20070036397.

[4] C. Fancourt, L. Bogoni, K. Hanna, Y. Guo, R. Wildes, N. Takahashi, and U. Jain, "Iris recognition at a distance," in *Proceedings of the 2005 IAPR Conference on Audio and Video Based Biometric Person Authentication*, U.S.A., July 2005, pp. 1–13.

[5] R. Narayanswamy, G. Johnson, P. Silveira, and H. Watch, "Extending the imaging volume for biometric iris recognition," *Applied Optics*, vol. 44, no. 5, pp. 701–712, February 2005.

[6] K. Park and J. Kim, "A real-time focusing algorithm for iris recognition camera," *IEEE Transactions on Systems, Man and Cybernetics*, vol. 35, no. 3, pp. 441–444, August 2005.

[7] Y. He, J. Cui, T. Tan, and Y. Wang, "Key techniques and methods for imaging iris in focus," in *Proceedings of the IEEE International Conference on Pattern Recognition*, August 2006, pp. 557–561.

[8] J. G. Daugman, "How iris recognition works," *IEEE Transactions on Circuits and Systems for Video Technology*, vol. 14, no. 1, pp. 21–30, January 2004.

[9] L. Ma, T. Tan, Y. Wang, and D. Zhang, "Personal identification based on iris texture analysis," *IEEE Transactions on Pattern Analysis and Machine Intelligence*, vol. 25, no. 12, pp. 2519–2533, December 2003.

[10] C. Tisse, L. Martin, L. Torres, and M. Robert, "Person identification technique using human iris recognition," in *Proceedings of the 25th International Conference on Vision Interface*, Calgary, July 2002, pp. 294–299.

[11] H. Proença and L. Alexandre, "Ubiris: A noisy iris image database." in *Proceedings of ICIAP 2005 - Interacional Conference on Image Analysis and Processing, Vol. 1*, 2005, pp. 970–977.

[12] H. Proença, S. Filipe, R. Santos, J. Oliveira, and L. A. Alexandre, "The ubiris.v2: A database of visible wavelength iris images captured on-the-move and at-a-distance," *IEEE Transactions on Pattern Analysis and Machine Intelligence*.

[13] J. G. Daugman, "Phenotypic versus genotypic approaches to face recognition," in *Face Recognition: From Theory to Applications*. Heidelberg: Springer-Verlag, 1998, pp. 108–123.

[14] W. W. Boles and B. Boashash, "A human identification technique using images on the iris and wavelet transform," *IEEE Transactions on Signal Processing*, vol. 46, no. 4, pp. 1185–1188, April 1998.

[15] R. P. Wildes, "Iris recognition: an emerging biometric technology, vol. 85, no. 9," in *Proceedings of the IEEE*, U.S.A., September 1997, pp. 1348–1363.

[16] Y. Huang, S. Luo, and E. Chen, "An efficient iris recognition system," in *Proceedings of the First International Conference on Machine Learning and Cybernetics*, China, November 2002, pp. 450–454.

[17] L. Ma, T. Tan, Y. Wang, and D. Zhang, "Local intensity variations analysis for iris recognition," *Pattern recognition, vol. 37, no. 6*, pp. 1287–1298, 2004.

[18] J. G. Daugman, "New methods in iris recognition," *IEEE Transactions on Systems, Man, and Cybernetics - Part B: Cybernetics*, vol. 37, no. 5, pp. 1167–1175, 2007.

[19] J. L. Cambier, "Iridian large database performance," Iridian Technologies, Tech. Rep., 2007, http://iridiantech.com.

[20] "Independent test of iris recognition technology," International Biometric Group, Tech. Rep., 2005, http://www.biometricgroup.com.

[21] T. Mansfiel, G. Kelly, D. Chandler, and J.Kane, "Biometric product testing and final report, issue 1.0," 2001.

[22] J. G. Daugman, "High confidence visual recognition of persons by a test of statistical independence," *IEEE Transactions on Pattern Analysis and Machine Intelligence*, vol. 25, no. 11, pp. 1148–1161, November 1993.

[23] W. H. Press, S. A. Teukolsky, W. T. Vetterling, and B. P. Flannery, *Numerical Recipes 3rd Edition: The Art of Scientific Computing*. U.K.: Cambridge University Press, 2007.

Bibliography

[1] BioRec - Non-Cooperative Multimodal Biometric Recognition. `http://www.di.ubi.pt/~lfbaa/biorec.html`.

[2] CIS'09 - 2009 International Conference on Computational Intelligence and Security. `http://cis2009.bit.edu.cn`.

[3] Alan Agresti. *Categorical Data Analysis (Wiley Series in Probability and Statistics).* Wiley Interscience, Hoboken, NJ, July 2002.

[4] Gladimir V. G. Baranoski and Michael W. Y. Lam. Qualitative assessment of undetectable melanin distribution in lightly pigmented irides. *Journal of Biomedical Optics*, 12(3):030501, 2007.

[5] C. Belcher and Yingzi Du. Feature information based quality measure for iris recognition. In *Systems, Man and Cybernetics, 2007. ISIC. IEEE International Conference on*, pages 3339–3345, Oct. 2007.

[6] Peter N. Belhumeur, João P. Hespanha, and David J. Kriegman. Eigenfaces vs. fisherfaces: recognition using class specific linear projection. *Pattern Analysis and Machine Intelligence, IEEE Transactions on*, 19(7):711–720, July 1997.

[7] N. Boddeti and B. Kumar. Extended depth of field iris recognition with correlation filters. In *Biometrics: Theory, Applications and Systems, 2008. BTAS 2008. 2nd IEEE International Conference on*, pages 1–8, October 2008.

[8] Randy P. Boussard, Lauren R. Kennell, David L. Soldan, and Robert W. Ives. Using artificial neural networks and feature saliency techniques for improved iris segmentation. In *Neural Networks, 2007. IJCNN 2007. International Joint Conference on*, pages 1283–1288, Orlando, Florida, August 2007.

[9] Christopher Boyce, Arun Ross, Matthew Monaco, Lawrence Hornak, and Xin Li. Multispectral iris analysis: A preliminary study. 2008.

[10] Alan B. M Cantor. Understanding logistic regression. *Evidence-based Oncology*, 3(2):52 – 53, 2002.

[11] Lih-Heng Chan, Sh-Hussain Salleh, and Chee-Ming Ting. PCA, LDA and neural network for face identification. In *Industrial Electronics and Applications, 2009. ICIEA 2009. 4th IEEE Conference on*, pages 1256–1259, May 2009.

[12] Yi Chen, Sarat C. Dass, and Anil K. Jain. Localized iris image quality using 2-d wavelets. In *ICB*, pages 373–381, 2006.

[13] Peter Clark and Tim Niblett. The CN2 induction algorithm. *Machine Learning*, 3(4):261–283, March 1989.

[14] J. Daugman. High confidence recognition of persons by iris patterns. In *Security Technology, 2001 IEEE 35th International Carnahan Conference on*, pages 254–263, October 2001.

[15] J. Daugman. Probing the uniqueness and randomness of iriscodes: Results from 200 billion iris pair comparisons. *Proceedings of the IEEE*, 94(11):1927–1935, Nov. 2006.

[16] J. Daugman and C. Downing. Effect of severe image compression on iris recognition performance. *Information Forensics and Security, IEEE Transactions on*, 3(1):52–61, March 2008.

[17] John G. Daugman. High confidence visual recognition of persons by a test of statistical independence. *Pattern Analysis and Machine Intelligence, IEEE Transactions on*, 15(11):1148–1161, November 1993.

[18] John G. Daugman. How iris recognition works. *Circuits and Systems for Video Technology, IEEE Transactions on*, 14(1):21–30, January 2004.

[19] John G. Daugman. New methods in iris recognition. *Systems, Man, and Cybernetics, Part B: Cybernetics, IEEE Transactions on*, 37(5):1167–1175, October 2007.

[20] Chris Ding and Hanchuan Peng. Minimum redundancy feature selection from microarray gene expression data. In *Bioinformatics Conference, 2003. CSB 2003. Proceedings of the 2003 IEEE*, pages 523–528, August 2003.

[21] Chris Ding and Hanchuan Peng. Minimum redundancy feature selection from microarray gene expression data. *Journal of Bioinformatics and Computational Biology*, 3(2):185–205, June 2005.

[22] Richard O. Duda, Peter E. Hart, and David G. Stork. *Pattern Classification (2nd Edition)*. Wiley-Interscience, November 2000.

[23] Mark D. Fairchild. *Color Appearance Models*. Jonh Wiley & Sons, Inc., 2nd edition, 2005.

[24] Craig Fancourt, Luca Bogoni, Keith Hanna, Yanlin Guo, Richard Wildes, Naomi Takahashi, and Uday Jain. Iris recognition at a distance. In *Proceedings of the 2005 IAPR Conference on Audio and Video Based Biometric Person Authentication*, pages 1–13, U.S.A., July 2005.

[25] Xiaofei He and Partha Niyogi. Locality preserving projections. In *In Advances in Neural Information Processing Systems 16*. MIT Press, 2003.

[26] Yuqing He, Jiali Cui, Tieniu Tan, and Yangsheng Wang. Key techniques and methods for imaging iris in focus. In *Proceedings of the IEEE International Conference on Pattern Recognition*, pages 557–561, August 2006.

[27] David W. Hosmer and Stanley Lemeshow. *Applied logistic regression (Wiley Series in probability and statistics)*. Wiley-Interscience Publication, September 2000.

[28] Lee Hsien-Che. *Introduction to Color Imaging Science*. Cambridge University Press, New York, USA, 2005.

[29] Junzhou Huang, Yunhong Wang, Jiali Cui, and Tieniu Tan. Noise removal and impainting model for iris image. In *Image Processing, 2004. ICIP '04. 2004 International Conference on*, volume 2, pages 869–872, October 2004.

[30] Honeywell International Inc. A distance iris recognition, 2007. United States Patent 20070036397.

[31] R.W. Ives, B.L. Bonney, and D.M. Etter. Effect of image compression on iris recognition. In *Instrumentation and Measurement Technology Conference, 2005. IMTC 2005. Proceedings of the IEEE*, volume 3, pages 2054–2058, May 2005.

[32] Byung Jun Kang and Kang Ryoung Park. Real-time image restoration for iris recognition systems. *Systems, Man, and Cybernetics, Part B: Cybernetics, IEEE Transactions on*, 37(6):1555–1566, December 2007.

[33] Vojislav Kecman. *Learning and Soft Computing*. MIT Press, Cambridge, 2001.

[34] A. Kong, D. Zhang, and M. Kamel. An anatomy of iriscode for precise phase representation. In *Pattern Recognition, 2006. ICPR 2006. 18th International Conference on*, volume 4, pages 429–432, 2006.

[35] Mats Larsson and Nancy L. Pedersen. Genetic correlations among texture characteristics in the human iris. *Molecular Vision*, pages 821–831, November 2004.

[36] Chengjun Liu and H. Wechsler. Gabor feature based classification using the enhanced fisher linear discriminant model for face recognition. *Image Processing, IEEE Transactions on*, 11(4):467–476, April 2002.

[37] Li Ma, Tieniu Tan, Yunhong Wang, and Dexin Zhang. Personal identification based on iris texture analysis. *Pattern Analysis and Machine Intelligence, IEEE Transactions on*, 25(12):1519–1533, December 2003.

[38] Elaine N. Marieb. *Human Anatomy & Physiology*, chapter 15. Benjamin-Cummings Publishing Company, 7th edition, 2007.

[39] Aleix M. Martinez and Avinash C. Kak. PCA versus LDA. *Pattern Analysis and Machine Intelligence, IEEE Transactions on*, 23(2):228–233, February 2001.

[40] James R. Matey, Oleg Naroditsky, Keith Hanna, Ray Kolczynski, Dominick J. LoIacono, Shakuntala Mangru, Michael Tinker, Thomas M. Zappia, and Wenyi Y. Zhao. Iris on the move: Acquisition of images for iris recognition in less constrained environments. *Proceedings of the IEEE*, 94(11):1936–1947, November 2006.

[41] Tom M. Mitchell. *Machine Learning*. McGraw-Hill Science/Engineering/Math, March 1997.

[42] Kazuyuki Miyazawa, Koichi Ito, Takafumi Aoki, Koji Kobayashi, and Hiroshi Nakajima. An effective approach for iris recognition using phase-based image matching. *Pattern Analysis and Machine Intelligence, IEEE Transactions on*, 30(10):1741–1756, October 2008.

[43] Donald M. Monro, Soumyadip Rakshit, and Dexin Zhang. DCT-based iris recognition. *Pattern Analysis and Machine Intelligence, IEEE Transactions on*, 29(4):586–595, April 2007.

[44] R. Narayanswamy, G. Johnson, P. Silveira, and H. Wach. Extending the imaging volume for biometric iris recognition. *Applied Optics, vol. 44, no. 5*, pages 701–712, February 2005.

[45] Jong Hyun Park and Moon Gi Kang. Noise reduction for gradient-based multispectral image fusion. In *Intelligent Signal Processing and Communication Systems, 2004. ISPACS 2004. Proceedings of 2004 International Symposium on*, pages 185–188, November 2004.

[46] Kang Park and Jaihie Kim. A real-time focusing algorithm for iris recognition camera. *IEEE Transactions on Systems, Man and Cybernetics, vol. 35, no. 3*, pages 441–444, August 2005.

[47] Hanchuan Peng, Fuhui Long, and Chris Ding. Feature selection based on mutual information: Criteria of max-dependency, max-relevance, and min-redundancy. *IEEE Transactions on Pattern Analysis and Machine Intelligence*, 27(8):1226–1238, August 2005.

[48] B. Pierscionek, S. Crawford, and B. Scotney. Iris recognition and ocular biometrics - the salient features. In *Machine Vision and Image Processing Conference, 2008. IMVIP '08. International*, pages 170–175, September 2008.

[49] W. H. Press, S. A. Teukolsky, W. T. Vetterling, and B. P. Flannery. *Numerical Recipes 3rd Edition: The Art of Scientific Computing.* Cambridge University Press, U.K., 2007.

[50] Hugo Proença. *Towards Non-Cooperative Biometric Iris Recognition.* PhD thesis, University of Beira Interior, October 2006.

[51] Hugo Proença. A structural pattern analysis approach to iris recognition. *Computer Recognition Systems 2*, 45:731–738, 2008.

[52] Hugo Proença and Luís A. Alexandre. A method for the identification of noisy regions in normalized iris images. In *ICPR '06: Proceedings of the 18th International Conference on Pattern Recognition*, pages 405–408, Washington, DC, USA, 2006. IEEE Computer Society.

[53] Hugo Proença and Luís A. Alexandre. The NICE.I: Noisy iris challenge evaluation - part i. In *Biometrics: Theory, Applications, and Systems, 2007. BTAS 2007. First IEEE International Conference on*, pages 1–4, September 2007.

[54] Hugo Proença, Sílvio Filipe, Ricardo Santos, João Oliveira, and Luís A. Alexandre. The UBIRIS.v2: A database of visible wavelength images captured on-the-move and at-a-distance. *IEEE Transactions on Pattern Analysis and Machine Intelligence*, 99(1), 5555.

[55] Hugo Proença and Luís A. Alexandre. UBIRIS: A noisy iris image database. In *ICIAP*, pages 970–977, September 2005.

[56] S. Rakshit and D.M. Monro. Effects of sampling and compression on human iris verification. In *Acoustics, Speech and Signal Processing, 2006. ICASSP 2006 Proceedings. 2006 IEEE International Conference on*, volume 2, pages II–II, May 2006.

[57] Gil Santos and Hugo Proença. On the role of the interpolation method in the normalization of non-ideal visible wavelength iris images.

[58] S.A.C. Schuckers, N.A. Schmid, A. Abhyankar, V. Dorairaj, C.K. Boyce, and L.A. Hornak. On techniques for angle compensation in nonideal iris recognition. *Systems, Man, and Cybernetics, Part B: Cybernetics, IEEE Transactions on*, 37(5):1176–1190, October 2007.

[59] K.N. Smith, V.P. Pauca, A. Ross, T. Torgersen, and M.C. King. Extended evaluation of simulated wavefront coding technology in iris recognition. In *Biometrics: Theory, Applications, and Systems, 2007. BTAS 2007. First IEEE International Conference on*, pages 1–7, September 2007.

[60] Masashi Sugiyama. Local fisher discriminant analysis for supervised dimensionality reduction. In *ICML '06: Proceedings of the 23rd international conference on Machine learning*, pages 905–912, New York, NY, USA, 2006. ACM Press.

[61] Christel-Loc Tisse, Lionel Martin, Lionel Torres, and Michel Robert. Person identification technique using human iris recognition. In *Proc. of Vision Interface*, pages 294–299, July 2002.

[62] M. Vatsa, R. Singh, and A. Noore. Improving iris recognition performance using segmentation, quality enhancement, match score fusion, and indexing. *Systems, Man, and Cybernetics, Part B: Cybernetics, IEEE Transactions on*, 38(4):1021–1035, August 2008.

[63] Meritxell Vilaseca, Rita Mercadal, Jaume Pujol, Monserrat Arjona, Marta de Lasarte, Rafael Huertas, Manuel Melgosa, and Francisco H. Imai. Characterization of the human iris spectral reflectance with a multispectral imaging system. *Appl. Opt.*, 47(30):5622–5630, 2008.

[64] Andrew R. Webb. *Statistical Pattern Recognition, 2nd Edition.* John Wiley & Sons, October 2002.

[65] Max Welling. Fisher linear discriminant analysis.

[66] Richard P. Wildes. Iris recognition: an emerging biometric technology. *Proceedings of the IEEE*, 85(9):1348–1363, September 1997.

[67] Guangzhu Xu, Zaifeng Zhang, and Yide Ma. Improving the performance of iris recogniton system using eyelids and eyelashes detection and iris image enhancement. In *Cognitive Informatics, 2006. ICCI 2006. 5th IEEE International Conference on*, volume 2, pages 871–876, July 2006.

[68] Peng Yao, Jun Li, Xueyi Ye, Zhenquan Zhuang, and Bin Li. Analysis and improvement of an iris identification algorithm. In *Pattern Recognition, 2006. ICPR 2006. 18th International Conference on*, volume 4, pages 362–365, 2006.

[69] Peng Yao, Jun Li, Xueyi Ye, Zhenquan Zhuang, and Bin Li. Iris recognition algorithm using modified log-gabor filters. In *Pattern Recognition, 2006. ICPR 2006. 18th International Conference on*, volume 4, pages 461–464, 2006.

[70] Li Yu, David Zhang, and Kuanquan Wang. The relative distance of key point based iris recognition. *Pattern Recognition*, 40(2):423–430, 2007.

[71] Harry Zhang. The optimality of naive bayes. In Valerie Barr, Zdravko Markov, Valerie Barr, and Zdravko Markov, editors, *FLAIRS Conference*. AAAI Press, 2004.

[72] Yong Zhu, Tieniu Tan, and Yunhong Wang. Biometric personal identification based on iris patterns. In *Pattern Recognition, 2000. Proceedings. 15th International Conference on*, volume 2, pages 801–804, 2000.